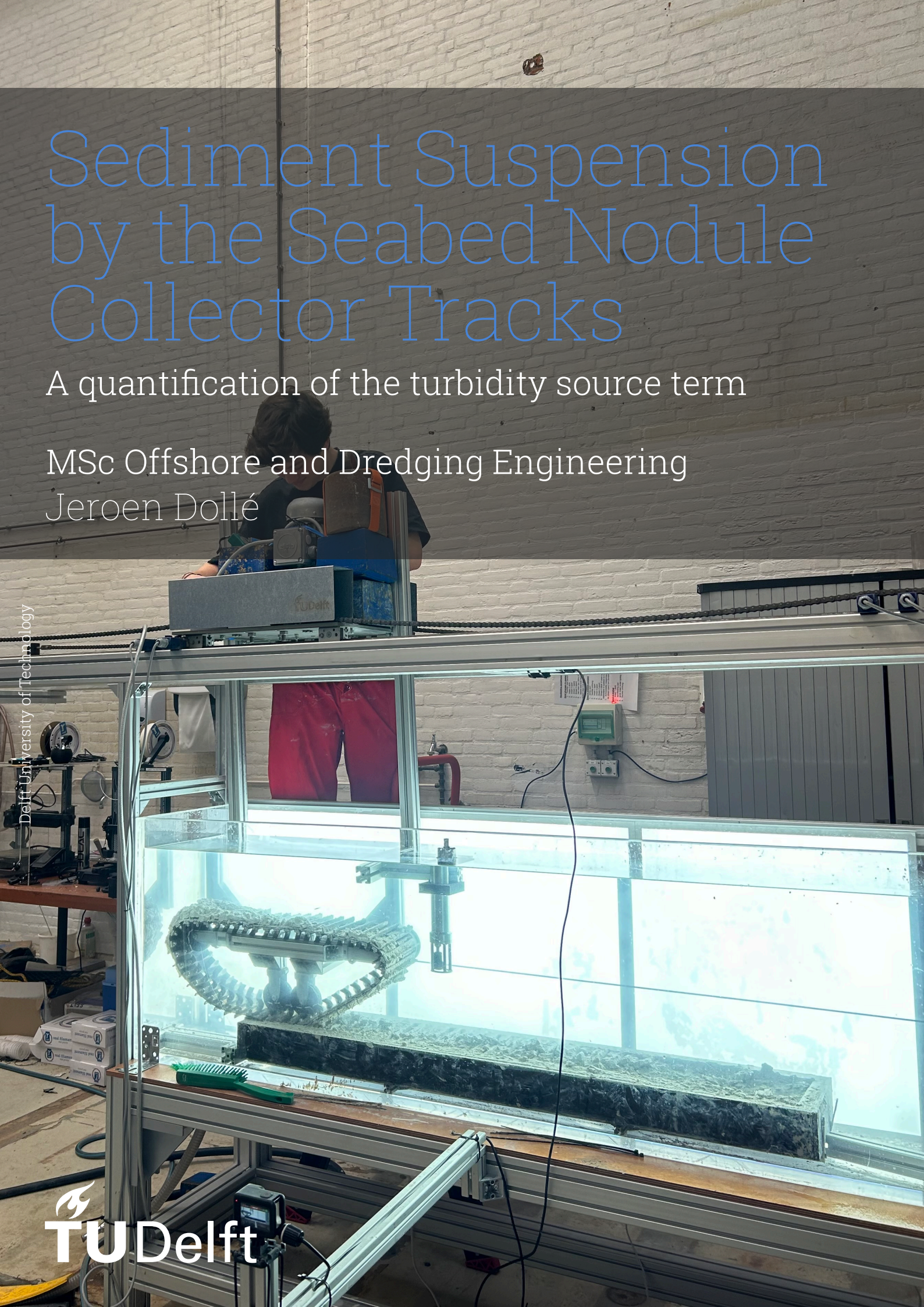
Sediment Suspension by the Seabed Nodule Collector Tracks

A quantification of the turbidity source term

MSc Offshore and Dredging Engineering

Jeroen Dollé



Delft University of Technology

TU Delft

Sediment Suspension by the Seabed Nodule Collector Tracks

A quantification of the turbidity source term

by

Jeroen Dollé

to obtain the degree of Master of Science
at the Delft University of Technology,
to be defended on 16 May 2025

Student number:	4915038	
Thesis committee:	Dr.ir. R.L.J. Helmons	TU Delft, chairman
	Dr.ir. G.H. Keetels	TU Delft
	Dr.ir. S. Akrami	Allseas
	ing. A. Vermeulen	Allseas
Faculty:	Faculty of Mechanical Engineering	TU Delft

Cover: Image of the experimental setup where the height of the tracks is adjusted

TU Delft

Abstract

With the rising global demand for rare earth metals, innovative approaches such as deep-sea polymetallic nodule collection have gained increasing attention. The Clarion-Clipperton Zone (CCZ), one of the most economically promising regions for these resources, is a key focus area. However, before large-scale exploitation can be carried out, it is essential to understand and minimise the environmental impacts thoroughly. One of the primary concerns regarding the environmental impact is the generation of sediment plumes.

This study has aimed to improve the understanding of sediment plumes generated by the tracks of the Seabed Nodule Collector in the NORI-D area. NORI-D is an area within the CCZ. A literature review has been conducted to examine the characteristics of the NORI-D site and the collector's track design, identifying key mechanisms of plume generation. Building on these insights, a kinematic model has been developed to estimate sediment relocation. A previous study on plume generation during a nodule collector test run in the GSR area has provided a valuable starting point. To pursue the remaining research objectives, a series of laboratory experiments has been performed, focusing on the effects of seabed penetration depth, driving velocity, slip ratio, and sediment type. A scaled model of the collector tracks has been driven over a sediment bed, using an artificial clay developed to mimic the behaviour of deep-sea sediment.

The combined insights from the literature review, kinematic model and experimental work now offer a sound understanding of sediment plume formation and an estimation of the turbidity source term associated with the collector tracks. The results provide an insight into the influence of the tested parameters on plume generation, identifying seabed penetration and driving velocity as the key factors. The knowledge gained from this research could support efforts to minimise the environmental impact of deep-sea mining operations on the seabed.

Preface

During my master's studies, I took the course Subsea Engineering, where I was introduced to deep-sea mining and the many challenges it entails. I was intrigued by the innovative techniques that enable the collection of materials such as polymetallic nodules from extreme depths. This sparked my interest in focusing my graduation project on deep-sea mining. However, while I am fascinated by the technology involved, I am also concerned about the potential consequences of these activities for the seabed and, consequently, the global environment. For this reason, I wanted to seize this opportunity to contribute to reducing its environmental impact, while still exploring this fascinating field.
With this project, I have aimed to take the first steps towards understanding the track-induced sediment plume and I hope that future researchers will build on this work to assess its impact more completely and ultimately help minimise its environmental footprint.
Given the complexity of deep-sea mining, this project presented several challenges and required making difficult decisions along the way. I would like to thank Rudy Helmons for the many discussions, for guiding me through the entire process and for helping me avoid making things unnecessarily difficult for myself. I am also grateful to Sepideh Akrami from Allseas for the many valuable discussions on complex soil mechanics, her advice on improving my writing and sharing her research experience, which helped me a lot. My thanks also go to Alexander Vermeulen from Allseas for his guidance on the complex technical aspects of the experimental setup and his support throughout the project. Finally, I would like to thank Ed Stok, Andre van den Bosch and Huib Zuurmond for their help in constructing the test setup in the laboratory.

Jeroen Dollé
Delft, May 2025

Contents

Abstract i

Preface ii

Nomenclature v

1 Introduction 1
- 1.1 Background . . . 1
- 1.2 Research Objectives . . . 3
- 1.3 Outline of Research . . . 3

2 Deep-sea Sediment and The Environment 4
- 2.1 Environment . . . 4
- 2.2 Sediment Composition and Characteristics . . . 7

3 Seabed Nodule Collector Tracks 12
- 3.1 Track Design . . . 12
- 3.2 Behaviour in Deep-Sea Sediment . . . 13
- 3.3 Kinematic Clay Disturbance Model . . . 16
  - 3.3.1 Seabed Penetration . . . 17
  - 3.3.2 Grousers . . . 17
  - 3.3.3 Jets and Adhesion . . . 19
- 3.4 Collector Field Test . . . 19

4 Experiments 21
- 4.1 Experimental Setup & Materials . . . 21
  - 4.1.1 Tracks . . . 22
  - 4.1.2 Sediment . . . 23
  - 4.1.3 Optical Backscatter Point Sensor . . . 27
  - 4.1.4 3D Camera . . . 29
- 4.2 Methodology . . . 31
- 4.3 Test Matrix and Parameters . . . 34
- 4.4 Results . . . 35
  - 4.4.1 Data Processing . . . 36
  - 4.4.2 Seabed Penetration . . . 37
  - 4.4.3 Driving Velocity . . . 38
  - 4.4.4 Slip Ratio . . . 40
  - 4.4.5 Sediment Type . . . 42
  - 4.4.6 Sediment Pick-Up at Start Location . . . 44

5 Discussion 45
- 5.1 Experimental Limitations . . . 45
  - 5.1.1 Setup Limitations . . . 45
  - 5.1.2 OBS Calibration . . . 47
  - 5.1.3 Sediment Bed Height Profiles . . . 48
  - 5.1.4 Millisil . . . 49
- 5.2 Results Discussion . . . 49
  - 5.2.1 Seabed Penetration . . . 49
  - 5.2.2 Driving Velocity . . . 50
  - 5.2.3 Slip Ratio . . . 51
  - 5.2.4 Sediment Type . . . 53
  - 5.2.5 Recovery Time . . . 54

5.3 Comparison of Experimental Results with Other Models 55

6 Conclusion & Recommendations **58**
6.1 Conclusion 58
6.2 Recommendations 59
6.2.1 Experiments 59
6.2.2 Setup Design 59
6.2.3 Future Research 60

References **61**

A Kinematic Sediment Relocation Model **64**
A.1 Seabed Penetration 64
A.2 Scooping 65
A.3 Pull-out 68

B Raw OBS Data **71**

C Sediment Bed Pictures **81**

D Sediment Bed Height Profiles **83**

E Millisil Results **95**

F Millisil Filtering Process **97**

Nomenclature

Abbreviations

Abbreviation	Definition
AC	Artificial Clay
CCZ	Clarion Clipperton Zone
CPT	Cone Penetration Test
DSC	Deep-sea Clay
DSM	Deep-sea Mining
GSR	Global Sea Mineral Resources NV
IOM	InterOceanMetal
NORI-D	Nauru Ocean Resources Inc area D
OBS	Optical Backscatter Point Sensor
PMT	Pilot Mining Test
PNMT	Polymetallic Nodule Mining Tool
ROV	Remotely Operated Vehicle
SNC	Seabed Nodule Collector
TMC	The Metals Company

Symbols

Symbol	Definition	Unit
A	Contact area	$[m^2]$
$A_{grouser,po}$	Area disturbed wet sediment by pull-out for a single grouser	$[m^2]$
B	Track width	$[m]$
c	Cohesion	$[kPa]$
C	concentration	$[g/L]$
$F_{available}$	Traction after disturbance	$]kN]$
F_{max}	Traction before disturbance	$[kN]$
g	Gravitational constant	$[m/s^2]$
k_c	Cohesive modulus	$[kN/m^{2.6}]$
k_ϕ	Frictional modulus	$[kN/m^{3.6}]$
$m_{grouser,po,mix}$	Mass disturbed wet sediment by pull-out for a single grouser	$[kg]$
$m_{pullout}$	Mass disturbed dry sediment by pull-out	$[kg]$
$m_{pullout,mix}$	Mass disturbed wet sediment by pull-out	$[kg]$
M_r	Motion resistance	$[kN]$
m_s	Sediment mass	$[kg]$
$m_{penetration}$	Mass disturbed dry sediment by seabed penetration	$[kg]$
$m_{penetration,mix}$	Mass disturbed wet sediment by seabed penetration	$[kg]$
m_{tot}	Total mass of the removed soil by the seabed penetration	$[kg]$
n	Terrain deformation exponent	[-]
n_t	Number of grousers per meter	[-]
N_c	Bearing capacity factor (5.14)	[-]
p	Pressure	$[kPa]$

Symbol	Definition	Unit
s	Distance traveled by the tracks	[m]
s_{bw}	Grouser distance traveled backward	[m]
s_{fw}	Grouser distance traveled forward	[m]
$s_{traveled}$	Track distance traveled	[m]
s_u	Undrained shear strength	[kPa]
s_{up}	Grouser distance traveled up	[m]
T	Turbidity	[FTU]
u	Mass water content	[%]
V	Submerged track volume	[m^3]
$V_{grouser,po,mix}$	Volume disturbed wet sediment by pull-out for a single grouser	[m^3]
$V_{penetration,mix}$	Volume disturbed wet sediment by seabed penetration	[m^3]
W	Normal load	[kN]
W_g	Grouser width	[m]
z	Seabed penetration	[m]
z_g	Grouser depth	[m]
α	Disturbance factor	[-]
β	Angle track wheel	[]
γ_s	Soil unit weight	[kN/m^3]
γ_w	Water unit weight (10.05 kN/m^3)	[kN/m^3]
ϵ	Pull-out angle	[]
ϕ	Angle of internal friction	[]
ρ_{mix}	Bulk density wet sediment	[kg/m^3]

1

Introduction

1.1. Background

The demand for critical raw materials is increasing rapidly, with the global energy transition being one of the primary drivers. Technologies such as solar panels and batteries require substantial amounts of these materials, creating a growing need for innovative solutions to meet this demand. Deep-sea mining (DSM) has emerged as a promising option. Vast mineral deposits have been discovered on the ocean floor worldwide, as illustrated in Figure 1.1. One of the most prominent and widely discussed areas is the Clarion-Clipperton Zone (CCZ). This region contains large deposits of polymetallic nodules and is considered one of the most economically viable areas due to the high abundance of nodules [1]. The CCZ is also the most extensively studied and holds the majority of exploration licenses. It is located in the Pacific Ocean and indicated by the green arrow in Figure 1.1.

Polymetallic nodules are potato-shaped and typically range in diameter from 1 to 20 cm [2]. They are found on the top layer of the seabed, often partially embedded in the seafloor and occasionally completely buried. What makes these nodules particularly valuable is their high concentration of manganese, nickel, copper, cobalt, and other essential minerals [1–3].

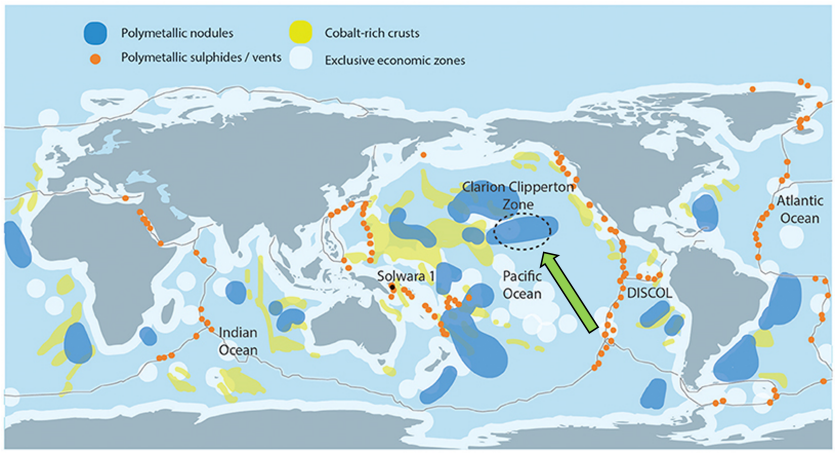


Figure 1.1: All discovered ore deposits in the ocean distinguished by type and the location of the Clarion Clipperton Zone [4] (edited)

The depth of the Clarion-Clipperton Zone (CCZ) ranges from 4 to 6 kilometers [5], making it a highly challenging environment for nodule collection. To overcome this, several parties are developing technologies to retrieve these nodules from the seafloor. One such company is Allseas Engineering B.V., which is developing a tracked vehicle that uses the Coandă effect to collect nodules from the seabed. This Polymetallic Nodule Mining Tool (PNMT) is known as the Seabed Nodule Collector (SNC).

While deep-sea mining (DSM) offers a promising alternative for securing the supply of critical raw materials, it also raises significant environmental concerns. In an environment dominated by very soft sediment, polymetallic nodules, being the only hard substrates available, serve as essential habitats for small benthic organisms living on the seafloor [6–8]. Extracting these nodules effectively removes their habitat. Environmental impacts at the mining site have been shown to persist for several decades [9]. Another major concern is the sediment plume generated during DSM operations. This plume can spread beyond the mined area [10], covering life on the surrounding seabed by forming a dense layer (blanketing) and generating a cloud of suspended sediment. As it disperses, the impact extends beyond the immediate mining site, affecting the surrounding environment as well.
Before commercial exploitation begins, it is crucial to understand these impacts and explore ways to minimise them. For this reason, gaining a better understanding of the sources of environmental disturbances is essential. This study focuses specifically on sediment plumes.
Previous research has identified four primary mechanisms through which sediment plumes are generated: the returned water plume, diffuser plume, track plume, and spillage plume (Figure 1.2). Although sediment plumes have been studied to some extent, the track plume has received relatively little attention. This study aims to shed more light on the track plume by investigating its formation and behavior in greater detail.

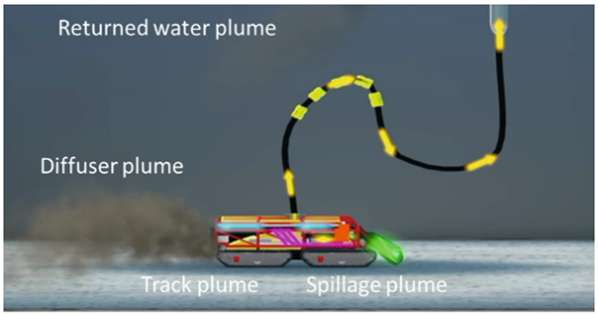


Figure 1.2: Different origins of a sedimentation plume created by a Coandã-based nodule collector device[11]

Several organisations have already conducted deep-sea tests using tracked Coandă-based nodule collectors, providing a valuable foundation for this study. Global Sea Mineral Resources NV (GSR) and The Metals Company (TMC) conducted test campaigns using their respective nodule collectors in their designated areas within the Clarion-Clipperton Zone (CCZ). Both parties published Environmental Impact Statements (EIS) that include findings on the local environmental characteristics and provide estimates of the potential impacts of their activities. These reports offer useful data to build upon.
In addition, Muñoz-Royo et al. [12] analysed plume generation during GSR's CCZ test using the "selfie manoeuvre". In this manoeuvre, the PNMT first drives in a straight line and then performs three consecutive left turns to circle back and intersect the plume it previously generated. One of the tests was conducted with the collection system turned off, allowing the analysis to focus solely on the plume generated by the movement of the tracks. This resulted in a plume generation of 3 ± 2 kg/s, which is four times smaller than when the full collecting system was in operation. The findings from this study serve as a starting point for the current research.

1.2. Research Objectives

Building on previous research, this study aims to scope the track plume and get an understanding of its behaviour and physics. That will be done by answering the following question:

What is the turbidity source term for the suspended sediment originating from the tracks of the Seabed Nodule Collector?

To help answer this question and acquire the needed knowledge, the following sub-questions are formulated:

- What physical phenomena cause sediment suspension that originates from the tracks?
- Which sediment and near-bottom environmental characteristics are relevant for the sediment suspension by the SNC tracks?
- What are the most influential design choices that impact plume generation and how is plume generation affected if these design choices are changed? Do plume-reducing adjustments have a penalty on other aspects of the track function?
- Can a model based on kinematics approximate the sediment suspension by the tracks

1.3. Outline of Research

To address these questions, it is essential to develop a thorough understanding of the target location and its environmental conditions. Chapter 2 examines the near-bottom environment, sediment composition and geotechnical properties of the area where the Seabed Nodule Collector (SNC) is anticipated to operate.
Chapter 3 then investigates the mechanisms of sediment suspension by examining the track design and its interaction with the seabed. Based on these insights, a kinematic model is developed to estimate the amount of sediment relocated by the tracks.
To validate and refine this model, a series of experiments are conducted, as described in Chapter 4. This chapter outlines the experimental setup, explains the design choices and aims to explore the outstanding questions while offering deeper insights into track–soil interaction. The chapter concludes with a presentation of the results and the relationships identified from the data.
These relationships are further analysed in Chapter 5, where they are supported by existing literature and fundamental physical principles. The implications for both the kinematic model and real-world deep-sea conditions are then discussed.
Finally, Chapter 6 provides a comprehensive conclusion, addressing all research questions based on the findings and discussions. It also presents a list of recommendations for improving the experiments and interesting future research.

2

Deep-sea Sediment and The Environment

As mentioned earlier, the depth of the CCZ ranges from 4 km to 6 km [5]. The CCZ encompasses a vast area and is divided into distinct zones. The division of all licensed and protected areas is shown in Figure 2.1. The area where the SNC is expected to be used is NORI-D [13]. This area is one of the exploration areas of Nauru Ocean Resources Inc. (NORI) in the southeast of the CCZ.

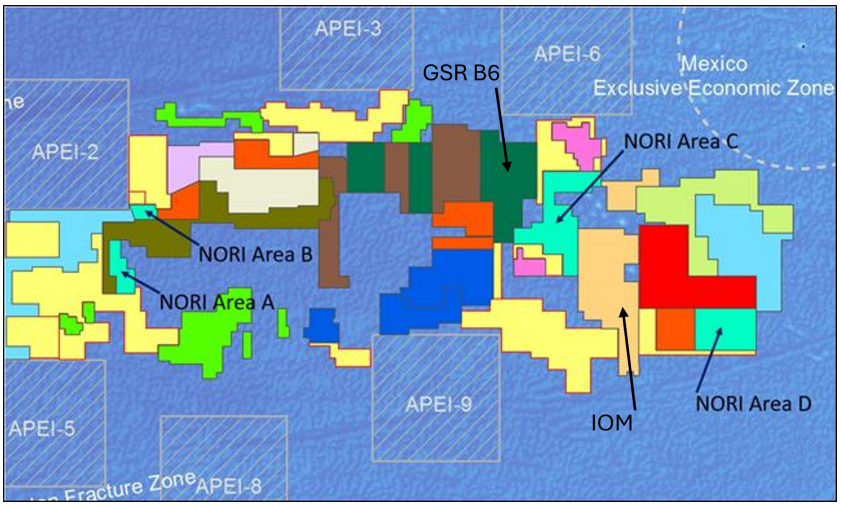


Figure 2.1: All licensed and protected zones in the CCZ with the NORI-D zone in the South-East corner and the other investigated areas [14]

This chapter will discuss the environment and soil properties of the NORI-D area at the seabed. The properties of the sediment and environment can be different at a large depth compared to a laboratory setting. It is crucial to keep this in mind when designing the SNC and conducting tests. To check the reliability of these findings, they will be compared to conditions found at other locations in the CCZ.

2.1. Environment

The subsea environment can affect the behavior of the soil and the likelihood of a sediment plume forming. The water properties vary with depth. The NORI-D area has a depth ranging from 4,270 m to 4,300 m [15]. NORI published an Environmental Impact Statement [2] detailing their findings about the NORI-D area, including water properties. It deployed three moorings at varying depths and collected data over a period of 7.5 months, from 14 October 2019 to 16 June 2020. The most relevant

mooring for this research is the ”Long Mooring,” which conducted measurements near the seabed. This mooring recorded an average current speed ranging from 2.16 to 3.16 cm/s, with a maximum speed of approximately 9 cm/s. The current at this location predominantly flows in a northwest direction, but this should be interpreted cautiously, as the data is from a single mooring at that certain depth. The other two moorings, located at different depths and positions, show different current directions. The significance of the current lies in its potential to act as an amplifying factor in combination with the collector's activities, influencing the sediment suspension rate. The water flow driven by the current can mobilise additional sediment from the seabed as the tracks loosen it.
NORI [2] also measured temperature, salinity, and dissolved oxygen levels. In addition to the mooring data, measurements were taken from five stations in the area. Data from these stations, collected in October 2019, are shown in Figure 2.2. The temperature decreases with depth and stabilises below 2,000 m, ranging from approximately 1.5 °C to 2 °C. This is consistent with data from the mooring, which recorded a steady 1.5°C over the months. The temperature of the water is relevant for the liquid viscosity, as that influences the settling velocity and transport of particles. The salinity measurements from the stations, displayed in Figure 2.2b, indicate a salinity of approximately 34.5 PSU. The long mooring recorded slightly higher salinity levels, ranging from 34.6 to 34.8 PSU. A higher salinity can increase the floc size and the settling velocity of the clay [16]. Figure 2.2c illustrates that dissolved oxygen levels are nearly zero at depths ranging from 300 to 600 m. Below this range, oxygen levels increase, reaching 4.5 mg/L near the seabed. The mooring data confirmed that dissolved oxygen levels remained relatively constant throughout the 7.5-month observation period.

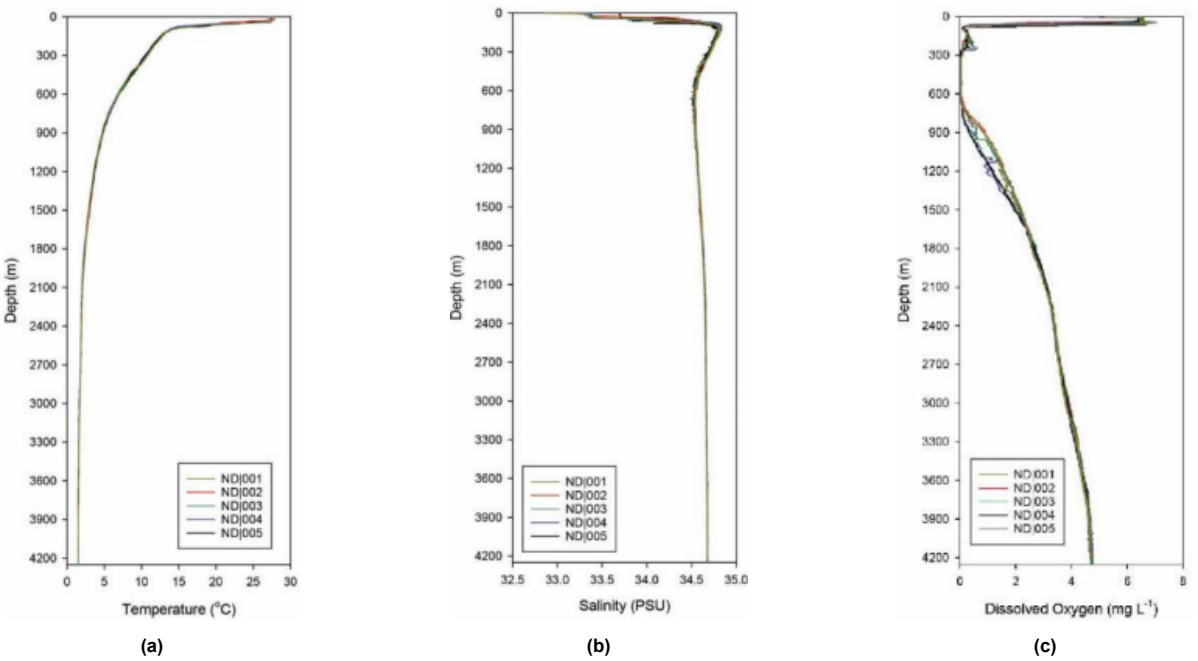


Figure 2.2: Water properties of the NORI-D area in October 2019, with (a) the in-situ temperature profile, (b) the Salinity profile and (c) the dissolved oxygen profile [2]

A Belgian company, Global Sea Mineral Resources NV (GSR), also shared its results on the environmental and water properties of the CCZ [17]. It deployed multiple moorings to gather data on water properties at different depths. The area it investigated that is closest to NORI-D is the GSR B6 area. The investigated properties, including temperature, salinity, density and dissolved oxygen, were measured over a nearly 4-year period. The results are displayed in Figure 2.3.

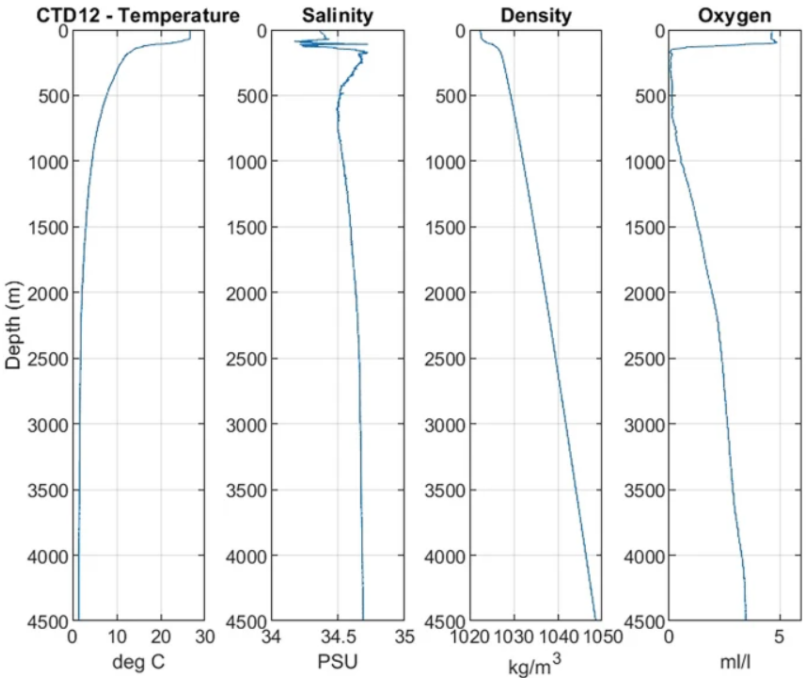


Figure 2.3: Water properties of the GSR B6 area in the CCZ [17]

For Deep Sea Mining (DSM), the near-bottom properties are most relevant. In Figure 2.3, it can be observed that as the depth increases, the temperature approaches 1.5 °C and the salinity approaches 34.7 PSU. The density has a linear relationship with depth due to the increasing hydrostatic pressure, which can reach values of approximately 40 MPa at a depth of 4 km. After a significant drop at a depth of 200 m, the oxygen level increases as the descent continues to the seabed. All properties tend to remain relatively constant over time. These findings align closely with those from NORI-D, increasing confidence in the accuracy of the NORI-D data. An overview of the properties of both areas is given in Table 2.1.

Table 2.1: Water properties of the NORI-D and GSR B6 areas

Water property	NORI-D	GSR	Unit
Temperature	1.5 - 2	1.5	°C
Salinity	34.6 - 34.8	34.7	PSU
Density	-	1048	kg/m^3
Oxygen	4.5	3.5	mg/L, ml/L

Besides water properties, GSR also investigated the current in area B6 [17]. It measured the current velocity and direction at varying depths for nearly four years. Since the near-bottom depth is the most relevant, only data from the near-bottom (< 7 m) current velocity are considered. The near-bottom current velocity of B6 is displayed in Figure 2.4. The red line is for the relevant mooring. The velocity remains constant over the depth until an elevation of 25 m, after which it significantly increases. Then the velocity continues to rise slightly to around 4.5 cm/s just above the seabed. This is higher than the NORI-D average near-bottom current. The considerable distance between the areas can explain this.

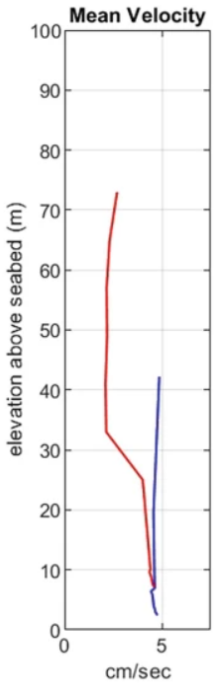


Figure 2.4: Near bottom current velocity at the GSR B6 area, with MOR007 in blue and MOR009 in red [17]

2.2. Sediment Composition and Characteristics

The maneuverability of the SNC and its interaction with the soil are highly dependent on the type of soil present. The area of the CCZ is extensive and does not consist of just one soil type, but in multiple areas throughout the CCZ (NORI-D, InterOceanMetal and GSR) is a seabed layer of up to 2 meters deep found that consists of soft silty clay [15] [3] [8] [2]. This clay has a semi-liquid top layer that will be disturbed during the mining process [3]. The ratios of silt and clay, as well as the types of clay, can vary between zones and even within the same zone. In tests conducted by The Mining Company (TMC) in NORI-D [15], multiple sediment compositions were identified and categorised into three groups labeled Unit 1, Unit 2, and Unit 3. All compositions were found in the NORI-D area but differ in depth, color and properties. The soil colors ranged from very dark brown to dark yellow-brown, with soft silty clay present throughout [15] [2]. A summary of these findings is illustrated in Table 2.2. Since the higher layers are most relevant and Unit 3 is barely observed, this study focuses on Units 1 and 2.

Unit 1, characterised as a very soft dark brown silty clay, is found widely across the site. This unit primarily represents the top layer of the seabed and is, therefore, most relevant to this research. Its thickness ranges from 5 cm to 16 cm, with a median of around 11 cm. This cohesive soil exhibits high plasticity but behaves like a semi-liquid. It causes the SNC to experience sinkage, low traction and slip [18].

Unit 2 is also often present in NORI-D and should be taken into consideration. It differs clearly in color from Unit 1, presenting as very soft, yellowish-brown silty clay. Like Unit 1, Unit 2 is a cohesive soil with high plasticity, but it is often a crustal layer located between 0.20 m and 0.50 m below the seabed. The undrained shear strength in this layer exhibits a sharp increase followed by a decline over a relatively short depth range. The clay activity ranges between 1.4 and 2, which possibly indicates the presence of the clay mineral montmorillonite [15].

Table 2.2: Summary of the soil types obtained by field measurements in NORI-D by TMC [15]

Unit	Soil Description	Top Depth (mbsf)	Thickness (m)	Typical Su (kPa)	Frequency	Comments
Unit 1	Very soft dark brown silty CLAY / Clayey SILT	0.00	0.05 - 0.16	1.0 – 4.0	Across the site	C3 reports describe the immediate surface as 'Semi-liquid', whilst the C6a/b reports describe the same material as (Hemi)pelagic drape
Unit 2	Very soft yellowish brown silty CLAY, often mottled dark brown*	0.08 – 0.16	0.45 – 1.10+	3.0 – 6.0 Occasional value as high as 10.0 recorded	Across most of the site	Mottling indicative of bioturbation and incorporation of Unit 1 material
Unit 3	Very soft dark yellowish brown silty CLAY, mottled dark brown	0.60 – 1.20	>1.40m	1.5 – 5.0	5 GC's only, in proximity to BC_114 & BC_115	Trending towards normally consolidated based on the seabed CPT results

* Variations recorded in the colour descriptions which appear from the data to have no effect on the soil material parameters.

Some manoeuvrability and nodule pick-up tests with the SNC on the seafloor of NODI-D have already been performed. In addition to the soil tests for the NORI-D area, TMC conducted an extra campaign focusing on the PMT area. It focused on high-definition characterisation of the upper 0.50 m layer of the seabed [15]. Box cores and seabed Cone Penetration Test (CPT) data were used. The results are shown in Table 2.3. The mean thickness of Unit 1 is 0.11 m. These results confirm that the soil in the test area is consistent with the findings of the previous site investigation. It is observed that the samples in the area have a more consistent soil composition. This can be attributed to the smaller test area and more uniform bathymetry.

Table 2.3: Summary of the soil types obtained by field experiments in the SNC test area by TMC [15]

Unit	Soil Description	Top Depth (mbsf)	Thickness (m)	Typical Su (kPa)	Frequency	Comments
Unit 1	Very soft dark brown CLAY	0.00	0.04 - 0.16	1.4-2.2*	Across the site	
Unit 2	Very soft brown CLAY, frequently mottled with dark brown	0.04 - 0.16	>0.4	2.0-5.2*	Across the site	

* Soil shear strength measured using Torvane in split samples and Laboratory Vane directly into box core

GSR conducted sediment tests in its contract area [8] and identified three main sediment types: A, B, and C. Sediment A is often found as the uppermost layer of the seabed, characterised as a brown to dark yellow-brown sandy mud. Sediment B is further categorised into B1 and B2. B1 is a yellow-brown to light yellow-brown mud that can appear either sandy or as a homogeneous mud. In contrast, B2 has intermediate colors between sediments A and B1, ranging from greyish-brown to brown. Facies C is less common and varies in color from dark grey to brown. The most frequently observed sediment pattern in area B4S03, a part of the GSR contract area, is A-B. The distribution of these sediment types aligns with the findings in the NORI-D area. Additionally, GSR discovered four different clay

mineral groups in the sediment: illite, smectite, chlorite, and kaolinite. The mineral ratios were relatively consistent across all samples, with the average percentages presented in Table 2.4.

Table 2.4: The estimated clay content of the top layers for the Peru Basin [19] and GSR (average of the box cores publicated in its EIS) [8]

	Illite (%)	Smectite (%)	Chlorite (%)	Kaolinite (%)
GSR	48.3	36.4	10.3	4.9
Peru Basin	28.0	35.1	31.8	5.15

Table 2.5: Liquid limit for the different deep-sea clay minerals [20] [21]

Illite (%)	Montmorillonite (%)	Chlorite (%)	Kaolinite (%)
60 - 120	100 - 900	43 - 46	35 - 100

P.E. Halbach and A. Abram [3] conducted a study on the surface sediment in the CCZ. They identified three East-West zones. The area most relevant to this research is the InterOceanMetal (IOM) region, which is the most Eastern area they studied. The semi-liquid top layer of the IOM area consists of siliceous silty clay and ooze, while the underlying layer is composed of pelagic clay, zeolitic clay and a zeolitic crust. In the IOM area, two clay colors are present: reddish-brown and yellow-brown. The reddish-brown pelagic clay is primarily found in the northern part of the IOM, whereas the yellow-brown clay is more predominant in the southern part. The southern clay aligns better with the altitude and sediment color of the NORI-D area. Halback and Abram distinguished two types of yellow-brown clay: one is siliceous silty clay found throughout the IOM, and the other is a mixture of radiolarian ooze and diatom ooze. In the NORI-D, mostly siliceous silty clay is found. As the color of the clay does not precisely indicate its type, it can serve as an additional validation.
Soil properties can significantly influence the amount of sediment suspended by the tracks. Essential properties are expected to be particle size, unit weight, shear strength, adhesion, and water content. During the recovery of the soil samples to the surface, their properties may change, making it challenging to collect accurate data. Given that soil types vary across different zones of the CCZ, it is essential to utilise data from NORI-D if available. TMC collected samples from the NORI-D site and shared the findings [15], which are presented in Table 2.6. As mentioned earlier in this section, TMC conducted a more detailed examination of the Pilot Mining Test (PMT) area. The results are summarised in Table 2.7. The values obtained provide a more precise range and align with the ranges presented in Table 2.6. The data are gathered from subsamples tested in the laboratory and on-site (CPT). It is important to note that the ranges in both Tables are derived from the minimum and maximum values across all samples. For instance, the maximum bulk density does not correspond to the maximum dry density, as they originate from different samples. Nevertheless, these ranges offer a valuable overview of the soil properties. To evaluate the reliability of TMC's data, reference data from additional tests will be utilised.

Table 2.6: Soil properties measured in the NORI-D area by TMC [15]

Property	Unit 1	Unit 2	Unit
Depth	0.0 - 0.16	0.05 - 1.10+	m
Submerged unit weight	2.33	2.33	kN/m^3
Bulk density	1.16 - 1.46	1.19 - 1.06	t/m^3
Dry density	0.26 - 0.53	0.29 - 0.46	t/m^3
Undisturbed shear strength	1 - 4	3 - 6	kPa
Remoulded shear strength	0.1 - 0.38	0.5 - 1.0	kPa
Water content	200 - 364	113 - 356	%
Liquit limit	141 - 229	190 - 220	%
Plastic limit	32 - 100	40 - 50	%
Soil sensitivity	5 - 15	5 - 100	-

Table 2.7: Soil properties measured in the PMT test area by TMC with a higher density of tests in the area [15] and the data obtained by GSR for comparison

Property	Unit 1	Unit 2	GSR	Unit
Depth	0.0 - 0.16	0.04 - 0.44+	0.0 - 0.25	m
Bulk density	1.34 - 1.38	1.2 - 1.43	1.25 - 1.45	t/m^3
Dry density	0.31 - 0.36	0.31 - 0.43	-	t/m^3
Undisturbed shear strength	1.4 - 2.2	2.0 - 5.2	0 - 9.5	kPa
Remoulded shear strength	-	0.23 - 1.1	-	kPa
Water content	278 - 329	193 - 324	175 - 275	%
Soil sensitivity	-	4 - 10.3	-	-

GSR also examined the sediment properties in its contract area [8]. It was found that the water content primarily falls within the range of 175% to 275%, with most samples averaging around 200%. Outlier values exceeding 400% were excluded as they were deemed to be measurement errors. The bulk density ranged from 1.25 t/m^3 to 1.45 t/m^3, with 1.35 t/m^3 being the most common value. The undrained shear strength was measured for each box core, revealing a general trend of increasing shear strength from 0 kPa at the seabed surface to a maximum of 9.5 kPa at depths of 20 to 25 cm. In one of the samples, it is observed that the shear strength increases rapidly within the first 3 cm, reaching 4 kPa, after which the increase continues at a slower rate. All these properties align with the soil characteristics observed in the NORI-D area.

B. Grupe et al. [19] conducted a study on deep-sea sediments from the Peru Basin, located Southeast of the CCZ, which, according to Halbach and Abram, exhibits similar soil conditions and has a semi-liquid top layer [3]. They measured the sediment unit weight, shear strength, and water content. Grupe et al. [19] found a water content of nearly 85% at the sediment surface. The water content rapidly decreases to 73% at a depth of approximately 10 cm and approaches 70% by 30 cm. These values are significantly lower than those observed by TMC in the NORI-D area. The shear strength at the surface is below 0.1 kPa, which is extremely low but understandable due to the semi-liquid layer. It increases to approximately 3 - 5 kPa within the first 10 - 15 cm and rises rapidly to 10 kPa at 30 cm, aligning with TMC's results. It is noteworthy that, despite the significant difference in water content, the strength of the clay and the presence of a semi-liquid top layer are consistent with the strength of CCZ clay. Table 2.4 highlights a difference in mineral composition between the clay from GSR and that of the Peru Basin, which could explain variations in soil properties. The Peru Basin sediment contains a higher fraction of chlorite and a lower fraction of illite compared to the GSR sediment. W.A. White and E. Pichler [22] found that, among the four primary minerals present in the deep-sea clay, chlorite has the lowest water absorption capacity. Since the smectite and kaolinite fractions are within a similar range for both sediments, the higher chlorite content can account for the lower water content observed in the Peru Basin. Additionally, when comparing the liquid limit results for clay minerals reported by B. Widjaja and K. Kurniawan [20] with those found by L. Daoudi et al. [21], it is evident that chlorite has a significantly lower liquid limit. This is also confirmed by the findings of J.K. Mitchell and K. Soga [23]. An overview of the liquid limits found for all minerals is given in Table 2.5. This indicates that soil particles detach at a lower water content, leading to a low shear strength even at relatively low water content levels.

Table 2.8: Particle sizes for three different areas within the CCZ

NORI-D	GSR	IOM
73% - 99% < 32 μm 13% - 88% < 2 μm	d_{50} = 12 μm	88.6% < 4 μm

NORI reported that their samples contained between 13% and 88% particles smaller than 2 μm, with 73% to 99% passing through a 32 μm sieve [2]. Halbach and Abram [3] noted that the grain size distribution in the IOM area consists of 88.6% sediment particles smaller than 4 μm, classifying most of the sediment as clay or silty clay. Additionally, GSR conducted field experiments in the eastern part of the CCZ, assessing not only water properties but also soil properties. They found that the average grain diameter of the sediment (d_{50}) is 12 μm [24]. This is a significant fluctuation, which may indicate

different soil types or varying water content. The value of d_{50} is relatively high compared to clay particles, which may be due to a large fraction of silt. An overview of the available particle size data for these areas is presented in Table 2.8. From these particle sizes, it can be concluded that NORI-D and IOM contain larger fractions of clay. For GSR, determining the clay fraction is more challenging, as it only provides the d_{50} value and the size is too large for clay particles. A complete particle size distribution for the areas would enable a more accurate estimation of the sediment type.

3

Seabed Nodule Collector Tracks

The Seabed Nodule Collector is equipped with tracks, enabling it to navigate across the seabed. While various types of tracks exist, they all operate on the same principle: a belt is looped around guiding wheels and driven by a sprocket (see Figure 3.2c). The tracks utilised by the SNC are typically found on snow groomers, as illustrated in Figure 3.1. These tracks are specifically engineered to provide traction on snowy surfaces and steep slopes. For the SNC, the widest available tracks (2 m) have been selected and their length has been increased to help distribute weight, enhance traction and generate sufficient bearing capacity. Traction tests [25] and the PMT indicate that these modifications are effective for achieving adequate grip on the seabed of the CCZ.

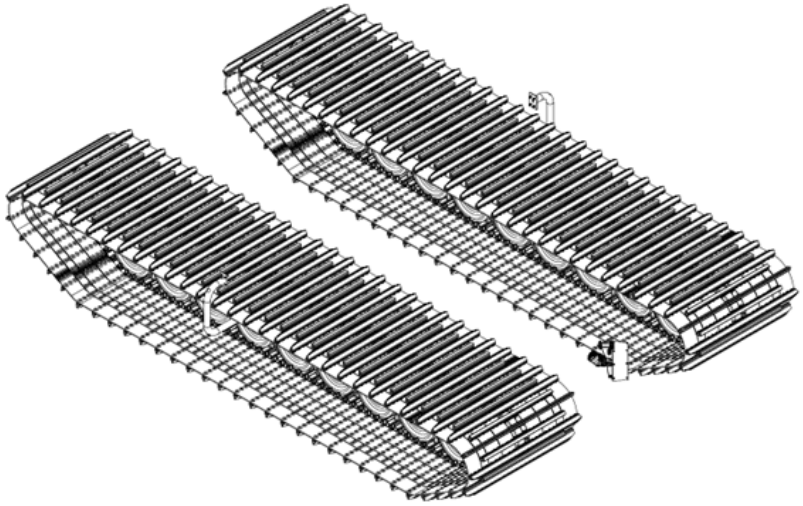


Figure 3.1: The SNC tracks [26] (edited)

This chapter will provide an overview of how the tracks operate and the factors that lead to sediment suspension. It will begin by describing the key components and dimensions, followed by an explanation of how the tracks function in clayey soil. Finally, the chapter will explore the sources of sediment suspension and compare it to a previous field study conducted by GSR.

3.1. Track Design

The tracks of the SNC are made of a rubber belt with aluminum 6061 grousers attached. It utilises two different grousers: the high grouser, measuring 125 mm in length, and the low grouser, measuring 75 mm in length. The tracks are guided by nine track rollers underneath and one front idler at the front.

The tracks are driven by a sprocket located at the rear. Unlike most tracks that rely on a track chain to engage with the sprocket, the SNC has a different design: the rubber belt has an opening in the middle, allowing the sprocket to grip the grousers directly. The overall length of the tracks, including the grousers, is approximately 8.7 meters, although the part in contact with the seabed is shorter, measuring 6 meters. The tracks enter and exit the seabed at a 30-degree angle. The total height of the tracks is 1.424 m. All key dimensions and components are illustrated in Figure 3.2.

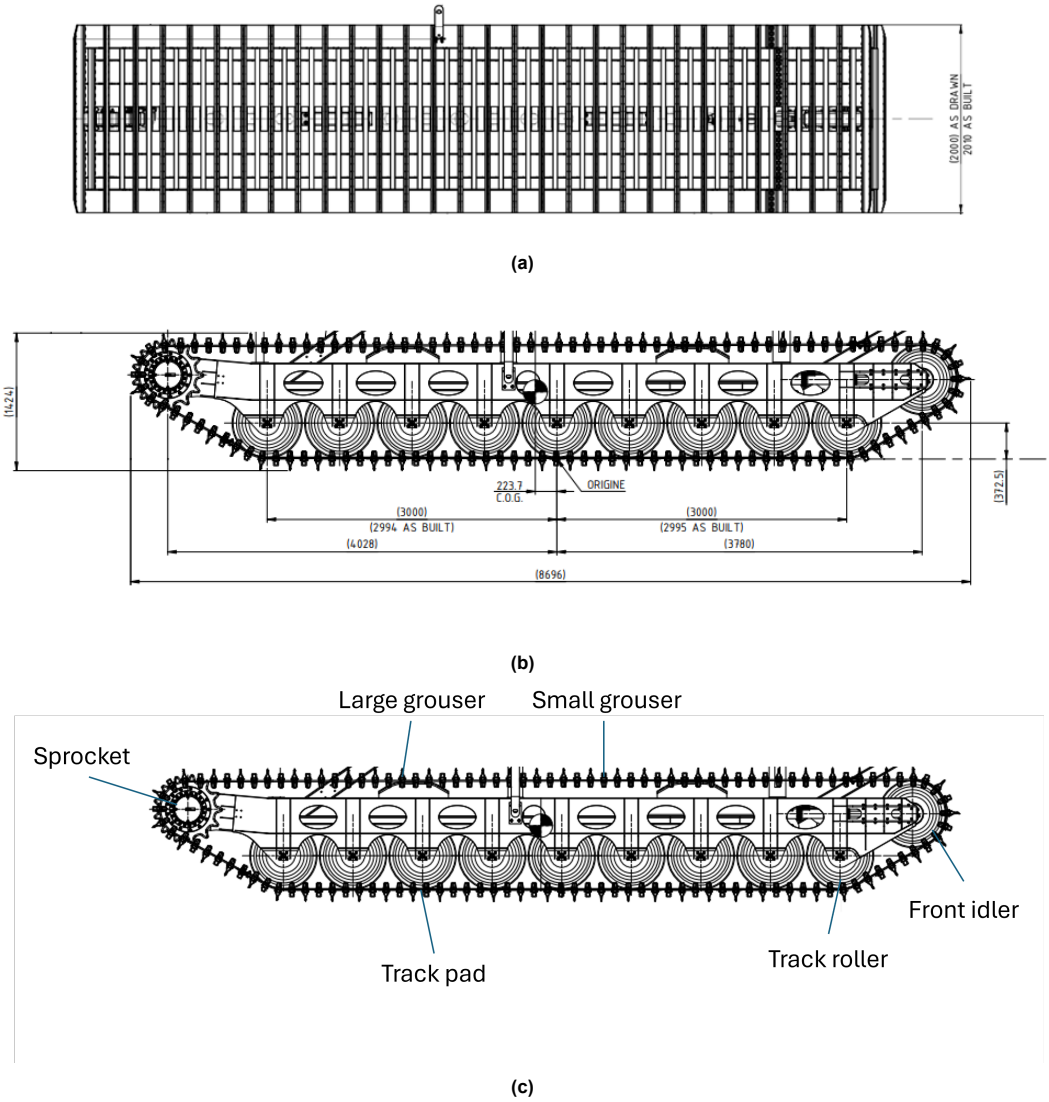


Figure 3.2: Technical drawing of the SNC tracks, with (a) the top view of the tracks [27] (edited), (b) the side view of the tracks and (c) showing the relevant parts [26] (edited)

3.2. Behaviour in Deep-Sea Sediment

In the previous chapter, it is established that the sediment in the NORI-D area is primarily composed of very soft silty clay. The uppermost layer, extending to a depth of 0.16 meters, exhibits a shear strength ranging from 1.4 kPa to 2.2 kPa and has a semi-liquid characteristic. The SNC collects nodules using a Coandã nozzle, which also removes the top layer of the seabed in the process. For this study, a consistent sediment layer of 4 cm is assumed, meaning that the effective seabed surface reflects the soil properties at this depth. Although the shear strength increases slightly, it remains very low, resulting in the tracks sinking approximately 6 cm [13] into the seabed. This was observed during the Pilot Mining Test (PMT) conducted by Allseas in the NORI-D area. J.Y. Wong [28] developed a method

to calculate the seabed penetration based on the pressure exerted by the tracks on the seabed and the soil properties. The equation used is as follows:

$$z = \left(\frac{p}{k_c/B + k_\phi} \right)^{1/n} \tag{3.1}$$

p is the pressure exerted by the tracks on the seabed, B is the total width of the tracks, k_c (kN/m^{n+1}) and k_ϕ (kN/m^{n+2}) are the cohesive and frictional modulus of terrain deformation and n the exponent of terrain deformation. J.Y. Wong [28] found values of n ranging from 0.11 to 1.6 for various types of soil and from 0.11 to 0.7 for different clayey soils. k_c, k_ϕ and n are determined by comparing test results obtained from applying pressure to plates of varying widths, which are pushed into the soil, measuring the seabed penetration corresponding to a given amount of pressure. k_c, k_ϕ and n are still to be determined for the NORI-D terrain. Therefore, for this research, the 6 cm from the pilot mining test will be used. After accounting for the removal of the top 4 cm by the nozzle, the tracks drive over soil at a depth of 10 cm. The grousers have a length of 12.5 cm and, therefore, reach a depth of 22.5 cm.
Although the tracks are straight at the bottom, the pressure distribution is uneven. The load on the tracks is transmitted through the track rollers, which generate peak stresses at their contact points with the seabed. This is depicted in Figure 3.3. According to J.Y. Wong [28], seabed penetration is primarily influenced by peak stress rather than average stress. To reduce peak stresses, track rollers can be placed closer together or a greater number of smaller rollers can be used, as seen in the Churchill V and the Panther A tanks.

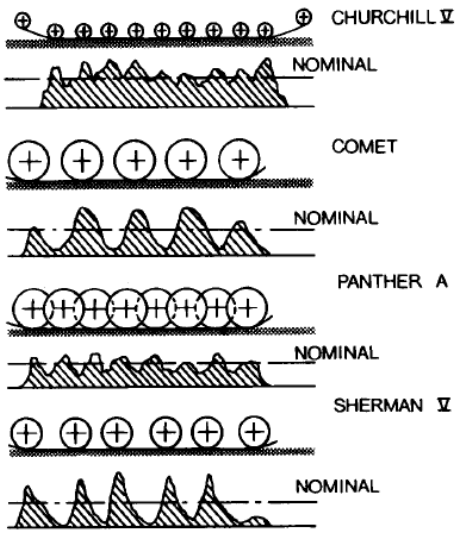


Figure 3.3: Measured normal pressure distribution at a depth of 23 cm below the soil surface under various tanks on land, with the tank type indicated on the right side of the figure [28]

As a result of seabed penetration, soil undergoes compaction and plastic deformation. Compaction is typically relevant for sandy soils and snow, while plastic deformation is more relevant for clayey soils [29]. Given that the sediment in the NORI-D area is primarily clay, this research assumes that plastic deformation is the dominant effect. seabed penetration leads to the formation of ruts created by the tracks, generating a motion resistance. This is the resistance encountered by the vehicle tracks as a result of seabed penetration during driving. For this analysis, motion resistance can be estimated using the following equation [29]:

$$M_r = s_u \cdot N_c \cdot B \cdot z \tag{3.2}$$

s_u is the undrained shear strength, N_c the bearing capacity factor (= 5.14 [29][30]), B the width of the track (times 2) and z is the seabed penetration of the tracks. For soil that is dominated by cohesion

and where the internal friction angle is zero, the bearing capacity factor $N_c = 2 + \pi = 5.14$ [31]. The geomechanical field widely accepts this value for soils with a high clay content. Equation 3.2 is based on the assumption of purely plastic deformation of the soil. In this case, the work needed to plastically deform the soil at a depth z is equal to the work required to penetrate the soil with the tracks to the same depth. The motion resistance over different seabed penetration levels is calculated for the SNC in NORI-D and the results are illustrated in Figure 3.4. The shear strength of the NORI-D clay increases linearly with depth, ranging from 1.4 kPa at the surface to 2.2 kPa at a depth of 0.16 m. Therefore, the shear strength is adjusted for each specific seabed penetration value.

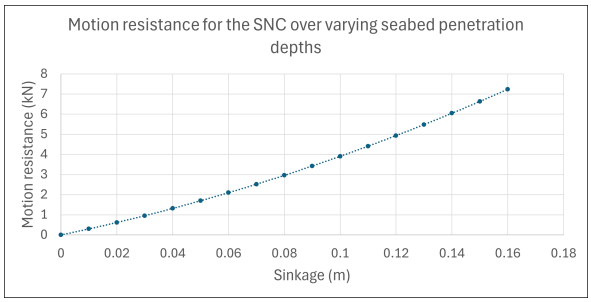


Figure 3.4: Motion resistance of the SNC tracks for a varying seabed penetration with a linear increasing undisturbed shear strength over depth

According to J.Y. Wong [28], in cohesive soils like the NORI-D sediment, the undrained shear strength governs traction. This shear strength decreases when the soil is disturbed, meaning that the traction between the tracks and the seabed decreases as the tracks and grousers deform the soil. As the tracks move forward, the soil becomes increasingly disturbed, resulting in the greatest disturbance occurring at the rear of the track. To address this change in traction, N. Morgan et al. [29] introduce the α factor, as shown in Equation 3.3.

$$F_{available} = \alpha \cdot F_{max} \tag{3.3}$$

where $F_{available}$ is the traction after disturbance of the soil and F_{max} is the traction before disturbance. According to N. Morgan et al. [29], the α value ranges from 0.4 (indicating full disturbance) to 1.0 (indicating no disturbance). The value 0.4 corresponds to a soil sensitivity of 2.5. The sensitivity of the NORI-D area Unit 1 soil is in the range of 5 to 15. This means that the α-factor for Unit 1, when fully disturbed, falls within the range of 0.067 to 0.2. The maximum tractive effort for soil with both adhesion and friction can be calculated using the following equation:

$$F_{max} = A \cdot c + W \cdot tan(\phi) \tag{3.4}$$

Where A is the contact area of the tracks on the soil, c and ϕ are the cohesion and angle of internal friction of the terrain respectively and W is the normal load on the track [28]. The internal friction angle for the NORI-D clay is not reported in the literature. However, it is expected to be very low due to its high water content and clay fraction. Data from the Pilot Mining Test indicate that the rotational speed of the tracks exceeds the forward speed of the collector. This suggests that the tracks are slipping, with slippage reaching up to 3% of the tracks' displacement when moving in a straight direction [32].
The SNC employs skid-steering for turning, which involves maintaining thrust in the outer track while reducing thrust in the inner track. For effective skid turning, it is essential to maintain sufficient traction on one track to ensure forward thrust and to overcome the turning resistance during the turn. The outer track must also overcome the combined motion resistance of both tracks [29]. However, skid-steering is not the focus of this study. The emphasis here is on straight, constant forward movement.
Previous tests conducted by Allseas [25] indicated that clay tends to adhere to the tracks. Anticipating this issue during the design of the NSC, it was expected that clay adhesion could lead to potential complications. One concern was that traction could decrease when the tracks and grousers re-enter the seabed while still coated with adhering clay. Another issue could arise from sediment and stones

getting between the sprocket and the track, potentially causing damage or blockages. To mitigate these problems, jets have been installed to direct water at the sprocket and tracks from two different angles, as shown in Figure 3.5. Footage from a Remotely Operated Vehicle (ROV) during the Pilot Mining Test revealed that only a minimal amount of clay adhered to the tracks (see Figure 3.6), forming a mere thin film. This is likely to have a negligible impact on traction. This suggests that conditions such as adhesion can vary significantly when saturated under laboratory-based conditions and at greater depths.

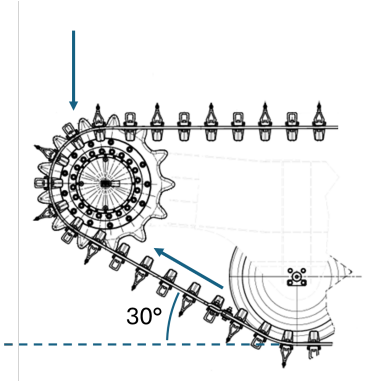


Figure 3.5: Locations of the jets for cleaning the tracks [27] (edited)

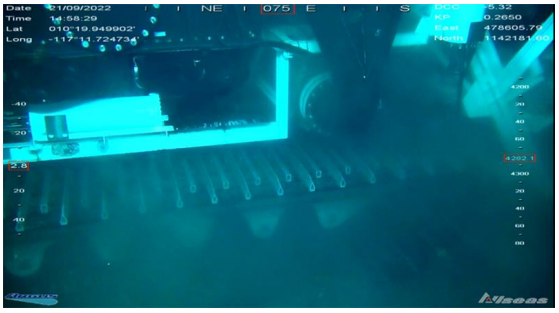


Figure 3.6: Tracks of the SNC during the PMT without track cleaning [33]

The situation depicted in Figure 3.6 represents the tracks during motion. When the collector is stationary and the contact time between the tracks and the clay increases, the pull-out force also increases [34]. Broeren [18] attributes this to the dissipation of excess pore pressures and the soil flowing back around the object. This process leads to an increase in adhesion forces, which may result in a larger amount of clay adhering to the tracks.
To gain traction, the tracks are equipped with grousers. A track without grousers relies on shear interaction between the track belt and the soil to generate traction. By introducing grousers, traction is instead derived from soil-to-soil shear [35]. The grousers are embedded into the seabed and as the vehicle moves, the tracks experience slip, since traction is only developed once the grousers begin to slip relative to the soil [35]. The slipping ceases once sufficient traction is generated to propel the collector. However, during this slip phase, the grousers also deform the sediment bed.

3.3. Kinematic Clay Disturbance Model

The SNC tracks are designed to provide sufficient traction for navigating over the seabed. It is expected that the tracks will generate a plume through two primary actions. The first action involves cleaning the tracks of adhering sediment via jetting. The second action relates to the interaction with the seabed during movement, which can be divided into three aspects: the seabed penetration of the tracks into the seabed, the scooping action as the grousers pull through the sediment at the last track roller and the pulling of the grousers out of the seabed. To gain a better understanding of the resulting plume and validate these expectations, footage from the PMT is analysed, showing the SNC operating without the collecting system activated (with only the tracks in motion). A plume is generated, confirming expectations about its presence.
Ultimately, the aim is to estimate the amount of sediment suspended by the tracks, but this proves to be highly complex. Even under the assumption that plastic deformation occurs due to the high clay content in the soil, determining the ratio of sediment that becomes suspended versus what is relocated on the seabed remains challenging. To address this, a kinematic model is developed based on the assumption of plastic deformation to estimate the amount of relocated sediment. By conducting tests, this model can be refined to provide a more accurate estimation of sediment suspension caused by the tracks. The kinematic model will assess the impact of each sediment suspension source and its relative significance. Given the soft clay, a substantial portion of the disturbed sediment is likely to become suspended. This section will examine all factors contributing to sediment suspension in greater detail. Observations from the footage will offer further insights into the origins of the plume and

the interaction between the tracks and the seabed. Finally, the theories underpinning the kinematic model will be discussed.

3.3.1. Seabed Penetration

The tracks of the SNC penetrate the seabed to a depth of 6 cm. The top layer of the soil often behaves as a semi-liquid, indicating that it is very soft and easily deformed. Because the soil is so soft, it easily becomes suspended when deformed. This is evident in the footage from the PMT, where a plume forms at the front of the tracks even when no other functions are activated and no additional environmental influences are observed aside from the forward movement of the tracks. For the seabed penetration aspect, the disturbed volume is equivalent to the volume of the submerged tracks and can be calculated using the following equation:

$$V = z \cdot A_{tracks} \cdot n_t \tag{3.5}$$

Where z represents the penetration of the tracks into the seabed, A_{tracks} is the total contact area of the tracks on the seabed and n_t is the number of tracks. This volume consists of a mixture of water and sediment particles. To quantify the sediment content, the sediment fraction must be calculated. This involves converting the volume into mass (as shown in equation 3.6) and then subtracting the water fraction (as shown in equation 3.7). This results in 60.6 kg of disturbed sediment for every meter the SNC drives forward.

$$m_{tot} = V \cdot \frac{\gamma_s + \gamma_w}{g} \tag{3.6}$$

$$m_s = \frac{m_{tot}}{u + 1} \tag{3.7}$$

Where m_{tot} is the total mass of the removed volume of the seabed, γ_s is the unit weight of the soil, γ_w is the unit weight of sea water (10.28 kN/m^3 from Table 2.1), g is the gravitational acceleration, m_s is the mass of the sediment fraction and u the water content. A more detailed calculation is given in Appendix A.

3.3.2. Grousers

The tracks have two types of grousers: high grousers (125 mm) and low grousers (75 mm). The grousers are used to enhance traction [35], but they also contribute to sediment suspension as a side effect. To generate traction, the grousers are fully embedded in the soil. As the grousers leave the seabed, they twist through the soil, likely to disturb it. Additionally, since the grousers do not fully emerge from the seabed after the twist, some sediment is scooped up during the process of pulling them out. To determine the amount of disturbed sediment by the grousers, the calculation is divided into two parts: first, the scooping effect is assessed, followed by the pull-out process. In Figure 3.7, the grousers and their relevant dimensions are illustrated. For the calculations, the grousers are simplified as plates with the original width and length but no thickness.

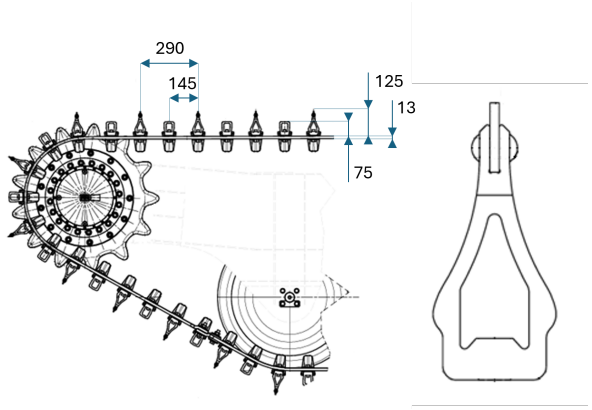


Figure 3.7: Grousers of the SNC tracks with the dimensions in millimeters [27] [36] (edited)

The track pads are horizontal and the grousers are vertical at the bottom of the tracks. At the rear, the tracks move upward at a 30-degree angle after turning around the last track roller (see Figure 3.5. During this 30-degree twist, the grouser remains in contact with the soil, creating a scooping effect, as illustrated in Figure 3.8a. The brown line represents the seabed surface after seabed penetration, and only the soil beneath this line is influenced by the grouser, as the seabed penetration has already deformed the soil above. The outer circle indicates the trajectory of the grouser when the track roller makes a full spin without horizontal displacement. The red area between the surface and the trajectory of the grousers represents the soil that a single grouser has deformed. This area, marked in red (see Figure 3.8a), measures $4.75{\cdot}10^{-3}$ m^2 for the high grouser and $1.64{\cdot}10^{-3}$ m^2 for the low grouser. It is assumed that the shear line in the clay at the edge of the grouser, formed when a scoop is removed from the clay, is minimal due to the softness of the soil. Therefore, for this estimation, the shear line is neglected and only the trajectory of the grousers is considered. This area is multiplied by the total width of the grouser and the number of grousers per meter to calculate the volume removed per meter of forward movement. Then, Equations 3.6 and 3.7 are applied to determine the quantity of sediment deformed per meter due to the scooping effect. The amount of deformed sediment per meter of forward movement due to the scooping effect of the high grouser is 18.2 kg and for the low grouser is 4.78 kg. This results in a total of 22.9 kg of deformed sediment caused by the scooping mechanism. The calculations and grouser trajectory are detailed in Appendix A.

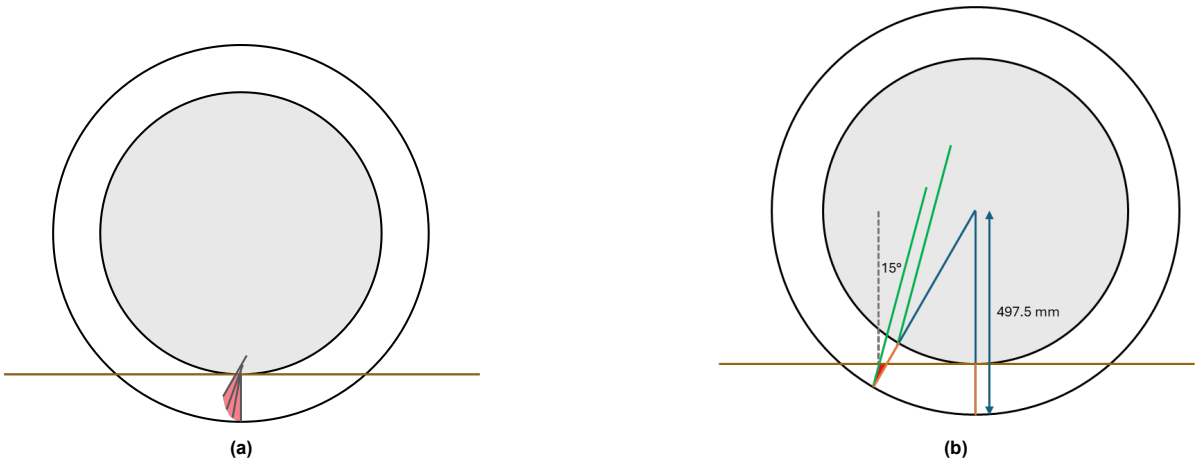


Figure 3.8: Area of soil that is deformed by a single grouser (indicated in red) with the track roller in grey and the outer diameter as the trajectory of the grouser, with (a) due to the scooping effect, with the grouser positions at 0, 10, 20 and 30 degrees, and (b) due to the pull-out process

After the twist, a part of the grouser remains embedded in the seabed. While the grouser moves upward at a 30-degree angle relative to the entire track, the tracks themselves continue to advance forward over

the seabed. For the pull-out process, it is important to examine the grouser-soil interaction, specifically the displacement of the grouser relative to the seabed. For every meter the tracks move forward, the grousers shift 0.134 m forward when they are pulled out. This results in a pull-out angle of 15 degrees relative to the seabed's normal, with the trajectory of the grouser illustrated by the green lines in Figure 3.8b. The soil that is still unaffected by the seabed penetration and scooping effects, which will be deformed during the pull-out, is the area between the green lines and beneath the seabed. This area is highlighted in red in Figure 3.8b and measures $4.32{\cdot}10^{-4}$ m^2 for the high grouser and $1.41{\cdot}10^{-5}$ m^2 for the low grouser. By multiplying this area by the width of the grouser and the number of grousers per meter and then applying Equations 3.6 and 3.7, the amount of deformed sediment per meter of forward movement is calculated as 1.65 kg for the high grouser and 0.0410 kg for the low grouser. This results in a total of 1.69 kg of deformed sediment due to the pull-out effect.

Table 3.1: Summary of the sediment disturbance per meter of driving forward for all plume generation sources [12]

seabed penetration (kg/m)	Scooping (kg/m)	Pull-out (kg/m)	Total (kg/m)
60.6	22.9	1.69	85.3

3.3.3. Jets and Adhesion

As previously noted, traction tests conducted by Allseas indicated that sediment tends to adhere to the tracks [25]. However, footage from the PMT reveals the opposite. This contradiction can be attributed to the different soil and water conditions at a depth of 4,300 m compared to those in laboratory conditions. Since the conditions observed during the pilot mining test are more representative for this study, all future assumptions will be based on these observations rather than the laboratory traction tests.
Only a thin film of clay adheres to the tracks and grousers. When this layer is jetted off, it will be a small percentage of the total sediment suspension generated by the tracks. This thin layer is unlikely to have a significant impact on traction and may not require cleaning. Therefore, if jetting were removed, there would be no sediment suspension from adhesion in combination with jetting. For estimating the quantity of deformed sediment, the adhesion does not need to be factored in, as all sediment affected by the motion and position of the tracks is already accounted for in the seabed penetration, scooping, and pull-out processes.

3.4. Collector Field Test

In 2021, Global Sea Mineral Resources NV (GSR) conducted a test using their first nodule collector prototype in the CCZ at a depth of 4,500 meters [12]. The collector was equipped with sensors and specific maneuvers were developed to study the sediment plume created by the collector. These maneuvers, referred to as "selfies", involved the collector making three 90-degree turns to cross its path and analyse the plume it generated (see Figure 3.9). The tests were conducted at three different sites, with varying loop distances, to examine the sediment plume under different conditions and at various intervals after soil disturbance.

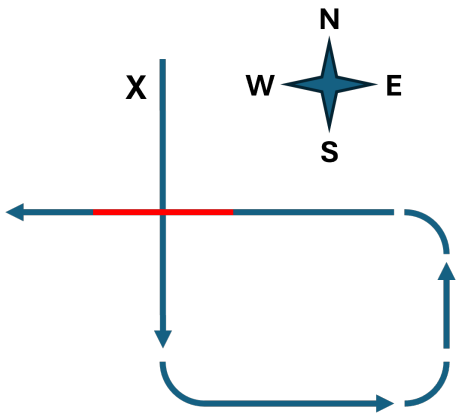


Figure 3.9: Top view of the selfie maneuver

The collector (L = 9.7 m, W = 4.8 m, H = 4.2 m [37]) utilises four pumps to generate the flow for the nodule collecting nozzle. Most tests operated with all four collecting system pumps active, except one test utilised only its tracks with no active pump. While an active pump provides a more comprehensive assessment of the total sediment suspension, this study specifically focuses on the sediment suspension caused solely by the tracks, making test B1 particularly relevant. A summary of the test is illustrated in Table 3.2. The collector drove through the plume from East to West at a speed of 0.36 m/s, with the measured concentration displayed in Figure 3.10. Notably, the collector did not engage the sediment plume until after the crossing, while all other tests indicate sediment plumes on both sides of the crossing. However, these tests show a wider plume following the crossing, likely because the plume at that side had more time to develop.

Table 3.2: Summary of the B1 selfie test [12]

Selfie	L_3 (m)	U_c (m/s)	t (min)	Initial heading (°T)	Slope (°)	Downslope direction (°T)
B1	100	0.36	16.2	271	∼1	∼90

Test B1 was conducted on a steeper slope compared to the others, with the slope descending to the right of the initial path, where the plume was observed. This raises the possibility that the slope influenced the direction of the plume's propagation. While a slight slope is known to affect plume spreading, C. Muñoz-Royo et al. [12] found no clear evidence linking the slope to the behavior of turbidity currents, suggesting that background currents primarily influence the spreading. Unfortunately, background current measurements were not taken for site B. C. Muñoz-Royo et al. [12] found a discharge of 12 ± 3 kg/s with all pumps active, compared to just 3 ± 2 kg/s with no active pumps, which is understandable but a significant difference that may further explain why the plume is only measured after the crossing. A smaller plume can be more easily entirely shifted to one side of the trail by background currents, although the extent of this shift remains remarkable.

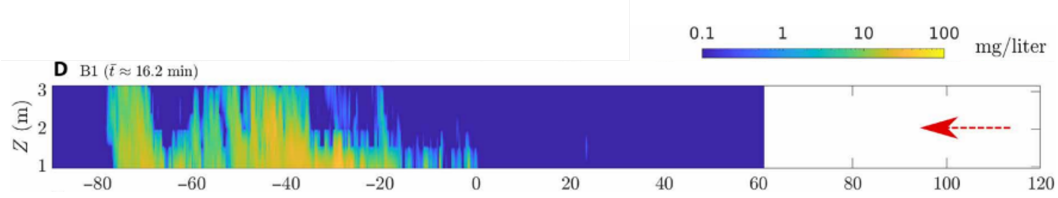


Figure 3.10: Sediment plume concentration vertical profile of B1 measured during selfie experiment, with zero at the crossing [12]

The plume discharge of test B1 is smaller than the calculated soil disturbance discussed earlier. This is because the two very different methods were used for the calculations. In paragraph 3.3.1 and 3.3.2, the calculations are very conservative and based on the kinematics of the tracks. C. Muñoz-Royo et al. [12] did not measure the total discharge but used the distance between the turbidity fronts and the Box Model Approximation. The Box Model is a simplified approach used to determine the bulk properties of a flow and its travel distance. It assumes that the entire plume has a uniform height and concentration. The distance travelled is also based on the settling velocities calculated for different particle sizes. By reversing this method and knowing the plume's traveled distance over time, along with the particle size distribution, the (uniform) concentration can be determined. This approximation provides a more global view and is likely closer to the actual situation. However, when converting the calculated discharge of test B1 for the SNC, the kinematic approximation is not that far off. For the Patania II calculations, a height and width of 4 metres is used [12]. The height and width of the SNC are about 4 and 6 metres, so the wake is approximately 1.5 times larger. Patania II was moving at a velocity of 0.36 m/s, resulting in a discharge of 8.33 ± 5.56 kg/m. By dividing the wake of the SNC by the wake of Patania II and multiplying that by the discharge of Patania II, the SNC discharge is calculated to be 12.5 ± 8.22 kg/m, which is approximately 4 to 20 times smaller than the kinematic estimation, with a mean of factor 7. The actual discharge may fall within this range.

4

Experiments

In the previous chapter, a model was developed to analyse soil relocation caused by various sediment disturbance sources. This model, based solely on the kinematics of the tracks, provides valuable insight into how each source contributes to soil relocation. However, the ultimate goal is to understand the track-induced plume generation and assess its extent. To this end, a series of experiments has been designed and conducted to validate the findings from the literature review and kinematic model and to address the remaining research objectives.

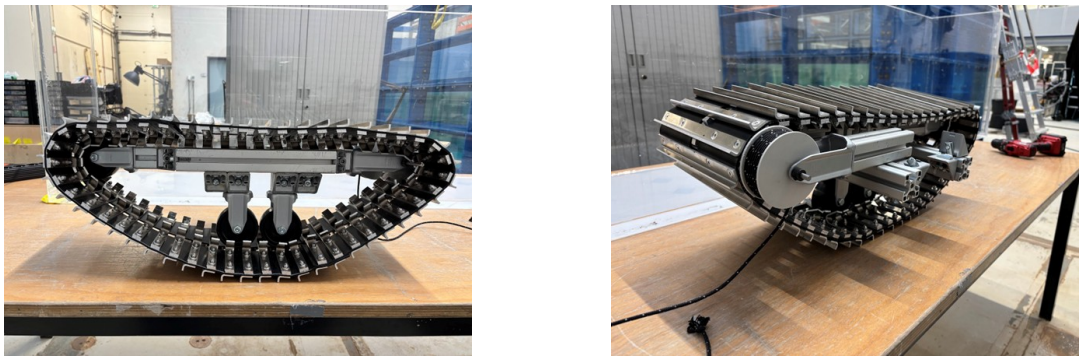


Figure 4.1: Tracks used for the experiments

This chapter first outlines the experimental setup and describes its most critical components in more detail. This is followed by the methodology and an overview of the test matrix, in which the test parameters are discussed. The chapter concludes by presenting the experimental results and the relations found.

4.1. Experimental Setup & Materials

In the below described experiments, a scaled version of the SNC tracks drives over a sediment bed in a submerged environment. The experimental setup is designed to approximate near-bottom ocean conditions in the NORI-D area. Figure 4.2 shows a schematic overview of the setup. Tests are conducted inside a plexiglass tank with internal dimensions of 2.00 m in length, 0.60 m in height, and 0.35 m in width. The tank width is kept as small as feasible to minimise three-dimensional effects. To replicate the seabed, a sediment bed is prepared separately in a designated box, which is then placed inside the tank. This modular approach streamlines preparation and enables continuous testing by alternating between two sediment boxes. Each box measures 1.30 m in length, 0.07 m in height, and 0.30 m in width. The dimensions are selected to maintain a narrow configuration while providing adequate space for lateral sediment displacement caused by track penetration. The sediment box is fixed in both

longitudinal and lateral directions using profiles positioned between the tank walls and the box.

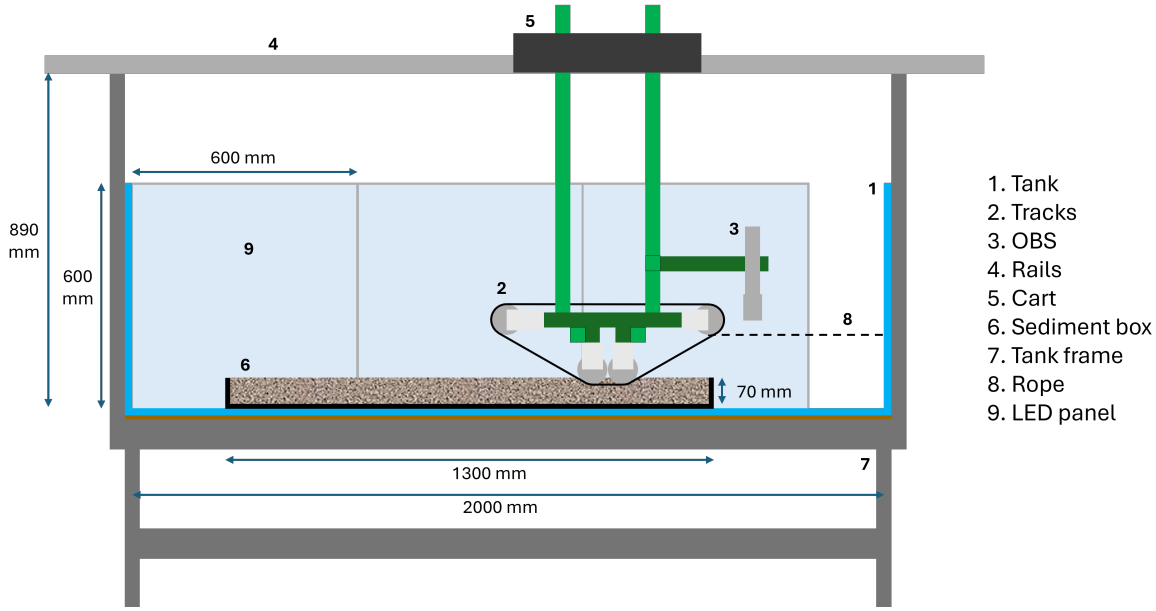


Figure 4.2: Laboratory setup design

The tracks move over the sediment bed from right to left, generating a plume whose concentration is measured using an Optical Backscatter Point Sensor (OBS) mounted at the rear of the tracks. Two GoPro cameras record the plume and track motion from the side and top outside the tank. Three 600 × 600 mm LED panels mounted at the back of the tank provide illumination to ensure clear visibility of the plume. A 3D camera will measure the height profiles of the track print in the sediment bed after each test. The tank is filled with fresh tap water, which is drained and replaced after each test run.
The following sections will provide a more detailed explanation of the design and highlight the key components of the experimental setup.

4.1.1. Tracks

The laboratory tracks are derived from the SNC track design, with similar track mechanics and all critical components scaled at a 1:10 ratio to replicate the plume dynamics and track–seabed interaction. The design is illustrated in Figures 4.3 and 4.1. The track system consists of two rubber belts connected by grousers. Like the SNC, the belt features an opening in the middle, allowing the sprocket to drive the belt via the grousers. The track belt has a width of 200 mm and a rubber thickness of 3 mm. The total track length is 616 mm and the height is 214 mm. The laboratory model uses two track rollers to reduce overall length and increase travel distance within the tank. The track rollers are built to scale and have a diameter of 80 mm. The soil entry and exit angles are maintained at 30°, consistent with the SNC design. The effective sprocket diameter is 74.8 mm.

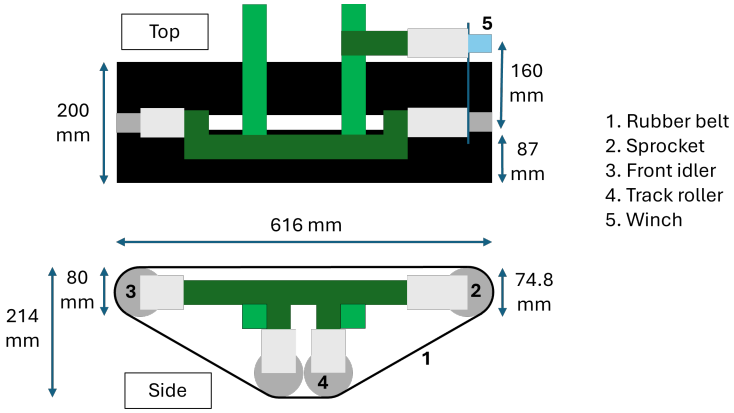


Figure 4.3: Laboratory track design with a scale of approximately 1:10

The grousers are based on a simplified design that preserves the essential characteristics of their real-world counterparts. Only the larger grousers from the SNC design are replicated in the laboratory setup. The spacing between the grousers is 30 mm, matching the scaled distance of the larger SNC grousers. Each grouser is made from a 3 mm thick aluminium plate and has a length of 12.5 mm. Figure 4.4 provides a more detailed view of the grousers.



Figure 4.4: Laboratory grouser design with a scale of approximately 1:10, with the left figure showing the front view and the right figure the side view

To avoid using underwater electronics for propulsion and prevent any complications that may arise from their underwater use, a rail system with a cart is mounted on top of the tank to propel the tracks. The cart is responsible for the linear displacement of the tracks only, while the rotation is controlled separately. A winch is attached to the same axis as the sprocket, with a low-stretch rope wound around it and secured to the left wall of the tank. As the tracks move forward, the rope unwinds from the winch, causing the sprocket and, consequently, the tracks to rotate. By adjusting the diameter of the winch, a slip ratio can be introduced. For example, when the winch has the same diameter as the sprocket (74.8 mm), there is no slip, whereas a winch diameter of 68.0 mm results in a 10% slip ratio. The power supplied to the cart is controlled via a control board, which features a dial that increases power when turned clockwise. The propulsion system does not include predefined velocity settings. A relationship between the setting and velocity is established by conducting multiple test runs at different power settings, enabling experiments at the target speeds. The motor will stutter if the power setting is too low, limiting the minimum achievable velocity to between 7 and 8 cm/s.

4.1.2. Sediment

The literature study has shown that deep-sea clay behaves differently depending on the environment. Therefore, a clay mixture is developed to mimic deep-sea clay by matching geotechnical properties of the deep-sea clay under near-bottom ocean conditions with those of the artificial clay under laboratory

conditions. A mixture of Sibelco FT-S1, Cebo OCMA Bentonite and water is used. The mineral composition of both ingredients for the artificial clay is provided in Table 4.1. This recipe is based on clay mixtures developed by Deltares for previous research to mimic the deep-sea clay [38]. The resulting clay has a grey colour.

Table 4.1: The ingredients and their proportions (percentage) for the Sibelco FT-S1 and the Cebo OCMA Bentonite [38] [39] [40]

Ingredient	FT-S1	OCMA Bentonite
Kaolinite (%)	64	17
Illite (%)	10	17
Montmorillonite (%)	-	66
Quartz (%)	19	-
Other minerals (%)	7	-

The properties focused on matching the deep-sea clay are water content and undrained shear strength. The target water content ranges from 200% to 364% and the undrained shear strength is set between 1 kPa and 4 kPa. Table 4.2 presents the final recipe to achieve these target properties. The undrained shear strength of the clay is measured using a Torvane test (Figure 4.5). Due to the very soft nature of the target clay, the largest bottom plate of the Torvane is used. A reading of 1 on the Torvane scale corresponds to an undrained shear strength of 19.6 kPa. The soft clay tested in this study consistently falls within the lowest range of the Torvane scale (< 0.5). For this research, a Torvane value of < 0.25 is accepted, corresponding to an undrained shear strength of < 4.9 kPa.Undrained shear strength measurements taken across multiple batches confirmed that all batches remained within this range. Based on this consistency, subsequent batches prepared with the same recipe are assumed to meet the required specifications. The OCMA and FT-S1 clay powders are not completely dry, with the OCMA powder containing a water content of 9.9% and the FT-S1 powder 6.4% [38]. Using the ratios from Table 4.2, the actual water content of the artificial clay has been calculated, resulting in a total water content of 244%.

Table 4.2: Proportions for the test sediment mixture with the ratio masses based on samples from the study performed by Deltares [38]

Ingredient	Ratio	1 batch	1 m^3	Unit
Cebo OCMA	0.14	9.00	266.0	kg
Sibelco FT-S1	0.07	4.50	133.0	kg
Water	0.45	28.9	854.9	kg
Total mass	0.61	42.4	1254	kg
Unit weight	12.3	12.3	12.3	kN/m^3
Total volume	$5.26{\cdot}10^{-4}$	0.0338	1	kN/m^3

To assess the effect of recovery time on the properties of the artificial clay, four samples are prepared in small containers, each allowed to recover for a different duration ranging from 0 to 3 days. Undrained shear strength measurements using the Torvane show that all samples remain within the same range. However, when examined by hand, the clay is perceived to become stiffer over time, suggesting structural changes. Notably, no layer of water is observed on the surface of the clay samples.



Figure 4.5: Torvane test to determine the undrained shear strength of the clay

Before conducting experiments with the artificial clay, preliminary tests are carried out using Millisil M10 to commission the setup and verify the proper functioning of the mechanisms and devices. These tests are excluded from the test matrix (Section 4.3). Millisil is a finely crushed quartz with very fine grains (d_{50} = 23 μm). Table 4.3 presents its granulometric data and characteristics. Millisil has no cohesion and settles much faster than clay, making it easier to handle. This makes it a suitable sediment for testing the experimental setup while also allowing for initial observations of plume behaviour. Only enough Millisil is available to prepare a single sediment bed, so it must be recycled after each test. To optimise the settling process, the smaller particles are filtered out before the experiments. The objective is to ensure that the Millisil settles within an hour inside the tank, allowing for a higher testing frequency within the available timeframe.

Table 4.3: Soil properties for Millisil M10 [41]

Property	Value	Unit
d_{10}	4	μm
d_{50}	23	μm
d_{90}	60	μm
Density	2.65	kg/m^3
Bulk density	0.9	kg/m^3

The filtering process is carried out in a round bucket. The bucket is filled with Millisil to a layer thickness of approximately 5 cm and then with water until the water level reaches approximately 30 cm. The Millisil is then suspended by mixing the volume with a concrete mixer until a uniform mixture is achieved (Figure 4.6a). The mixture is left to rest for an hour, allowing the particles to settle. Any remaining suspended particles are removed by siphoning the cloudy water into another bucket (Figure 4.6c). This is called a washing. The process is repeated until the water remains clear after the desired settling time. Figure 4.7 illustrates the progress of the filtering process.
After approximately 20 washing cycles, the settling time is reduced to half an hour, as the water depth in the tank is twice that of the bucket. The filtering process is discontinued as soon as no further improvement is observed after a half-hour settling time. In total, 34 washing cycles are performed, with the final result illustrated in Figure 4.7c.
Once filtered, the Millisil is placed inside a sediment box and evenly distributed across the bottom, resulting in a sediment layer thickness of approximately 4 cm (Figure 4.8a).



(a) (b) (c)

Figure 4.6: Millisil filter setup, with (a) the bucket after mixing the Millisil with water, (b) the concrete mixer used to mix the Millisil with water and (c) how the dirty water with the smaller particles is siphoned to another bucket



(a) (b) (c)

Figure 4.7: Millisil filtering progress, with (a) the 1^{st} washing with a 1 hour interval, (b) the 6^{th} washing with a 1 hour interval and (c) the 34^{th} washing with a half hour interval



(a) (b) (c)

Figure 4.8: Prepared sediment boxes, with (a) Millisil with a small layer of water on top, (b) artificial clay and (c) deep-sea clay from GSR box core 33

Also, a test will be conducted using actual deep-sea clay. The sediment used in this test is the remaining material from box core 33 of the GSR area and is brown in colour. It originates from a deeper layer than the surface layer where the nodules are typically found. While it is not the same as NORI-D sediment, it shares many similar characteristics. Due to the limited amount of available clay, only one test run can be performed. Since there is not enough sediment to completely fill the sediment box, a small wooden beam is placed inside to reduce the box's volume, as illustrated in Figure 4.8c.

Table 4.4: Summary of the mineral compositions for the artificial clay and the average of the GSR box cores shared in the EIS of GSR [38] [8]

Mineral	Artificial clay	Deep-sea clay (GSR)
Kaolinite (%)	32.6	4.9
Illite (%)	14.6	48.3
Montmorillonite / Smectite (%)	44	36.4
Chlorite (%)	0	10.3
Quartz (%)	6.3	0
Other (%)	2.3	0

The GSR clay has a significantly different mineral composition than the artificial clay, as shown in Table 4.4. The bulk density assumed for the GSR sediment is 1350 kg/m^3 and the water content 200%, as these are the average values found for the sediment [8]. The undrained shear strength of the GSR clay is also measured using a Torvane and falls within the same range as the artificial clay (< 4.9 kPa).

4.1.3. Optical Backscatter Point Sensor

An Optical Backscatter Point Sensor (OBS) is used to measure the concentration of sediment plumes behind the tracks. The OBS emits a light beam that reflects off particles suspended in the fluid. The intensity of this backscattered light is then measured, providing a turbidity value. A higher concentration of particles results in greater light reflection, leading to a higher turbidity reading. In the experiments, the tip of the OBS is positioned approximately 10 cm behind the tracks and 20 cm above the sediment bed. The OBS does not measure the concentration of the entire plume but rather provides local measurements. The measurement area depends on the light transmittance through the plume, which varies with its concentration. For high-concentration plumes, the OBS can measure an area as small as a few millimeters, while for low-concentration plumes, it can measure an area of up to ten centimeters. The sensor must be calibrated for each sediment type to relate the measured turbidity to the actual sediment concentration. This calibration depends on factors such as sediment composition and particle size. The calibration method follows the approach used by Chmiel et al. for an Acoustic Doppler Velocimeter [42]. By measuring turbidity at known concentrations, a calibration curve is established, allowing for accurate concentration measurements during the experiments. Calibration is performed for both the Millisil and the artificial clay. The calibration curve for the deep-sea sediment is provided by the Royal Netherlands Institute for Sea Research (NIOZ) [43].



Figure 4.9: OBS calibration setup

For the calibration of the artificial clay, a bucket is filled with 12 litres of tap water. The OBS is placed inside the bucket with sufficient clearance from the sides and bottom to prevent measurement interference from backscatter. An automatic mixer ensures that the mixture remains uniformly distributed throughout the calibration process. The setup is illustrated in Figure 4.9.
The calibration begins at a concentration of 0 g/L, which is gradually increased in predefined intervals. After each addition of clay, the mixture is stirred for five minutes to ensure even distribution before data collection begins. OBS measurements are recorded for one minute, but to account for potential fluctuations at the start and end of the sampling period, only the middle 40 seconds of data (recorded at 1 Hz) are averaged for each concentration. Concentrations range from 0 g/L to 10 g/L, with increments of 0.1 g/L between 0 g/L and 1 g/L, and increments of 1 g/L for concentrations from 1 g/L to 10 g/L. It is observed that the sensor becomes saturated at concentrations above 3 g/L. Figure 4.10b presents the calibration curve for the artificial clay. From that curve, the following equation is obtained to calculate the sediment concentration from the measured turbidity:

$$C = \frac{(T - 12.969)}{489.46} \tag{4.1}$$

Where C represents the concentration in [g/L] and T is the turbidity in [FTU].

Table 4.5: Batch sizes for the Millisil OBS calibration

Concentration (g/L)	5	4	3	2	1	0.9	0.8	0.7	0.6	0.5	0.4	0.3	0.2	0.1	0
Wet Millisil (g)	75.1	30.0	30.0	30.0	10.5	10.5	10.5	10.5	4.5	4.5	4.5	4.5	1.5	1.5	0
Volume tank (L)	12	6	8	12	8.4	9.3	10.5	12	6	7.2	9	12	6	12	12

A similar calibration method is applied for Millisil, with a slight modification. Since Millisil remains wet from the filtering process, an alternative approach is used. A sample of Millisil is mixed with an excess amount of water, allowing the sediment to settle. The clear water from the top is then drained, leaving the sediment fully saturated. It is assumed that when the quartz is fully saturated, its volume concentration is 60%. Based on this assumption, fully saturated Millisil is used to prepare batches for the target concentrations. To minimise errors associated with this method, a different batching approach is employed compared to the artificial clay. Instead of gradually increasing the concentration by adding small sediment batches, the process begins with a high concentration and adding water to dilute the mixture.

Due to the clearance requirements of the OBS, the bucket must contain at least 6 litres of water. Therefore, a grouping system is established to determine which concentrations can be achieved using the largest possible Millisil batches while maintaining the minimum required volume. These concentration groupings are presented in Table 4.5. The Millisil calibration curve is shown in Figure 4.10a. From that curve, the following equation is obtained to calculate the sediment concentration from the measured turbidity:

$$C = \frac{(T - 12.969)}{79.948} \tag{4.2}$$

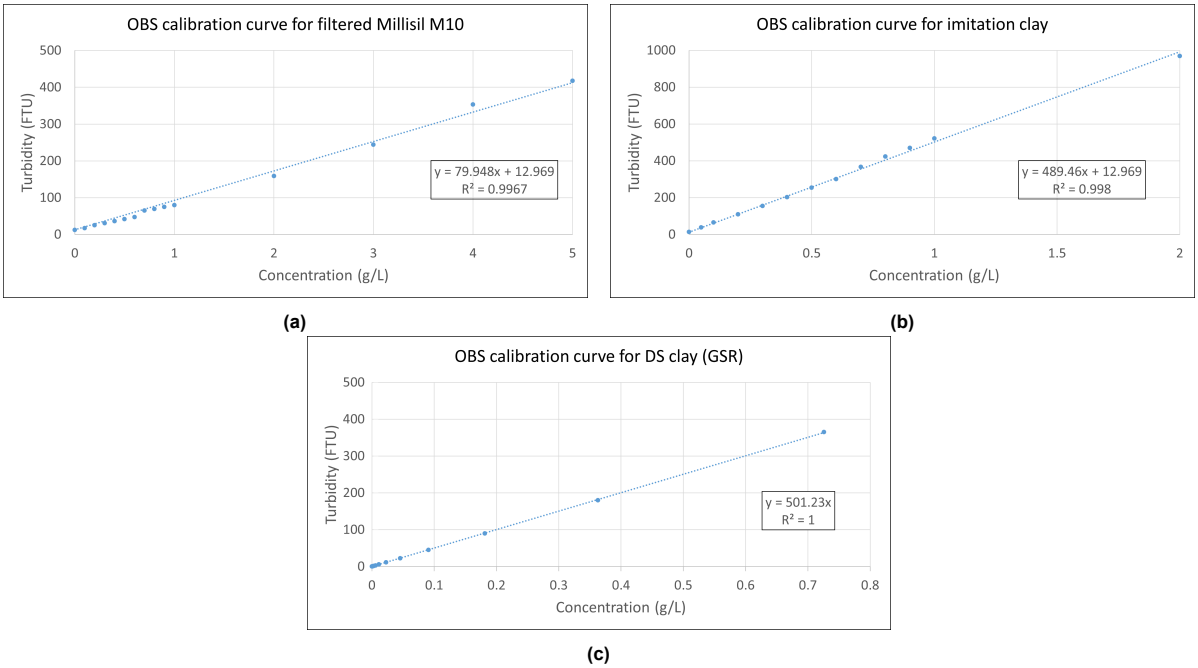


Figure 4.10: OBS calibration curves, with (a) the Millisil calibration curve with the corrected measurements, (b) the artificial clay calibration curve and (c) the deep-sea clay calibration curve from NIOZ [43]

4.1.4. 3D Camera

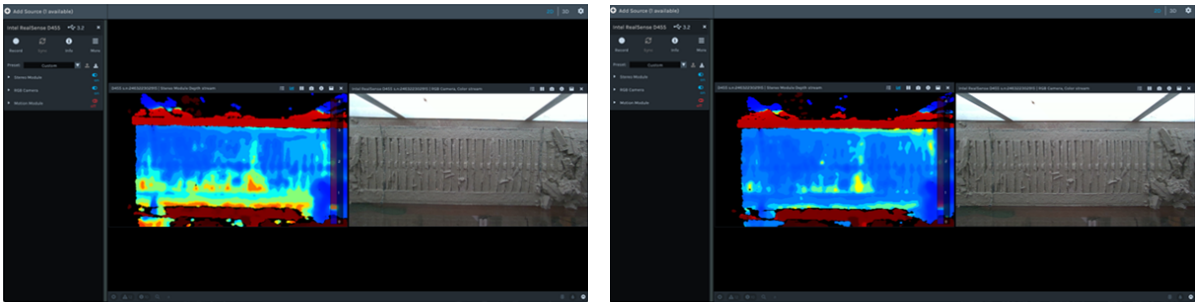
A 3D camera is employed to map the bottom profile of the sediment bed after the tracks have driven over it. These profile scans might help to validate the results obtained from the OBS and GoPro footage. The Intel RealSense D455 model is used for the 3D scans. The camera operates using a stereo vision system, featuring two lenses, which enable it to perceive depth similar to the human eyes. Depth is calculated by an AI that compares the two images. Before scanning the bottom profile, the tank is drained. Once the tank is completely drained, two markers are placed on the bed to indicate the area where the scans should be conducted (see Figure 4.11a). These markers align with the edges of the middle LED panel. The 3D camera is positioned directly above the tank at the marked location (see Figure 4.11b).



(a) (b)

Figure 4.11: 3D camera setup, with (a) the area markings (L = 0.6 m) and (b) the camera positioning

Before scanning, it is ensured that the camera is levelled. Even a slight angle can significantly affect the measured profile, as differences within a single scan often fall within a few millimeters. Intel software is used to check the camera's alignment. By reviewing the depth footage and adjusting the height, the camera is calibrated to be level for each test, as shown in Figure 4.12.



(a) (b)

Figure 4.12: 3D camera depth display, with (a) the depth image when the camera position is uneven and (b) where the position is corrected

The camera is then accessed via Python. First, two calibration points are established to set the distance (the width of a LED panel) and H = 0, with the height adjusted to the level of the sediment box's side wall. After this, additional points are set, and the Python code generates a bottom profile plot from the first point to the second. For every test run, five lines are measured (see Figure 4.13).

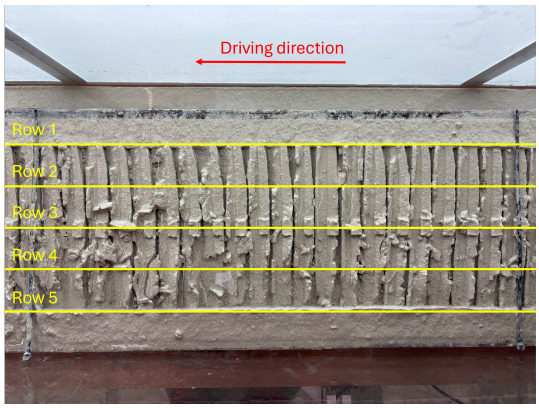


Figure 4.13: The lines used for the height profiles of the sediment beds

4.2. Methodology

Ensuring that the sediment beds are in the same condition for each experiment is crucial to avoid irregularities in the results. The following describes the methodology for a day of testing:

- At the start of the day, the clay batch is already mixed and two sediment beds are prepared in advance from the day before.
- On the test day, the LED panels are switched on, then the GoPro cameras are connected to the laptop and subsequently the OBS is set up. The OBS, which runs on batteries, remains installed behind the tracks for the entire day.
- Before installation, the OBS is configured on the laptop, then synchronised with the laptop's clock and programmed with a start time. Once activated, it is placed inside its waterproof case and attached behind the tracks.
- With the electronics set up, the first sediment box is placed inside the tank and secured in position.
- The rope for track rotation is wound onto the winch and the tracks are positioned on the sediment bed.
- Depending on the test parameter settings, the tracks are pushed into the clay until the desired penetration depth is reached. This depth is determined by the length of the beams extending above the cart. For zero penetration, the marked length is 28.2 cm (see Figure 4.14).
- Once the penetration is set, the rope is anchored to the tank wall, and the velocity settings are adjusted.

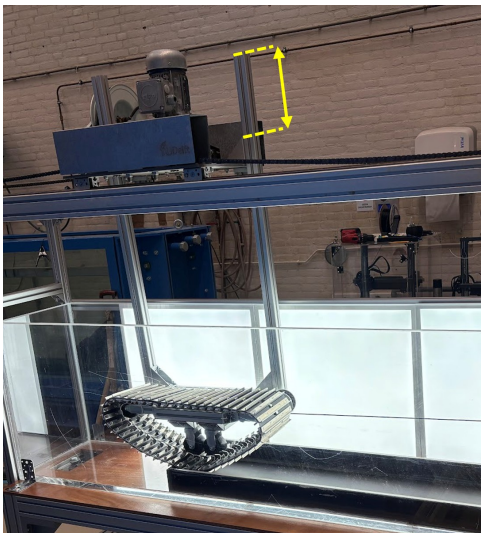


Figure 4.14: Penetration depth reference, with 0 mm penetration when the yellow marked length is 28.2 cm

- Now, the tank is filled with water. The hose is placed beneath the sediment box to minimise disturbance to the sediment bed. The tank is filled until approximately 5 cm of clearance remains at the top.
- Before proceeding, the recording software is checked to ensure that both cameras are working and the clock is visible in the frame. The experiment name code is updated and a final check is performed to confirm the penetration, velocity and slip settings, as well as the fastening of the sediment box.
- With everything ready, the recording begins. A ruler is placed inside the tank for approximately 10 seconds to provide a scale reference for the camera and is then removed.
- The cart is then activated and automatically stops when the tracks reach the end of the sediment bed (1 meter). The recording continues for approximately 15 seconds after the run to capture the development of the plume.

- The tracks are then lifted free from the bed and the tank is drained. The tracks are returned to their starting position by driving the cart back at low speed to avoid disturbing the sediment bed.
- Once the tank is fully drained, the bottom profiles of the sediment bed are recorded using the 3D camera, as described in Section 4.1.4. A standard photograph is also taken to document the sediment bed.
- After collecting the bottom profile data, the sediment box is removed and both the tank and tracks are thoroughly cleaned.
- Once all sediment is removed, the process can be repeated for the next test. To adjust the slip ratio, the winch must be replaced. Varying the winch's diameter allows for changes in the slip ratio.
- Draining and refilling the tank takes time, so a sediment bed for a later test is prepared during this waiting period. The top layer of clay is removed and discarded (Figure 4.15b), while the remaining clay is scooped (Figure 4.15c), mixed and then combined with fresh clay from the same batch prepared the previous day (Figure 4.15d). The final layer of clay is added, spread evenly in the box and smoothed (Figure 4.15e). To prevent drying, the box is covered with a plastic sheet. This process is illustrated in Figure 4.15.



(a) (b) (c) (d) (e)

Figure 4.15: Sediment bed preparation of a used sediment bed, where (a) the top layer is being removed, (b) the whole top layer is removed, (c) the clay left is scooped, (d) the newly added clay is mixed with the left clay and spread evenly and (e) the box is topped with extra clay and smoothend

- In the afternoon, the clay for the next day is prepared. First, the correct amounts of FT-S1 (4.5 kg) and OCMA (9 kg) clay powder are weighed, and 28.93 L of water is measured.
- Using a concrete mixer attached to a cordless drill, the FT-S1 clay is first added to the water in the bucket and mixed until uniform (Figure 4.16c). At this stage, the mixture thickens but remains liquid.
- Then, half of the OCMA powder is added and mixed thoroughly. The clay is still fluid but has already thickened (Figure 4.16d).
- Finally, the remaining OCMA powder is incorporated. The clay now takes on a plastic consistency. The clay must be mixed until all lumps are eliminated (Figure 4.16e).
- Once mixed, the clay is covered with plastic to prevent drying. Figure 4.16 shows the clay mixing process.



(a) (b) (c) (d) (e)

Figure 4.16: The various steps taken in the mixing process of the artificial clay, with (a) an illustration of the setup, (b) the bucket filled with water only, (c) the mixture when the FT-S1 is added and mixed, (d) the mixture when also half of the OCMA is added and (e) when the second half of the OCMA is added and uniformly mixed

Up to four experiments can be conducted on a well-organised test day. At the end of the day, the entire setup is cleaned and the first two sediment boxes for the next day are prepared. Once everything is tidy, the OBS is removed from the tracks and connected to the laptop. The data from the day's experiments is gathered and by synchronising the clock in the video footage with the OBS timestamps, the correct data points are identified.

4.3. Test Matrix and Parameters

To assess the influence of sediment suspension sources identified in the literature, these experiments focus on four key parameters: sediment bed penetration, velocity, slip ratio and sediment type. The standard settings for these parameters during the experiments are a penetration depth of 6 mm, a velocity corresponding to setting 5 (7–9 cm/s), a slip ratio of 10% and the artificial clay as the sediment. When testing a parameter, all other variables remain constant to isolate its specific influence. Table 4.6 provides an overview of all tests. As can be read from Table 4.6, several important notes apply to some of the tests. These notes are better explained below:

- Tests #11–#13: The 3D camera is not fully functional during these tests, which prevents the accurate calculation of the area below the bottom profiles.
- Tests #19–#22: The OBS data for these tests is lost due to an error during the sensor data retrieval process, but footage of the experiments remains available. Since OBS data is crucial, these tests are repeated. However, the footage can still help validate the new test results.

Table 4.6: Test matrix with the useful experiments only

Type	#	Code	Parameters				Time driving (s)	Notes
			Penetration (mm)	Velocity setting	Real velocity (cm/s)	Slip ratio (%)		
Control	11	02_Clay_P6_V5_S10	6	5	7.1	10	14	Area of the bottom profile not measured
	13	04_Clay_P6_V5_S10	6	5	7.7	10	13	Area of the bottom profile not measured
Penetration	14	05_Clay_P0_V5_S10	0	5	7.7	10	13	
	15	06_Clay_P10_V5_S10	10	5	8.3	10	12	Tracks placed submerged
	16	07_Clay_P2_V5_S10	2	5	8.3	10	12	
	17	08_Clay_P4_V5_S10	4	5	7.7	10	13	
	18	09_Clay_P8_V5_S10	8	5	7.7	10	13	
Velocity	19	10_Clay_P6_V10_S10	6	10	14.3	10	7	Tracks placed submerged, OBS data lost
	20	11_Clay_P6_V8_S10	6	8	11.1	10	9	OBS data lost
	21	12_Clay_P6_V20_S10	6	20	20.0	10	5	OBS data lost
Control	22	13_Clay_P6_V5_S10	6	5	8.3	10	12	OBS data lost
Slip	23	14_Clay_P6_V5_S0	6	5	8.3	0	12	
	24	15_Clay_P6_V5_S20	6	5	9.1	20	11	Sediment box rested for 2.5 days
	25	16_Clay_P6_V5_S5	6	5	9.1	5	11	Sediment box rested for 2.5 days
	26	17_Clay_P6_V5_S5	6	5	9.1	5	11	
	27	18_Clay_P6_V5_S20	6	5	9.1	20	11	
Penetration	28	19_Clay_P10_V5_S10	10	10	9.1	10	11	
Velocity	29	20_Clay_P6_V10_S10	6	10	14.3	10	7	
	30	21_Clay_P6_V8_S10	6	8	11.1	10	9	
	31	22_Clay_P6_V20_S10	6	20	20.0	10	5	
Control	32	23_Clay_P6_V5_S10	6	5	9.1	10	11	
DS sediment	33	01_DSClay_P6_V5_S10	6	5	9.1	10	11	

Sediment bed track penetration

Following the control tests, the penetration tests are performed by varying the penetration depth. In the kinematic model, penetration accounts for the most significant sediment relocation. Therefore, adjusting this parameter is hypothesised to have one of the most significant impacts. The standard penetration setting is 6 mm, corresponding to a 1:10 scale of the average real-world penetration [13]. This value is then varied between 0 mm and 10 mm. A representation of the penetration depths relative to the rubber belt of the tracks is shown in Figure 4.17.

Since the clay is very soft, a considerable amount of sediment is hypothesised to be suspended due to the momentum generated as it is pushed to the sides and front of the tracks. However, not all sediment will be suspended, as some will relocate along the sides of the trench formed by the tracks. These tests aim to provide insight into the sediment suspension-to-relocation ratio.

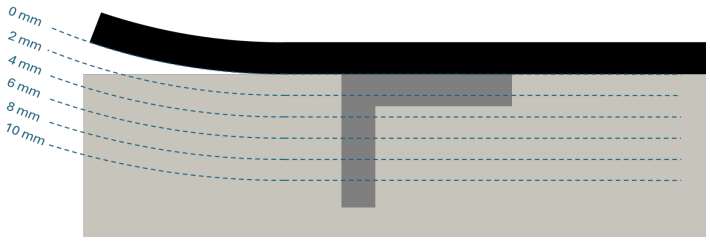


Figure 4.17: Representation of the seabed penetration depth relative to the tracks, where p = 0 mm when the rubber belt is on the seabed

Velocity
The experiments are conducted at lower velocities than those performed in the field (0.40 cm/s). By testing at different velocities, the velocity effect can be evaluated and results can be extrapolated to real-world conditions. The setup's minimum velocity is approximately 7 cm/s and the maximum test velocity is 20 cm/s. An increase in velocity is hypothesised to influence sediment suspension in two ways:

- **Momentum Increase:** The seabed penetration by the tracks leads to sediment displacement with a certain momentum, resulting in plume generation. Driving with a higher velocity amplifies the momentum of sediment displacement, leading to greater plume concentrations.
- **Track Rotation Effect:** Faster track rotation intensifies the scooping and pull-out actions of the grousers. This increased movement will likely sweep more clay into the water rather than slowly relocate it, further contributing to plume concentration. This affects the sediment suspension-to-relocation ratio for the scooping and pull-out mechanisms.

Slip Ratio
A slip was observed during the PMT of the SNC, which affects clay strength. As clay is remoulded, its undrained shear strength decreases. A higher slip ratio increases clay remoulding and consequently influences the sediment suspension. However, the undrained shear strength is already low for this clay and the total sediment displacement due to slip is limited in the laboratory setting. Therefore, the remoulding effect is expected to be minimal.
Increasing the slip ratio also increases the track rotation speed. As discussed earlier, the rotation velocity influences sediment suspension.
The standard slip ratio for the experiments is set to 10%, but also slip ratios of 0%, 5% and 20% will be tested. Changing the slip ratio allows for closer examination of the effects of scooping and grouser pull-out while keeping the penetration effects constant, providing a better understanding of their impact.

Sediment type
The artificial clay is used to replicate geotechnical properties of deep-sea clay under laboratory conditions, compensating for differences in pressure and water conditions. While it matches deep-sea clay's water content and undrained shear strength, it differs in mineral composition and other potentially significant properties. A test using actual deep-sea sediment is conducted to enhance the ability to translate artificial clay results into real-world conditions. This test may provide valuable insights and serve as a comparison point for the real world. Additionally, it is interesting to observe how deep-sea sediment behaves under laboratory conditions. In the real-world scenario, the sediment remains undisturbed prior to mining activities, resulting in peak undrained shear strengths. Whereas, the clay used in the experiments is always remoulded, leading to reduced strength characteristics and possibly increasing plume generation.

4.4. Results

In this section, the results of the experiments outlined in the preceding sections are presented. In Section 4.4.1, the data processing methodology will be elaborated upon, explaining how and why the data is processed in a particular manner, thereby ensuring that the results are as accurate and meaningful as possible. Following this, the processed results will be presented in the subsequent sections 4.4.2 up to 4.4.6 and the relations will be identified. In addition to the primary focus areas, several additional

observations have been made throughout the experiments. Although not directly part of the initial research scope, these findings provide valuable insights and will be explored throughout this chapter. To keep the Results section comprehensible, the results from the Millisil experiments are discussed in Appendix E, as their main objective is to improve the setup. In general, all experiments have been conducted with artificial clay unless otherwise mentioned (e.g. the results described in Section 4.4.5 have been executed with deep-sea clay). Furthermore, the temperature measured in the tank during the tests ranges from 8.2 °C to 13.6 °C.

4.4.1. Data Processing

This section describes the results of the data processing with the aim to ensure that the data is presented as meaningful as possible. The velocity series is used as an example for the data processing in this section. The results analysed in the next sections have undergone the same data processing steps. The raw data of all experiments is provided in Appendix B.

Since the tracks' actual velocity varied between tests and did not always match the target velocity, the real velocity has been calculated from the video recordings after each test run. The Optical Backscatter Point Sensor (OBS) was set to record at a frequency of 1 Hz. The tracks move at different velocities across tests, so data points recorded at the same driving time correspond to different positions on the sediment bed. To account for this, the concentration measured by the OBS was plotted against the distance travelled. This is illustrated in Figure 4.18a. The distance on the x-axis represents the location of the front track roller on the sediment bed. The concentration on the y-axis corresponds to the value measured by the OBS at that track location. Since the OBS in the hereby used line-up is mounted behind the tracks, it effectively measures the plume approximately 47 cm behind the x-axis location.

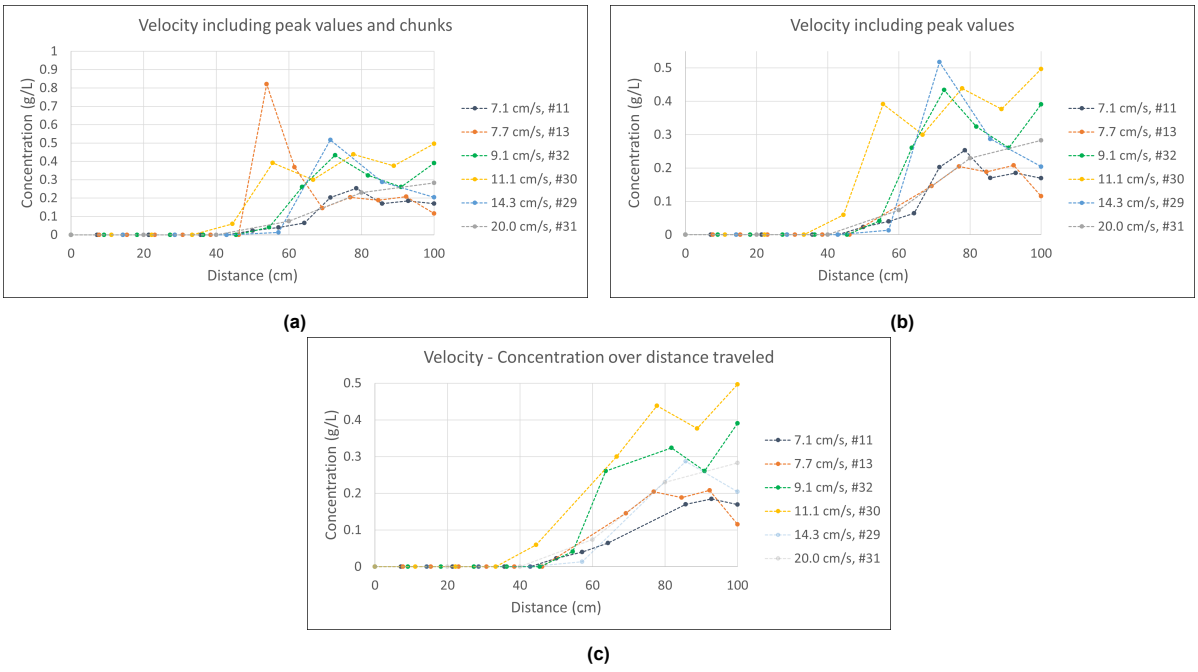


Figure 4.18: The steps taken for the data processing of the velocity series, with (a) the raw data, (b) after removal of data points where a chunk of clay was in front of the sensor and (c) the processed data after removal of the plume encounter peak values

In some instances, large chunks of clay fell in front of the OBS, causing extremely high concentration readings. These outlier points are removed from the dataset to avoid distorting the overall results. The cleaned graph is shown in Figure 4.18b.

The plume requires time to develop and since the OBS is mounted at the rear of the tracks, a certain distance must be covered before it can measure a steady-state plume concentration. Interestingly, it is consistently observed that when the OBS reaches the steady-state plume, it first records a peak concentration, which then decreases as the tracks continue to travel. This trend is clearly visible in Figure 4.18b and is particularly notable because it occurs in nearly every experiment.

To investigate this phenomenon further, the experiment recordings are closely analysed. When the tracks start moving, a chunk of clay is pulled from the bed and trapped between the grousers, as highlighted by the yellow circle in Figure 4.19. At this stage, no scooping occurs. However, once the tracks stop picking up sediment and begin scooping, a dense plume is generated, marking the point at which the full plume is generated. The observed peak concentration consistently coincides with the moment the OBS encounters this dense plume, right where the tracks started scooping.

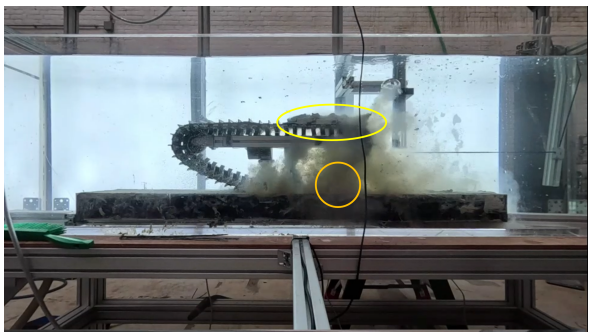


Figure 4.19: Plume generation when the tracks stop picking up the clay, with in the yellow marking the picked up clay and in the orange marking the dense plume generation by scooping

At this location, the OBS is exposed to a sudden surge in sediment concentration, which temporarily overwhelms the sensor and causes a peak reading. After this initial spike, the OBS stabilises and measures the actual plume concentration. These peak values are excluded from the data analysis to ensure a more accurate representation of sediment concentration over the distance travelled. An example is given in Figure 4.18c.

4.4.2. Seabed Penetration

The seabed penetration tests have been conducted at 6 depths ranging from 0 mm to 10 mm. The OBS results from the whole penetration series are shown in Figure 4.20, displaying the measured sediment concentration over the length of the sediment bed for all penetration depths. Plots marked with * represent tests from other parameter series that can be used for this category as well. Lower penetration depths (0 mm and 2 mm) show the higher measured concentrations, while higher penetration depths (8 mm and 10 mm) show lower concentrations. The 6 mm penetration test recorded the highest concentration of all. There does not seem to be an apparent relation in this figure.

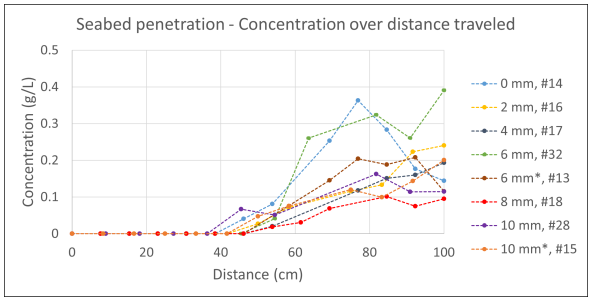


Figure 4.20: OBS results of the whole seabed penetration series with the plume encounter peaks removed (Slip ratio = 10%)

After further analysis, it is found that although the velocity setting is constant across all tests, the actual velocities vary between runs. Since velocity might influence plume concentration, the data are divided into separate plots based on the calculated velocities. This is shown in Figure 4.21, which reveals a clearer relationship. Most plots show that as penetration depth increases, the measured plume concentration decreases. In Figure 4.21a, the plume concentration for 4 mm penetration is higher than for 6 mm* penetration, deviating from the general trend observed at other penetration depths. Additionally, the plume concentration at 0 mm penetration decreases significantly after 77 cm of travel distance.

Examination of the bed profile of the 0 mm penetration test (Appendix C) indicates that the tracks pick up chunks of clay in the later stage of the test run, reducing the amount of sediment being scooped by the grousers and resulting in a lower plume concentration.

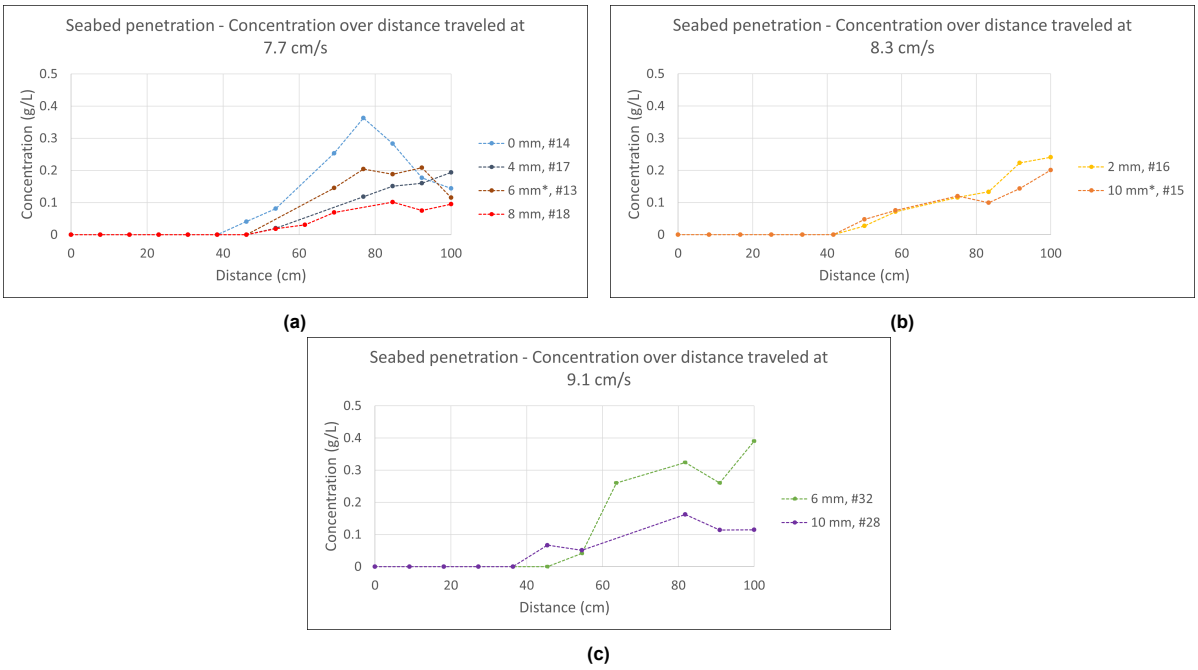


Figure 4.21: Measured concentrations by the OBS ordered by velocity (Slip ratio = 10%)

Other data that has been analysed are the height profiles made by the 3D camera. An overview of all height profiles is provided in Appendix D. By comparing these profiles with the corresponding sediment bed images in Appendix C, local anomalies such as large clay clumps or voids are identified and excluded to enable a more accurate analysis of the base height profile resulting from track penetration. Based on this analysis, a sediment relocation order is established and is presented in Table 4.7. The results show no consistent relationship between penetration depth and sediment relocation and grouping the data by velocity does not reveal a clear trend.

Table 4.7: Sediment relocation differences for all seabed penetration depths with a ranking from high to low total relocation

Penetration depth	Row 1 (mm)	Row 3 (mm)	Row 5 (mm)	Relocation ranking
0 mm	3	4.5	2.5	3
2 mm	2	3.5	2	5
4 mm	1	3.5	1.5	6
6 mm	2	6	5	1
8 mm	2	5	4	2
10 mm	3	4.5	1.5	4

4.4.3. Driving Velocity

Experiments have been conducted at six different velocities. An overview of the results is presented in Figure 4.22, which displays the sediment concentration measured by the OBS along the travelled distance of the track for each velocity. A fixed time interval determines the measurement locations, so tests conducted at higher velocities contain fewer data points.

The results show that the lowest velocities, 7.1 cm/s and 7.7 cm/s, produce the lowest sediment concentrations, with concentrations increasing at 9.1 cm/s and 11.1 cm/s. However, the results at 14.3 cm/s and 20.0 cm/s deviate from this pattern. These two velocities did not reach a steady-state plume and have therefore been made transparent (Figure 4.22) and excluded from the results interpretation.

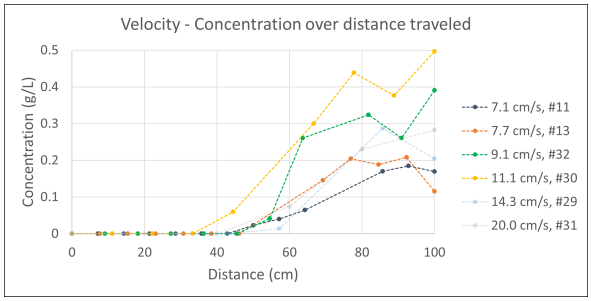


Figure 4.22: OBS results of the whole velocity series with the 14.3 cm/s and 20.0 cm/s velocities made transparant (Penetration = 6 mm, Slip ratio = 10%)

Figure 4.23 presents the peak and average concentration values for different velocities. These two metrics are used to validate each other. The average concentration is not calculated over the entire test run but only from when the OBS measures a steady-state plume until the track stops moving. A more detailed explanation of this approach can be found in Appendix B.
The data suggest a general trend in which higher velocities increase sediment concentrations. The only exception is the 7.7 cm/s test, where the average concentration is slightly lower than that of 7.1 cm/s. However, since these velocities are relatively close and the difference is minimal, this variation is considered an acceptable margin of error.

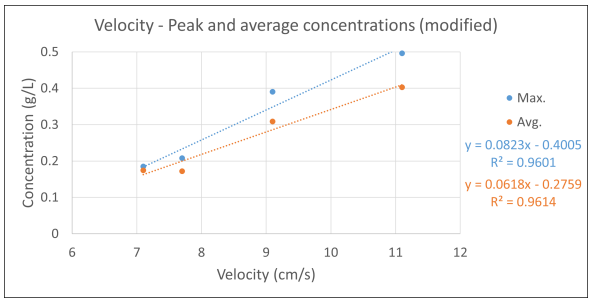


Figure 4.23: The peak and average values of the OBS results for the different velocities with a steady state plume (Penetration = 6 mm, Slip ratio = 10%)

A closer examination of the sediment beds across different velocities provides an interesting insight. A few examples are shown in Figure 4.24, while a complete overview can be found in Appendix C. At lower velocities, more clay is picked up and the sediment bed experiences greater disturbance. This is particularly interesting because the sediment bed appears less damaged while the plume concentration increases with higher velocities.



(a) (b) (c)

Figure 4.24: Sediment bed profiles after the tracks drove over it at different velocities, with (a) 7.7 cm/s, (b) 11.1 cm/s and (c) 20 cm/s

4.4.4. Slip Ratio

By introducing a slip, the sediment experiences (minimal) remoulding and the tracks rotate at a higher velocity. Figure 4.25 provides an overview of the slip series results, where the concentration measured by the OBS is plotted against the distance travelled by the tracks at different slip ratios. A clear trend of increasing concentration with higher slip ratios can be observed for 0%, 5%, and 10% slip. However, the 20% slip ratio does not follow this pattern. Closer examination of the recordings reveals that at 20% slip, the tracks pick up a relatively long chunk of clay at the start, which delays the onset of the scooping effect and, consequently, the full development of the plume. As a result, the OBS does not capture a steady-state plume before the tracks reach the end of the sediment box. Therefore, the 20% slip test is shown as transparent in the figure and excluded from the results interpretation.

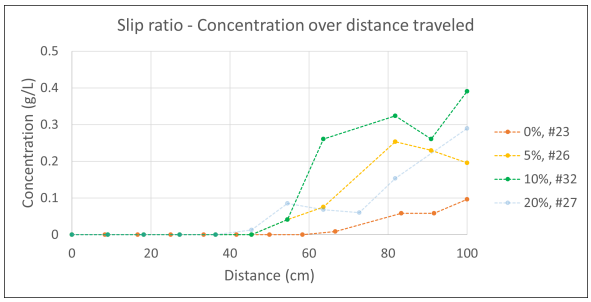


Figure 4.25: OBS results of the whole slip ratio series with the plume encounter peaks removed (Penetration = 6 mm)

Figure 4.26 presents the average and peak concentrations for the different slip ratios. The graph shows that the concentration increases with an increasing slip ratio and the data points are close to the linear trend.

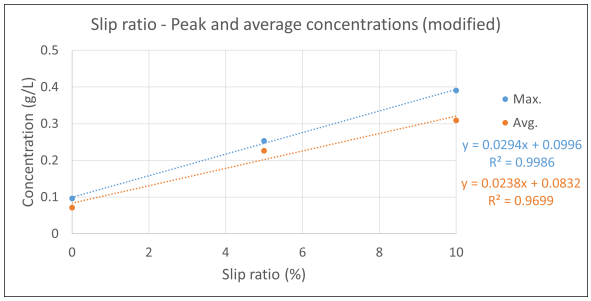
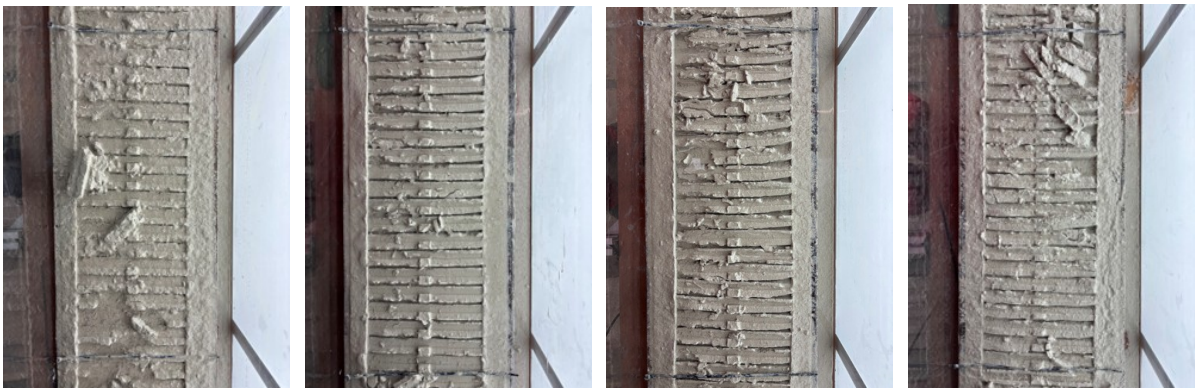


Figure 4.26: The peak and average values of the OBS results for the different slip ratios with a steady state plume (Penetration = 6 mm)

When examining the bed profiles for different slip ratios, as shown in Figure 4.27, it is observed that the sediment bed sustains more damage at higher slip ratios.



(a) (b) (c) (d)

Figure 4.27: Sediment bed profile for different slip ratios, with (a) 0%, (b) 5%, (c) 10% and (d) 20%

Two experiments from the slip series (5% and 20%) are conducted using sediment boxes that have rested over the weekend, resulting in a 2.5-day resting period instead of the usual 0.5 day (overnight). During the resting period, the boxes are covered with plastic sheets to prevent drying. Although the sediment beds appear unchanged when placed in the tank, the experiments show a significantly lower plume concentration. As a result, these slip ratios are retested using a fresh batch of clay.
Figure 4.28 compares the results for the 5% and 20% slip ratios using sediment beds with varying resting times, plotting concentration against the distance travelled by the tracks. The graph shows that longer resting times lead to lower plume concentrations for the artificial clay.
Notably, the trend of increasing sediment concentration with higher slip ratios remains visible with the longer-rested sediment beds, further supporting the hypothesis regarding the slip ratio series.

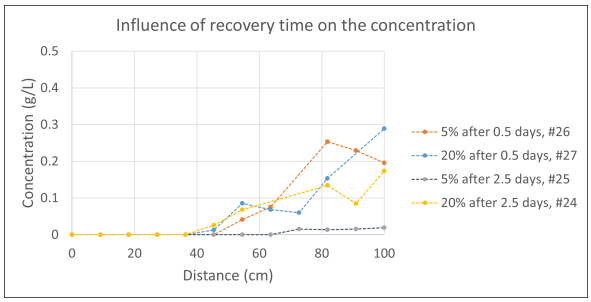


Figure 4.28: Sediment bed resting time comparison of the OBS results of the slip ratio series with the plume encounter peaks removed (Penetration = 6 mm, Velocity = 9.1 cm/s)

Additionally, Figure 4.29 shows that sediment beds with a 2.5-day resting period sustain significantly more damage. This finding supports the earlier observation from the velocity series that the plume concentration decreases when more clay is picked up.



(a) (b) (c) (d)

Figure 4.29: Sediment bed profiles for different clay recovery times, with (a) 5% slip after one night, (b) 5% slip after a weekend, (c) 20% slip after one night and (d) 20% slip after a weekend

For both 20% slip tests, regardless of resting time, the tracks continued without further pick-up after the initial chunk of clay was picked up. However, what is particularly striking is that approximately midway through the run, a larger amount of clay was suddenly picked up from the bed and this continued for the remainder of the runs (Figures 4.29c and 4.29d). No clear observations were made that can explain why sediment pick-up suddenly increased at these points.

4.4.5. Sediment Type

A test is conducted comparing deep-sea clay for the sediment bed with artificial clay. All test parameters are consistent between the two clay types, except for the sediment type. Figure 4.30 presents the concentration measured by the OBS over the distance travelled by the tracks for different sediment types. The peak concentration is 0.390 g/L for the artificial clay and 0.130 g/L for the deep-sea clay. The average concentration is 0.309 g/L for the artificial clay and 0.0882 g/L for the deep-sea clay. The concentration of the deep-sea sediment is significantly lower than that of the artificial clay.
Before the test, the undrained shear strength of the deep-sea sediment was measured using the Torvane and was found to be within the same range as the artificial clay. However, the deep-sea clay felt noticeably different to the touch, exhibiting a stiffer texture. Additionally, when smoothing the clay, it was observed that the top layer of the deep-sea clay continued to be drawn slightly in the direction of the smoothing motion, even in areas that had already been levelled. This behaviour is not observed in the artificial clay. The deep-sea clay behaves more as a whole, with particle interactions causing collective movement across the bed.

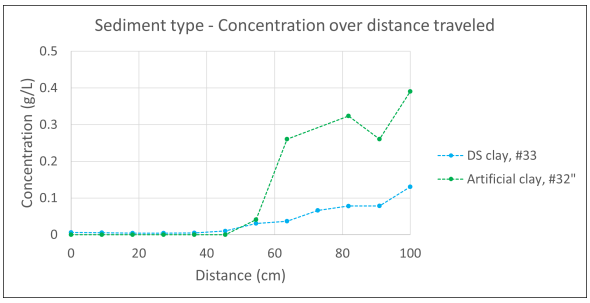


Figure 4.30: OBS results of the different sediment types with the plume encounter peaks removed (Penetration = 6 mm, Slip ratio = 10%, Velocity = 9.1 cm/s)

A clear difference is also observed when comparing the bottom profiles of both sediment types. Figure 4.31 shows that the deep-sea sediment bed remains more intact than the artificial clay bed. Additionally, the spacing between the marks left by the grousers is significantly smaller for the deep-sea clay, indicating that a larger proportion of the clay remained part of the bed rather than becoming suspended. This is further supported by Figure 4.32, which shows a greater relocation of clay at the side of the deep-sea sediment bed.



(a) (b)

Figure 4.31: Sediment bed profiles of the two different sediment types for the same settings, with (a) the artificial clay (control test) and (b) the deep-sea clay (GSR)



(a) (b)

Figure 4.32: The increase in height at the edges of the sediment bed after the test run for the different sediment types, with (a) the artificial clay (control test) and (b) the deep-sea clay (GSR)

Another notable observation during the tests is that the artificial clay began to swell upon submersion, whereas this behaviour is not observed in the deep-sea sediment. The difference is illustrated in Figure 4.33. Swelling can affect the strength of the clay, which in turn influences the concentration of the sediment plume.



(a) (b)

Figure 4.33: Submerged sediment beds, with (a) the swelling effect visible for the artificial clay (was smooth before submersion) and (b) no swelling effect visible for the deep-sea clay

4.4.6. Sediment Pick-Up at Start Location

In almost all tests, a significant chunk of clay is removed at the start of the run. Specifically, where the tracks are initially placed on the sediment bed (Figure 4.34). The section of the sediment bed that the tracks contact while in motion remains relatively undisturbed. At the end of the run, another large chunk is removed when the tracks stop and are lifted from the bed.



(a) (b)

Figure 4.34: Significant sediment pick-up at the track start (up) and finish (down) locations, where (a) the tracks are placed submerged and (b) the tracks are placed dry

During most tests, the tracks are placed on the sediment bed while the tank is still dry, preventing plume generation upon placement. To determine whether this dry placement is responsible for the initial large chunk removal, an additional test was conducted where the tracks were placed while the tank was already filled with water. The same clay removal at the starting location is observed for the submerged placement as for the dry placement.

5

Discussion

This chapter builds on the results as presented in Chapter 4. First, the limitations of the experimental setup are discussed, followed by a closer examination of the OBS calibration, Millisil and sediment bed height profiles. Next, the implications of the results presented in Section 4.4 are then discussed in detail, supported by insights from the literature and fundamental physics. Finally, the experimental findings are compared with the kinematic model and the literature in Section 5.3.

5.1. Experimental Limitations

5.1.1. Setup Limitations

In the currently used setup, the relevant components of the tracks, including the track rollers, track width, grousers and sprocket, are scaled at 1:10. The entry and exit angles at the bottom of the tracks are maintained at 30°, matching those of the SNC tracks. Other dimensions, such as the track height, have been optimised for manufacturability, while the track length has been adjusted to maximise the travel distance within the tank. The grousers are designed to be as realistic as possible, although certain simplifications were necessary to ensure feasibility while still capturing the essential characteristics of their real-world counterparts. Only the larger grousers from the SNC are used on the laboratory tracks, as the current design does not accommodate the inclusion of smaller grousers. Furthermore, the grouser shape has been simplified: instead of the original spear-point design (Figure 3.7), a 3 mm thick aluminium plate is used.

The power supplied to the cart is controlled via a control board, which features a dial that increases power when turned clockwise. It is found that even though the velocity setting on the power control board was constant between all tests, not all test runs had the same velocity. This may be due to the high sensitivity of the power regulator, combined with a dial that is difficult to set to the exact same setting. Another factor could be that variations in penetration depth alter the motion resistance. After every test run, the actual velocity is calculated from the recording.

The beams connecting the tracks to the cart are mounted on the sides of the tracks. Due to the momentum generated by the weight of the tracks, these beams do not hang perfectly vertically. As a result, the tracks are not entirely horizontal relative to the sediment bed (see Figure 5.1). This misalignment is largely compensated for by the track rollers, which apply pressure to only the center of the tracks. However, bed profile observations indicate that the left side (shown as the right side in Figure 5.1) has a larger penetration. When interpreting the results, this asymmetry should be considered, as it may lead to uneven sediment suspension.

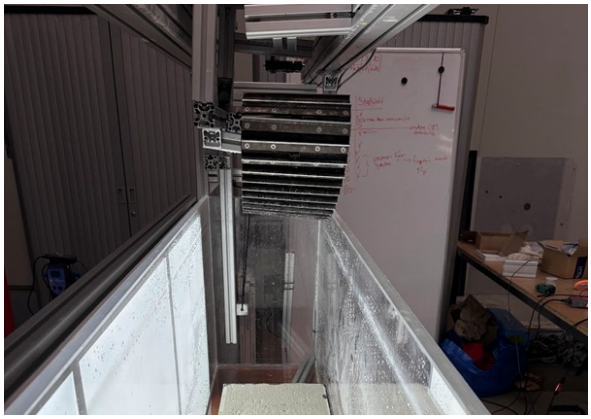


Figure 5.1: Picture of the front of the tracks where it can be observed that the tracks are not completely horizontal

In the NORI-D area, the water depth is approximately 4 km, resulting in a hydrostatic pressure of approximately 40 MPa higher than inside the laboratory tank. This pressure difference leads to variations in water conditions and sediment behaviour, which may in turn affect sediment plume dynamics and plume concentration. To address this, a clay mixture is used that mimics deep-sea clay by matching geotechnical properties of the deep-sea clay under near-bottom ocean conditions with those of the artificial clay under laboratory conditions. However, it is important to keep in mind that this approach does not account for all differences and results should therefore be interpreted with caution. During some of the experiments, relatively large bubbles were observed. Upon investigation, it was found that air can become trapped under the sediment box when filling the tank and some of this air may be released during a test. Another possible cause of large bubbles is the presence of air pockets within the sediment bed. As the tracks drive over the bed, the clay deforms and flows in the direction of the least resistance. If the bed contains air pockets, they will be forced out by the deforming clay. This affects the results because relocated clay may fill the empty air pockets instead of being pushed to the sides and middle of the tracks, meaning it is not included in the total amount of relocated clay. Additionally, this can reduce sediment suspension, as less clay is displaced sideways, resulting in a lower momentum of the relocating clay. To minimise the formation of air pockets, the sediment box is filled carefully in steps. First, about half of the clay is placed in the box and spread evenly from the middle to the sides. Then, the next layer is added and distributed in the same way. Finally, any remaining gaps are filled, and the clay surface is smoothed. If air pockets are detected during this process, they are filled with clay. However, some air pockets may have been missed.

Although the tank has an inner length of 2 meters, the tracks could only travel a distance of 1 meter. At the lowest possible velocity (7.1 cm/s), this resulted in a maximum test duration of 14 seconds. In most tests, a steady-state plume was observed from around 60% of the total distance, leaving only approximately 6 seconds of proper data collection time. After processing the data and removing points such as plume encounter peaks, the remaining data points were quite limited, making it difficult to interpret the results. It was often unclear whether the concentration plots reached a steady state. A longer test duration might have provided more conclusive results. The OBS measurements after the test run were also examined to explore whether additional data could be obtained. In this scenario, the tracks remained at the same location while the plume continued to develop. For the penetration tests, the concentration remained relatively constant for a few seconds after the run. However, for other tests, the concentration fluctuated significantly and inconsistently. Video recordings revealed that the plume exhibited different flow patterns relative to the OBS after the run, making the data less reliable. Due to this inconsistency, it was decided that post-run OBS measurements should not be used for analysis.

In some tests, larger and more numerous clay flakes were observed to be in suspension. While this phenomenon could also occur in real-world conditions, it can create a distorted impression of the measured concentration. The OBS determines turbidity based on the amount of light reflected to the sensor. When clay particles are uniformly distributed in the water, forming a fine sediment cloud, the OBS detects a significant amount of backscatter. However, suppose the same sediment mass is suspended as larger flakes instead of a fine cloud. In that case, less backscatter is observed, even though the suspended sediment concentration remains unchanged. Since the OBS is calibrated for a uniform mix-

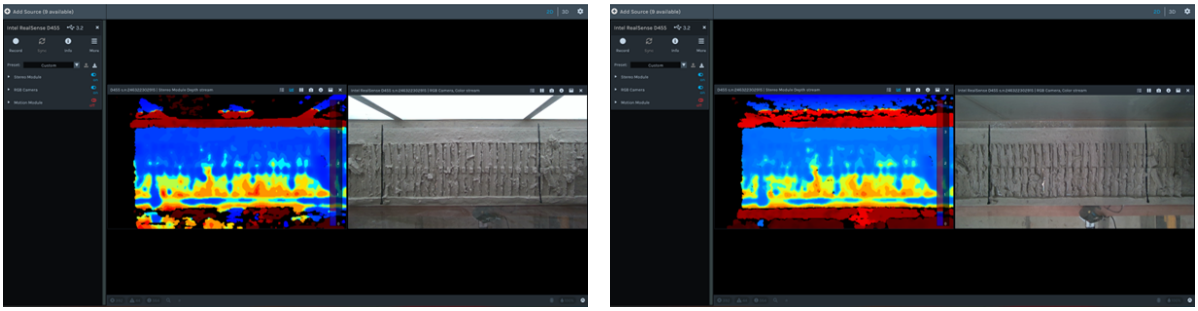
ture of fine particles, it may underestimate the true concentration when larger flakes are present. This potential error should be considered when interpreting the results if flake formation is observed during an experiment.
The undrained shear strength of the clay was measured using a Torvane. Due to the very soft consistency of the clay, the readings fell within the lower range of the device, where the accuracy of the device is limited. As no better method for measuring undrained shear strength was available, it was decided to work with a general range of 0 - 0.25 (0 kPa - 4.9 kPa) on the Torvane scale. To ensure consistency, the same recipe was used for each new batch of clay. Undrained shear strength measurements taken across multiple batches confirmed that all batches remained within this range. Nonetheless, this limitation should be considered when interpreting the results, as it may influence the validity of the underlying theories.
After each test run, the tank is drained, cleaned and refilled for the next test. The NORI-D water obviously contains sea salt, but no salt is added to the laboratory water. Still, since the study focuses on the effect of kinematics, a quantitative comparison can still be made as long as environmental aspects are kept constant.
The NORI-D near-bottom background current ranges from 2.16 cm/s to 3.16 cm/s. While this current is not strong enough to suspend cohesive sediment from the seabed by itself, it can contribute to suspending sediment once it has been loosened by the tracks. This effect should be kept in mind when interpreting the results.
The SNC also features jets to clean the tracks during operation. Although these jets were not included in the kinematic model and experiments, they can theoretically act as an additional source of sediment suspension. Nonetheless, the experiments did not indicate a strong need for continuous cleaning during driving.

5.1.2. OBS Calibration

The OBS measures turbidity, which correlates with sediment concentration. This relationship varies for each sediment type, requiring the OBS to be calibrated individually for all sediments used in the experiments. As discussed in Section 4.1.3, the calibration was conducted in a 12 L bucket, where the liquid was continuously mixed using an automatic mixer to maintain a uniform sediment concentration throughout the process. However, the liquid was mixed using a rotating mixing rod, which created a vortex and introduced centrifugal forces. These forces caused sediment particles to be pushed toward the sides of the bucket, resulting in a concentration gradient within the calibration setup. As a result, the mixture might not have been completely uniform. Despite this limitation, using the automatic mixer was the most effective method to maintain the sediment in suspension during calibration. To minimise the effects of centrifugal forces, the mixer was placed at the side of the bucket rather than in the center. This positioning allowed the mixing rod to help redistribute sediment particles that had been pushed to the sides. Although obstacles could have been placed inside the bucket to disrupt vortex formation, this was not done due to space constraints. Given the concentrations used, the relatively small diameter of the bucket and the measures taken, the resulting concentration differences were expected to be minimal. Additionally, since the OBS was always positioned at the same location within the vortex, any concentration variations would have remained consistent throughout the calibration process.
As discussed in Section 4.1.3, wet Millisil was used during the calibration process. Although the exact water content of the Millisil was not determined, this approach ensured that the uncertainty of water content was well defined. Additionally, a sample of the filtered Millisil was preserved, allowing for future determination of the fully saturated sediment's water content if required. Corrections can be applied to both the calibration and experimental data if needed.
Small masses in the range of 1.2 g were used for the artificial clay calibration. The most accurate available scale has a capacity of up to 100 kg and displays values with an accuracy of 10^{-1} g. While the scale is relatively precise, a scale with a smaller range would have been preferred for these batch sizes to ensure even greater precision.
From the collected data, a trend line was established to define the relationship between sediment concentration and OBS measurements for each sediment type. The OBS measured turbidity ranging from 12.5 FTU to 13.4 FTU when no sediment was added to the water. As a baseline for the tap water, the average of the above range (12.97 FTU) is taken. The R^2 values for the trend lines are 0.997 for Millisil and 0.998 for artificial clay. These values are very high, indicating that the data points closely follow the relationship defined by the trend line.

5.1.3. Sediment Bed Height Profiles

The 3D camera was used to measure the height of the track imprints in the sediment bed, to serve as a validation of the findings from the OBS measurements and sediment bed photographs. This method relies on optical input, so sufficient lighting is essential for accurate depth recognition. In this setup, the primary lighting was provided by LED panels positioned along the side of the tank, arranged to optimise visibility for the GoPro cameras used to record the plume. As a result, the clay surface at the top of the tank was well illuminated and accurately measured. However, the fine details of the grouser prints were located within the track trench, where shading reduced visibility. This made it difficult for the 3D camera to detect and measure their depth. In most of the height plots, these small grouser imprints are therefore not captured. Only when larger amounts of clay were relocated and the track imprints became wider were the imprints visible on camera. Due to this limitation, the height profiles may give a misleading impression of the track-bed interaction. As a result, most of the OBS data is validated using sediment bed photographs rather than the 3D camera measurements.
Although the side lighting increased the contrast between the grouser prints and the surrounding bed surface, it was ultimately decided to keep the LED panels on during the 3D scanning process. As shown in Figure 5.2, the depth profiles captured with the lights turned on are noticeably more explicit than those taken with the lights off.



(a) (b)

Figure 5.2: 3D camera depth display, with (a) the depth image when the LED panels are on and (b) when the LED panels are off

For the height profiles, only two-dimensional plots could be generated. To capture the full variation across the bed, multiple measurement lines (rows 1 - 5) were taken, as illustrated in Figure 4.13. These lines were selected to ensure that all different prints across the bed width were represented. For instance, Row 2 corresponds to the right rubber belt. It should be noted that the print is not uniform across the entire width of the belt, but this simplification was necessary for the analysis and outliers can be checked with the sediment bed pictures.
For the outer rows, measurements were taken at locations with the highest sediment relocation, located directly at the edges of the tracks. However, it is important to consider that the sides of the sediment bed are sloped for the artificial clay, resulting in a non-uniform height across the width. This high point is often very narrow, making it difficult to capture along the entire bed length, especially when the tracks did not drive perfectly straight.
Before scanning the bottom profile, the tank is drained. The ideal scenario would be to conduct the 3D scans immediately after the test run, while the sediment has not yet settled and the bed has not deformed. However, this is not feasible due to the cloudy water obscuring the camera's view. Fortunately, the sediment bed retains its shape after the tank is drained.
Sometimes, large chunks of clay are found on the sediment bed, which can influence the profile scans. These chunks typically originate from clay that adheres to the tracks during the test and falls off in the middle of the run. While these chunks should be included in the scans, as they represent a realistic scenario that could occur in the field, it is important to consider that such irregularities might impact the pattern of the track print on the sediment bed. When interpreting the scan results, these factors should be considered and can be identified with the sediment bed images.

5.1.4. Millisil

As discussed in Section 4.1.2, the filtering process was carried out in a bucket, where the water level was half that of the tank. Consequently, the settling time could be halved to 30 minutes. However, to minimise sediment loss, the filtering was conducted with great caution and an initial settling time of one hour was used in the bucket. Once it was observed that further washing did not improve water clarity and that minimal sediment was lost, the settling time was reduced to 30 minutes. Due to this cautious approach, the filtering process took longer than expected. Additionally, no instruments were available to measure the particle size distribution, so the exact characteristics of the filtered Millisil remain unknown. However, since the primary purpose of using Millisil was to test the setup, observe plume formation and identify necessary adjustments, the precise particle size distribution was not a critical factor.

Some plastic fragments were mixed with the sediment when scraping the Millisil from the bottom of the bucket. While most of these fragments were removed, some remained in the sediment. This should be considered, as their presence may influence the concentration measurements recorded by the OBS.

It was observed that the Millisil bed was highly packed, making the sediment bed very hard. Because of that, track penetration tests could not be conducted with Millisil. Additionally, a significant amount of weight had to be added to the cart. Otherwise, the cart would lift as the sediment bed pushed the tracks up. The bed was so hard that even the grousers could not fully penetrate it, causing the tracks to drive on the grousers rather than the rubber belt. Although direct comparisons between Millisil and artificial clay data is challenging, Millisil successfully served its purpose in preparing the setup for the clay experiments and providing a better understanding of plume generation.

5.2. Results Discussion

5.2.1. Seabed Penetration

For the seabed penetration experiments, it was found that as penetration depth increases, plume concentration decreases. This trend becomes evident when results are sorted by velocity and is actually the opposite of what was initially expected. It was originally assumed that the short-term pressure exerted by the tracks on the sediment bed would not be sufficient to cause soil consolidation, resulting in no compaction. Based on this assumption, it was expected that deeper penetration would lead to greater sediment displacement and, given the low undrained shear strength of the sediment, a significant portion of the displaced top layer would become suspended in the water.

The bed profile images in Appendix C and the profile height plots in Appendix D confirm that sediment displacement occurred, as evidenced by the increased height in the side regions (rows 1 and 5) and the middle region (row 3).

To understand why this occurs, the profile height plots were further examined. The initial hypothesis suggested that deeper penetration would cause more sediment to accumulate in the side and middle rows. However, OBS data indicate that although greater penetration should lead to increased sediment displacement, no additional sediment is suspended. If with a larger penetration depth, no more clay is either suspended or accumulated at the sides, it suggests that soil compaction has taken place, contrary to the original assumption.

According to existing literature, clay consolidation does not typically occur under short-term pressure. Therefore, another mechanism must be responsible for the compaction. A likely explanation lies in the preparation process for the clay mixture. The clay and water were mixed in a bucket using a mixing rod. Since the mixture was not sealed from the air, air probably became trapped within the clay. Similar to how air is incorporated into whipped cream during mixing. As a result, the clay was not completely saturated and the clay's pores contained both water and air. L. Barden and G. Pavlakis [44] found that the permeability of unsaturated cohesive soils is significantly higher for air than for water, indicating that air escapes more easily from sediment pores. This, in combination with the fact that air is more compressible than water [45], could explain the observed compaction. Video recordings of the experiments reveal small air bubbles rising from the sediment bed under track pressure, which supports this theory.

When soil compaction occurs, two key effects influence plume concentration and sediment displacement. First, instead of being pushed laterally, more clay is compressed downward, reducing the momentum of sediment movement toward the sides. Second, as the soil becomes more compacted, its physical properties change, further affecting sediment relocation and suspension behaviour. Remov-

ing air from the clay reduces the distance between particles, increasing the density, leading to a higher undrained shear strength [46]. These factors likely contribute to the observed decreased plume concentration at greater penetration depths. However, this behaviour is expected to differ in real-world deep-sea conditions. In such environments, the clay is fully saturated, meaning that short-term loading does not result in consolidation (and compaction). As a result, a larger portion of the sediment would be displaced, with a greater fraction brought in suspension. Additionally, the absence of consolidation leads to increased pore water pressure when pressure is applied, which reduces the effective stress and further decreases the undrained shear strength, potentially enhancing plume generation. Given that the laboratory tests were performed using unsaturated clay, it is difficult to directly extrapolate the observed penetration effects to real-world conditions.
Another challenge introduced by compaction is accurately determining the sediment suspension-to-relocation ratio. In addition to clay accumulating at the sides and center of the tracks or being suspended in the water column, compaction causes particles to become more densely packed beneath the tracks. It is challenging to quantify the extent to which the clay has been compacted rather than relocated or suspended. As a result, the suspension-to-relocation ratio cannot be precisely determined from this experiment, introducing uncertainty into the estimation.
In Section 4.4.2, the height profiles of the penetration series are analysed. Greater penetration depths are anticipated to lead to increased clay relocation along the sides (rows 1 and 5) and in the center of the bed (row 3). This should be reflected in the height profiles captured by the 3D camera. The results are presented in Table 4.7. No consistent relationship between penetration depth and sediment relocation can be identified from these results. Given these inconsistencies, further analysis of the sediment bed images was conducted. Aside from the 8 mm penetration depth, a visible increase in height difference between the track trench and its sides is observed with increasing penetration depth when studying the bed pictures (Appendix C). This matches expectations but is remarkably not reflected in the height profiles.
In Figure 4.21a, the concentration for 4 mm penetration is higher than that of 6 mm* penetration and this does not follow the general relation that is observed in other penetrations. The graph shows that the concentration for the 4 mm penetration is still increasing. This could suggest that the plume has not reached a steady state yet, which may explain why the concentration is lower than for the 6 mm* penetration.

5.2.2. Driving Velocity

Based on the literature study, it was anticipated that increasing the track velocity would result in a higher track rotation velocity and cause the clay to be pushed out harder from under the tracks. This higher rotation speed would cause the grousers to sweep sediment more forcefully into the water during both the scooping phase and the pull-out. At the same time, the increased push would result in more momentum during sediment relocation. Both of these effects contribute to enhanced sediment suspension.
Unfortunately, only a limited number of data points could be generated per experiment because of the limited length of the tank. This makes it challenging to draw firm conclusions or establish reliable trends. This challenge becomes even more pronounced at higher velocities, where the number of measurements decreases even further. While the available data is the best that could be obtained with the length of the tank, some degree of uncertainty should be considered when interpreting the results. Additionally, higher velocities reduce the OBS's ability to capture the developed sediment plume. At these speeds, the OBS encounters the sediment plume before it has had sufficient time to develop. This was the issue for the tests at 14.3 cm/s and 20.0 cm/s, where the OBS never reached the steady-state plume. For the 20.0 cm/s test, this effect is particularly evident in both the video and the OBS data. The footage clearly shows that the OBS never reaches the steady-state plume. Figure 4.22 shows that the concentration is still increasing at the end of the test, indicating that the plume had not yet reached a steady state when the measurements stopped. At 14.3 cm/s, the OBS almost reaches the steady-state plume but nearly misses it. The pattern of concentration over distance travelled at this velocity follows a similar trend to that at 9.1 cm/s and 11.1 cm/s, but appears delayed. Consequently, these two tests were excluded from the results interpretation. This leaves four velocities for which a steady-state plume was successfully recorded. While a larger dataset would have been ideal, the results still allow for the identification of a meaningful trend. Using a linear fit, a trend line was fitted to both the peak and average concentration values, as shown in Figure 4.23. Theoretically, this trend should intersect

the origin, since no plume is generated when the tracks are stationary. However, including this intersection significantly worsened the fit. Zhu et al. [47] found that the erosion rate of cohesive soils often correlates linearly with the shear stress induced by the flow velocity for sediment beds with uniform soil properties over depth. However, this refers to sediment suspension caused by flow, not excavation by a tracked vehicle. As no reliable theoretical basis is found for a specific fit type in this context, a linear fit was chosen solely based on the data points. This provides a reasonable estimate of sediment concentration within the tested velocity range (7.1 cm/s – 11.1 cm/s). With R^2 values of approximately 0.96 for both fits, the relationship observed within this velocity range is considered sufficiently robust.
It was also observed that the sediment beds remained more intact during tests conducted at higher velocities. The tracks tend to extract larger chunks of clay from the bed at lower velocities. This is particularly interesting because, although the plume concentration increases at higher velocities, the sediment bed shows less visible disturbance. This suggests that a smaller plume is developed when more clay is picked up. When the tracks pick up clay, it either remains trapped between the grousers or falls off, but settles quickly due to its large mass. In either case, the clay does not contribute to the plume concentration when picked up by the tracks. Additionally, when the tracks pick up the top layer of the sediment bed, the grousers cannot scoop it. It is observed that the plume is the densest at the moment that the grousers are scooping.
One possible explanation for why less clay is picked up at higher velocities is that the clay may adhere more strongly to the tracks over time. At higher velocities, the contact time between the tracks and the clay is reduced, potentially resulting in less adhesion and, consequently, less clay being picked up.

5.2.3. Slip Ratio

When the tracks experience a slip, the sediment trapped between the grousers becomes remoulded. The higher the slip ratio, the more intensely the soil is remoulded. According to literature [29], remoulded clay exhibits a lower undrained shear strength compared to its undisturbed state. The SNC tracks experience a remoulding distance of 0.18 m at a 6% slip ratio. To achieve a comparable decrease in undrained shear strength through remoulding, the laboratory tracks must cover the same remoulding distance. However, due to the laboratory tracks' shorter contact length, reaching 0.18 m would require a slip ratio of 220%, which is highly unrealistic and would result in impractically high rotation speeds. Even when scaling the remoulding distance down by a factor of 10 (i.e., 0.018 m), the required slip ratio would still be 22%, which is considered too high because of its broader impact on track–soil interaction, not just remoulding. As a compromise, a standard slip ratio of 10% was selected for the experiments, with an additional test at 20% slip to examine the effects at a more realistic remoulding distance.
A 10% slip ratio means that the remoulding distance for the laboratory tracks is relatively short, and therefore the remoulding effect is expected to be minimal. Combined with the clay already having a low undrained shear strength, the overall effect on plume generation is likely negligible.
It was observed in Section 4.4.4 that the 20% slip ratio does not follow the pattern of the other slip ratios. Upon closer investigation, the recordings reveal that at 20% slip, the tracks pick up a relatively long chunk of clay at the start. This is illustrated in Figure 5.3 by the yellow line. Previous findings (Section 4.4.1) indicate that the densest plume is generated when the tracks are scooping. However, in this case, the prolonged sediment pickup delays plume formation due to the scooping process. As a result, the OBS does not measure a steady-state plume before the tracks reach the end of the sediment box. This is reflected in Figure 4.25, where the concentration starts increasing at a greater distance than the other slip ratios and still rises when the test concludes. Since the fully developed plume is not captured, the 20% slip test is excluded from the results interpretation.

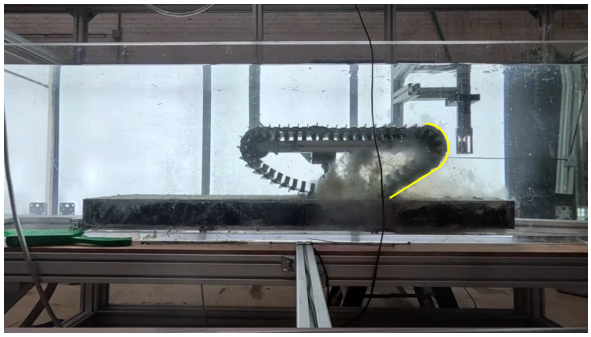


Figure 5.3: Sediment pick-up at the start location for the 20% slip test, with the length of the chunk marked by the yellow line

The relationship observed for the other slip ratios shows that sediment concentration increases with higher slip ratios. This effect is attributed to the rise in track rotation speed. As expected from the velocity category, the higher rotation speed increases the momentum of the clay as it is swept into the water through the scooping and pull-out mechanisms, thereby enhancing sediment suspension.
This relation is also shown in Figure 4.26. A linear fit is applied to illustrate this relationship. There is always a baseline concentration at 0% slip, which depends on the values of the other parameters. Since no data is available for slip ratios above 10%, it is difficult to predict how the relationship would evolve at higher slip ratios. It is expected, however, that beyond a certain slip ratio, the concentration would show little further increase. Once the remoulding has progressed sufficiently, the undrained shear strength reaches its maximum reduction due to the remoulding effect. From a kinematic perspective, at very high slip ratios, almost all sediment between the grousers would already be relocated. Nevertheless, the increased track rotation speed would generate additional flow around the tracks, which could theoretically cause a slight further increase in concentration by picking up more sediment. This effect, however, is expected to be minimal. Based on the findings of this study, a linear trend best fits the data within the 0% – 10% slip range. According to the literature, slip ratios higher than 10% are not typically expected in real-world conditions.
The trend lines closely follow the data points, with relatively high R-squared values: 0.999 for peak concentrations and 0.970 for average concentrations. However, it should be noted that not all slip ratios are conducted at the same velocity. Specifically, the 0% slip test was conducted at 8.3 cm/s, whereas the 5% and 10% slip tests were conducted at 9.1 cm/s. Since velocity is known to influence plume concentration, a correction is investigated for the 0% slip test to account for this difference. Based on the trend line from the velocity series (Figure 4.23), it was found that the average plume concentration increases by approximately 0.0618 g/L per 1 cm/s. Applying this correction, the average concentration for the 0% slip test increases from 0.071 g/L to 0.12 g/L and the peak concentration from 0.096 g/L to 0.14 g/L. The corrected plot is shown in Figure 5.4, where the trend line for average concentrations shows a significantly improved fit, with an R^2 value of 0.994. Although the R-squared value for peak concentrations decreased slightly to 0.996, this change is minimal and the average concentration is considered a more representative metric for assessing sediment suspension.

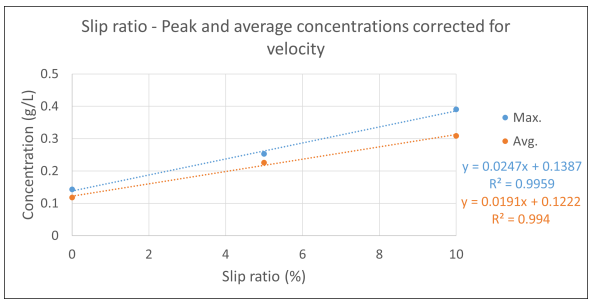


Figure 5.4: The peak and average concentrations of the slip ratio series with the 0% slip correct according to the velocity relation

When examining the bed profiles for different slip ratios, as shown in Figure 4.27, it becomes clear that the sediment bed sustains more damage at higher slip ratios. Previously, it was observed that plume concentration tends to decrease when the tracks pick up more clay. However, the slip ratio results appear to suggest the opposite trend. One possible explanation is that the clay chunks between the grousers are more easily picked up because they have already been loosened by displacement due to slip. However, as discussed earlier, the higher rotation velocities associated with slip further enhance sediment suspension. This may suggest that track rotation velocity may have a greater influence on plume concentration than sediment pick-up.
The slip ratio is not included in the kinematic model. If it was included, the effect of the forward movement of the whole tracks would have less impact on the sediment relocation reduction. This effect is better explained in Appendix A. Including a slip ratio would result in more sediment relocation by the scooping and pull-out mechanisms.

Table 5.1: Calculated error for the slip ratio of each winch (1 meter driving distance)

slip ratio (%)	Track rotation distance (mm)	Error (%)
0	1008	0.8
5	1047	0.3
10	1110	0.9
20	1204	0.3

Before conducting the tests, the required winch diameters were calculated to achieve the intended slip ratios. After the experiments, video recordings were used to verify whether the tracks actually experienced the correct slip ratio. This was done by tracking the distance travelled by a single grouser and comparing it to the target distance, allowing the error in slip ratio for each winch to be calculated. An overview of these results is provided in Table 5.1. All deviations were found to be less than 1%. Given the small magnitude of these errors and the fact that the exact distance travelled by a grouser could not be precisely determined, it was decided not to adjust the slip ratios in the final results. The potential correction would still carry uncertainty and is unlikely to affect the outcomes significantly. Therefore, the original slip ratios were retained in the analysis.

5.2.4. Sediment Type

One experiment was conducted using deep-sea sediment from the GSR area to observe plume generation and the interaction between the tracks and the natural sediment. Although according to the literature study deep-sea sediment may behave differently under laboratory conditions compared to real-world environments, the experiment was considered valuable for potentially revealing useful insights.
The results, presented in Figure 4.30, show that the deep-sea sediment generates significantly less plume compared to the artificial clay. Besides the sediment type, the only notable difference is that the artificial clay was allowed to rest overnight. In contrast, the deep-sea clay was thoroughly stirred before being put in the sediment box and subsequently inside the tank. Stirring was necessary as the sediment had been stored in a plastic barrel for some time and appeared friable. Torvane measurements indicated similar undrained shear strength values for both materials. However, the deep-sea clay felt noticeably stiffer to the touch. This suggests that its compressive strength may be higher. Additionally, during bed preparation, it was observed that the clay, within approximately 10 cm of the smoothing location, tended to be dragged along in the direction of the smoothing tool. This behaviour is not observed in the artificial clay and suggests that the deep-sea clay may have longer interparticle bonds, implying a higher tensile strength.
The mineralogical composition of the clays may explain these behavioural differences. While the montmorillonite/smectite fraction falls within the same range, the ratios of other minerals differ. The artificial clay has a high kaolinite content, which forms a structure resembling pillars of stacked pancakes (Figure 5.5a). In contrast, the deep-sea sediment contains a more significant proportion of illite, which has a more interwoven, overlapping structure (Figure 5.5b), making it perhaps more tightly bound together.



(a) (b)

Figure 5.5: Microscopic structure of clay minerals, with (a) kaolinite [48] and (b) illite [49] (edited)

Figures 4.31 and 4.32 clearly show a distinct difference in the bed profiles. The deep-sea clay bed displays minimal voids between the grouser prints and much of the relocated clay appears to have accumulated along the edges of the bed. This indicates that the clay behaves more as a whole, with particles that are less easily separated from one another.
This experiment highlights the behavioural differences between the two types of clay. It emphasises the importance of matching the artificial clay to the deep-sea clay based on more than undrained shear strength and water content. Although achieving a full match was not feasible within the scope of this study, the selected artificial clay represented the best available alternative.

5.2.5. Recovery Time

Although it was not initially intended to investigate the recovery time of the clay, a coincidental set of experiments introduced variation in this parameter, revealing a significant impact. Figure 4.28 shows that the sediment bed produced a noticeably lower concentration when it was allowed to rest for 2.5 days, compared to just 0.5 days. While the Torvane measurements indicated similar undrained shear strength values in both cases, a noticeable difference in strength was observed by hand. This suggests that the clay regains strength over time through thixotropic behaviour [50]. The observed reduction in plume generation is likely due to this increase in strength during the recovery period.
Behaviours like higher stiffness were also observed for the deep-sea clay, which led to the idea of comparing the deep-sea sediment results with those from the longer recovery time tests. This comparison is presented in Figure 5.6. It is important to note that the deep-sea sediment test is conducted at a slip ratio of 10%, meaning the conditions are not entirely identical. The results show that the deep-sea sediment concentration falls between the 5% and 20% weekend recovery tests, aligning with the observed relationship that plume concentration increases with slip ratio. This may suggest that artificial clay begins to behave more like deep-sea sediment when given a longer recovery time. However, it should be noted that the deep-sea clay was tested on the same day it was prepared, resulting in a short recovery period.

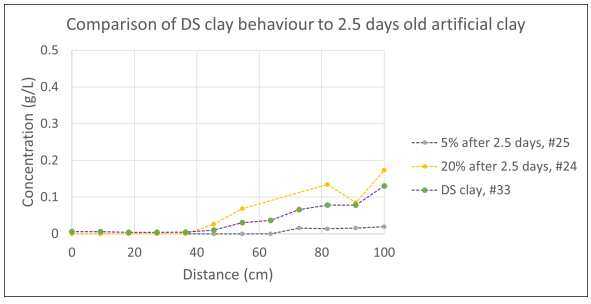


Figure 5.6: Comparison of the OBS results for different recovery times and deep-sea sediment (Penetration = 6 mm, Velocity = 9.1 cm/s)

It is also observed that when the recovery time is longer, the bed experiences more damage from sediment pick-up. The cause of this remains unclear. All tests were conducted at the same velocity (9.1 cm/s). One possible explanation is that the adhesion of the clay increased over time. Miedema [51] states that adhesion relates to cohesion, where an increasing cohesion results in an increasing adhesion. Higher adhesion may lead to more clay being picked up, while increased cohesion causes the particles to bind more strongly together. As a result, the picked-up clay remains in larger chunks that settle quickly, rather than dispersing into a plume.

5.3. Comparison of Experimental Results with Other Models

The literature review (3.4) included an analysis of the Patania II “selfie” manoeuvre, which served as a reference point for this thesis study. Building on the analysis of the SNC track design, a kinematic model was developed to estimate sediment relocation. Using these foundations, a scaled model of the SNC tracks was constructed and tested under controlled laboratory conditions. This section presents a comparison between the experimental results, the Patania II data and the predictions of the kinematic model.

Experiments were conducted with artificial clay and deep-sea clay. For the comparison, the results from the tests with the standard parameter settings are used: 23_Clay_P6_V5_S10 and 01_DSClay_P6_V5_S10. The sediment suspension and relocation are first evaluated for the artificial clay. The artificial clay experiments yielded an average plume concentration of 0.309 kg/m^3. For the discharge calculations, it is assumed that the plume concentration is uniform over both the height and width of the plume. The plume height is approximately 0.35 m and the width is approximately 0.25 m (Figure 5.7). From this, the sediment suspension rate for the artificial clay experiment is calculated to be 0.0270 kg/m.



Figure 5.7: Plume dimensions of the imitaion clay with the standard settings (test 23)

The sediment height profile plots show that the average height increase in row 1 is 0.002 m, in row 3 is 0.006 m and in row 5 is 0.005 m (Figure 4.13). Outliers, such as large clay clumps, were excluded by comparing the height profiles with the corresponding sediment bed images. The height increase in row 3 is uniform across the width, whereas rows 1 and 5 display a slope. While a height increase is observed immediately adjacent to the track imprint, no increase is visible at the edge of the box (Figure 4.32b). To account for this, the width of the elevated section at the side is halved when calculating sediment relocation. The elevated widths of the rows are presented in Table 5.2.

The height increase in row 3 results from the openings in the middle of the track belt. As the track moves forward, only half of row 3 retains this height increase, as the other half is pushed away by the grouser plates (Figure 4.13). Based on these observations, a total relocated sediment volume of $2.01 \cdot 10^{-4}$ m^3 is calculated. With an artificial clay density of 1254 kg/m^3 (= 12.3 · 1000 / 9.81) and a water content of 244%, the total sediment relocation is determined to be 0.0731 kg/m.

Table 5.2: Summary of the average height profiles of rows 1, 3 and 5 for both sediment types

		Row 1	Row 3	Row 5
Artificial clay	**Height (m)**	0.002	0.006	0.005
	Width (m)	0.035	0.026	0.035
	Profile	Sloped	Uniform	Sloped
Deep-sea clay	**Height (m)**	0.0035	0.0045	0.003
	Width (m)	0.05	0.026	0.05
	Profile	Uniform	Uniform	Uniform

The same method is applied to calculate the sediment suspension and relocation for the deep-sea clay experiment. The average concentration measured for the deep-sea clay is 0.0882 kg/m^3. The dimensions of the sediment plume are shown in Figure 5.8, from which a sediment suspension rate of 0.00582 kg/m is determined.
The heights and widths of rows 1, 3, and 5 for the deep-sea clay are presented in Table 5.2. Unlike the artificial clay, sediment accumulation at the sides of the box is uniform across the entire 0.05 m width. This results in a total relocated volume of $3.84 \cdot 10^{-4}$ m^3. For the density and water content of the deep-sea clay, the average values reported by GSR are used, respectively 1350 kg/m^3 and 200%. Based on these values, a sediment relocation of 0.173 kg/m is determined.

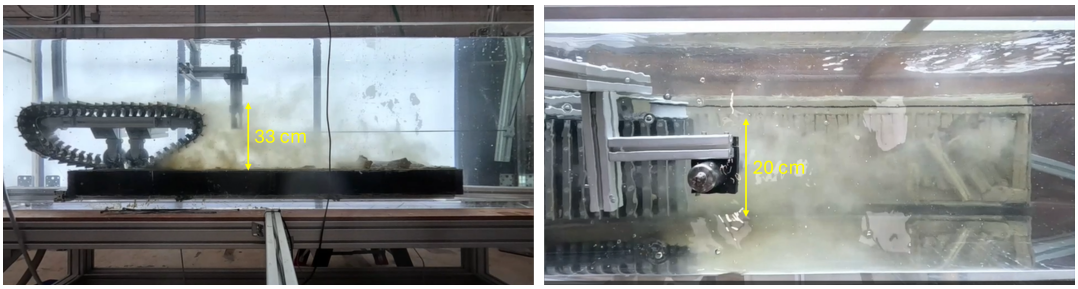


Figure 5.8: Plume dimensions of the deep-sea clay with the standard settings

For Patania II, a sediment suspension rate of 8.33 ± 5.56 kg/m was determined, based on an assumed wake width of 4 × 4 m. To enable comparison with the experimental results, this wake is scaled to match the dimensions of the experimental plumes, resulting in a suspension rate of 0.0456 ± 0.0304 kg/m for the artificial clay plume and 0.0344 ± 0.0229 kg/m for the deep-sea clay plume. No data are available on seabed sediment relocation for Patania II. Therefore, this cannot be calculated.
To compare the kinematic model with the experimental results, the experimental parameters were applied in the model, including the laboratory track dimensions and the properties used above to calculate sediment relocation. The model predicts total sediment relocation rates of 0.533 kg/m for the artificial clay and 0.658 kg/m for the deep-sea clay.
A summary of the suspension rate, relocation rate and total sediment relocation for all methods is provided in Table 5.3.

Table 5.3: Summary of the sediment suspension and relocation calculations

	Suspension (kg/m)	Relocation (kg/m)	Total (kg/m)
Experiment AC	0.0270	0.0731	0.100
Experiment DSC	0.00582	0.173	0.178
Patania II (AC)	0.0456 ± 0.0304	-	-
Patania II (DSC)	0.0344 ± 0.0229	-	-
Kinematic model AC	-	-	0.533
Kinematic model DSC	-	-	0.658

When comparing the results presented in Table 5.3, it is evident that the sediment suspension rates from the executed experiments (AC = 0.0270 kg/m, DSC = 0.00582 kg/m) are close to those of Patania II (AC = 0.0456 ± 0.0304 kg/m, DSC = 0.0344 ± 0.0229 kg/m). In particular, the experimental sediment suspension rate for the artificial clay falls within the range reported for Patania II.
In contrast, the total sediment relocation predicted by the kinematic model is approximately five times larger for the artificial clay and about four times larger for the deep-sea clay compared to the experimental results. This suggests that the Patania II approach aligns more closely with the experimental observations and that there seems to be a deviation in the kinematic model. This could be explained by the fact that the total sediment relocation estimates, as predicted by the kinematic model, do not account for clay adhering to the tracks or soil compaction. The penetration tests demonstrated that, due to compaction, sediment suspension actually decreased, contrary to the literature-based expectation that suspension would increase with penetration depth. This highlights the significant role of compaction and may explain the larger differences observed for the kinematic model. Therefore, a correction factor, compensating for the compaction ratio, could be part of an updated version of the kinematic model.
Given that the Patania II data match the experimental results the best, the sediment suspension rate for the SNC collector is most reliably estimated using the Patania II scaling approach. The wake of the SNC is approximately 4 × 6 m. Scaling the artificial clay experiment suspension rate to the SNC wake yields an estimated sediment suspension rate of approximately 7.41 kg/m. Scaling the original Patania II results to the SNC wake gives a suspension rate of 12.5 ± 8.34 kg/m. The actual SNC track plume generation is likely to fall within this range.

6

Conclusion & Recommendations

This study has aimed to improve the understanding of the sediment plume generated by the tracks of the Seabed Nodule Collector in the NORI-D area. The knowledge gained from this study can contribute to minimising the environmental impact of deep-sea mining activities on the seabed.
A literature review has been conducted to investigate the characteristics of the NORI-D area and the track design to identify the sources of plume generation. Based on these findings, a kinematic model was developed to estimate sediment relocation due to these sources. Additionally, a series of experiments focusing on seabed penetration depth, driving velocity, slip ratio and sediment type were conducted to pursue the remaining research objectives.
This chapter addresses the research objectives by building on the knowledge acquired throughout the study. It begins by presenting the conclusions drawn from the study to address the sub-questions, followed by the main research question and concludes with recommendations for future research and suggestions for potential improvements.

6.1. Conclusion

On the basis of literature, the developed kinematic model and experiments performed in this study, major conclusions can be summarised as follows:

- Literature has suggested that the undrained shear strength is a critical soil property influencing plume generation, with water content identified as one of the key factors affecting this strength. However, experiments showed a significant difference for the different sediment types. This indicates that the artificial clay should match the deep-sea clay not only in undrained shear strength and water content, but also in additional properties to ensure comparable plume generation behaviour. The characteristics responsible for the differing behaviour between the two clay types could be adhesion and compressive strength. Although these properties were not measured, manual examination of the clay suggested notable differences.
- By the track design analysis during the literature study, three primary sources of sediment suspension were identified: seabed penetration by the tracks, scooping caused by the grousers at the final track roller and the pull-out of grousers partially embedded in the sediment. The experiments later confirmed these sediment suspension sources.
- Based on the literature, fully saturated sediment under deep-sea conditions would be expected to undergo relocation, leading to greater sediment suspension with increasing penetration depth. However, the experiments indicate that increased penetration depth was associated with reduced plume generation, which is attributed to soil compaction. This discrepancy is likely specific to the test environment. To minimise seabed penetration, the submerged weight of the collector can be reduced or the contact area with the seabed can be increased to distribute the load better.
- According to the literature, an increased slip ratio is expected to lead to an increased sediment suspension. Experiments also showed that increased slip ratios lead to more plume generation due to higher track rotation speeds (at a constant vehicle speed). An additional aim of the study is

to examine how changes to the track design influence plume generation. Slip can be minimised by improving traction, which can be achieved by widening or lengthening the grousers or by increasing the contact area. Obviously, this must be well-balanced since enlarging grousers also amplifies the scooping effect, which may, in turn, increase plume generation.

- Driving velocity plays a complex role. The experiments showed that while higher velocities tend to generate more plume, they cause less physical disturbance to the seabed. Conversely, lower speeds result in more sediment being picked up, reducing scooping and pull-out effects.
- A kinematic model was developed to determine the sediment relocation by each source. When comparing the model's predictions of total sediment relocation to the experimental results (Table 5.3), it was found that the model overestimates total sediment relocation by a factor of five for artificial clay and four for deep-sea clay. These differences are not extremely large given the complexity of the phenomenon, but they do suggest that a model purely based on kinematics is incomplete.
- **The main research objective was to find the turbidity source term for the suspended sediment originating from the tracks of the SNC. Based on the literature review, it can be concluded that seabed penetration is one of the main contributors to sediment suspension. The experiment results indicate that the velocity is the governing parameter by increasing track rotation speed and the momentum of clay relocation. One key finding was that by scaling the Patania II test results to the experimental setup, a close match was found. Therefore, the test results are scaled according to the approach used for the Patania II study. The most reliable range found in this study for SNC track plume generation is between 12.5 ± 8.34 kg/m while driving in a straight, forward motion.**

6.2. Recommendations

6.2.1. Experiments

This study is one of the first to investigate plume generation caused by tracks on deep-sea sediment. Therefore, it is already a valuable outcome that the study reveals phenomena and track-soil relations worth investigating. However, expanding the dataset would significantly improve the reliability of the results and help make trends more apparent. First, testing a broader range of parameters and conducting multiple repetitions for each test setting would have been beneficial. This would make it easier to identify outliers and reduce their impact on the results. Achieving this would require a larger time frame to complete all the necessary tests. Second, increasing the number of data points per test by extending the length of the sediment bed would also enhance the findings. In the current setup, whether the OBS measurements captured a steady-state concentration was not always certain. Additionally, the tracks were unable to complete a full rotation. To address this, a driving distance of 5 meters (five times the current design) is recommended, based on the current scaled track dimensions.

Although the artificial clay matched the deep-sea clay regarding water content and undrained shear strength, the experimental results differed significantly. This suggests that the current matching criteria are insufficient. Additional properties, such as compressive strength, water absorption capacity and adhesion, should also be considered. Developing a representative artificial clay may require a dedicated study. However, doing so would greatly improve the relevance and accuracy of future experiments.

It is also strongly recommended to de-air the soil and ensure it is fully saturated before testing. This process requires time, but neglecting it can lead to distorted results as discussed in Chapter 5. Fully saturating the clay would add considerable value to the outcomes.

6.2.2. Setup Design

Due to manufacturing constraints, the tracks were mounted to the cart using an L-shaped structure. This caused the tracks to hang slightly crooked, resulting in uneven pressure distribution on the sediment bed and uneven plume generation. For future studies, it is advised to attach both sides of the tracks to the propulsion system, eliminating any tilting moment caused by the weight of the tracks.

Track rotation occasionally stuttered during the experiments. Two improvements can help achieve smoother rotation: (1) shortening the track roller guidance plates and increasing the sprocket diameter for a better fit, and (2) ensuring that the track tension does not act directly on the sprocket. This can be achieved by adding an additional track roller beside the sprocket to absorb the tensioning force,

allowing the sprocket to rotate more freely.
Improving the method for measuring height profiles is also highly recommended, as accurate profiles greatly enhance the value of the data. Sonar would work very well, although it is costly. The current 3D camera setup has demonstrated its ability to measure depth accurately, provided the sediment bed is well-illuminated. Therefore, a practical and affordable improvement would be adding extra light sources from multiple angles to ensure the entire bed is visible to the camera.
Finally, the current power regulator made conducting experiments at precise velocities difficult. To improve accuracy and repeatability, it is recommended to use a velocity or power controller that allows for programmable speed settings.

6.2.3. Future Research

For future research, a key improvement to the kinematic model and to the overall ability to estimate sediment suspension would be a more accurate understanding of the suspension-to-relocation ratio for each plume generation mechanism. To accomplish this, the individual sources should be better isolated and influencing factors such as soil pick-up and compaction should either be prevented or quantifiable during testing. A potential improvement could be to conduct tests with individual components of the tracks rather than testing the entire track assembly. For example, testing only the scooping action of a single grouser would allow for better isolation of the plume generation source. This approach would help rule out or control other influences.
Additionally, exploring how the plume behaves and how the track-soil interaction is affected under more realistic deep-sea conditions would be insightful. Conducting experiments using actual deep-sea water or simulating deep-sea conditions more closely would not only enhance the realism of the tests but also help evaluate the reliability of results obtained under simplified conditions. If the influence of these environmental factors proves to be minimal, it could justify the continued use of simpler test setups in the future.
Another interesting design consideration is the grouser angle. The grousers are positioned perpendicular to the track pads in the current track design. This orientation, combined with the angle at which the tracks exit the seabed, causes the grousers to relocate clay during the pull-out phase. By adjusting either the grouser angle or the exit angle, so that the grouser is pulled out along its length, it may be possible to reduce or even eliminate sediment disturbance during pull-out. This could lead to a much cleaner track exit, with less plume generation. Investigating the effects of these adjustments on, for example, traction performance, would be a valuable next step in optimising track design for minimal environmental impact.
Lastly, introducing a current to the experimental setup would also be interesting. Such a current could influence plume behaviour and enhance sediment suspension, offering a more comprehensive understanding of how these systems behave in real-world scenarios.

References

[1] T. Kuhn & A. Wegorzewski & C. Rühlemann & A. Vink. “Composition, Formation, and Occurrence of Polymetallic Nodules”. In: *Deep-Sea Mining: Resource Potential, Technical and Environmental Considerations*. Ed. by R. Sharma. Cham: Springer International Publishing, 2017, pp. 23–63.

[2] *Environmental Impact Statement - Testing of polymetallic nodule collector system components in the NORI-D contaract area, Clarion-Clipperton Zone, Pacific Ocean*. Tech. rep. Nauru Ocean Resources Inc., 2021.

[3] P.E. Halbach & A. Abram. *Study Report about the surface sediments in the NE Pacific Clarion-Clipperton Zone (CCZ)*. Sept. 2013.

[4] Balaram Vysetti. “Deep-sea mineral deposits as a future source of critical metals, and environmental issues - a brief review”. In: *Minerals and Mineral Materials* 2.2 (2023).

[5] M. Lodge & D. Johnson & G. Le Gurun & M. Wengler & P. Weaver & V. Gunn. “Seabed mining: International Seabed Authority environmental management plan for the Clarion–Clipperton Zone. A partnership approach”. In: *Marine Policy* 49 (2014), pp. 66–72.

[6] T.R. Vonnahme & M. Molari & F. Janssen & F. Wenzhöfer & M. Haeckel & J. Titschack & A. Boetius. “Effects of a deep-sea mining experiment on seafloor microbial communities and functions after 26 years”. In: *Science Advances* 6.18 (2020), eaaz5922.

[7] P.P.E. Weaver & J. Aguzzi & R.E. Boschen-Rose & A. Colaço & H. de Stigter & S. Gollner & M. Haeckel & C. Hauton & R. Helmons & D.O.B. Jones & H. Lily & N.C. Mestre & C. Mohn and L. Thomsen. “Assessing plume impacts caused by polymetallic nodule mining vehicles”. In: *Marine Policy* 139 (2022), p. 105011.

[8] *Environmental Impact Statement - Small-scale testing of nodule collector components on the seafloor of the Clarion-Clipperton Fracture Zone and its environmental impact*. Tech. rep. Global Sea Mineral Resources, 2018.

[9] D.O.B. Jones & M.B. Arias & L. Van Audenhaege & S. Blackbird & C. Boolukos & G. Bribiesca-Contreras & J.T. Copley & A. Dale & S. Evans & B.F.M. Fleming & A.R. Gates & H. Grant & M.G.J. Hartl & V.A.I. Huvenne & R.M. Jeffreys & P. Josso & L.D. King & E. Simon-Lledó & T. Le Bas & L. Norman & B. O’Malley & T. Peacock & T. Shimmield & E.C.D. Stewart & A.K. Sweetman & C. Wardell & D. Aleynik & A.G. Glover. “Long-term impact and biological recovery in a deep-sea mining track”. In: *Nature* (2025).

[10] I.Z. Gazis & H. de Stigter & J. Mohrmann & k. Heger & M. Diaz & B. Gillard & M. Baeye & M.E. Veloso-Alarcón & K. Purkiani & M. Haeckel & A. Vink & L. Thomsen & J. Greinert. “Monitoring benthic plumes, sediment redeposition and seafloor imprints caused by deep-sea polymetallic nodule mining”. In: *Nat. Commun.* 16.1 (2025), p. 1229.

[11] R. Helmons & S. Alhaddad & C. Chassagne & M. Elerian & G. Keetels & A. Kirichek & L. Thomsen. “Turbidity at the Source: Aiming for Minimized Sediment Dispersion During Deep-Sea Mining”. In: *Deep-Sea Mining and the Water Column: Advances, Monitoring and Related Issues*. Ed. by R. Sharma. Cham: Springer Nature Switzerland, 2024, pp. 209–242.

[12] C. Muñoz-Royo & R. Ouillon & S. El Mousadik & M.H. Alford & T. Peacock. “An in situ study of abyssal turbidity-current sediment plumes generated by a deep seabed polymetallic nodule mining preprototype collector vehicle”. In: *Science Advances* 8.38 (2022), eabn1219.

[13] *Pilot Mining Test close-out report*. Tech. rep. Allseas Engineering B.V., 2023.

[14] International Seabed Authority. *Clarion Clipperton Fracture Zone*. June 2024. URL: `https://www.isa.org.jm/map/clarion-clipperton-fracture-zone`.

[15] *Geotechnical Data Report, NORI-D – Project Zero Area*. Tech. rep. The Metals Company – Nauru Ocean Resources Inc, June 2024.

[16] Z. Li & Jf. Zhang & Qh. Zhang & Xt. Shen & Tq. Chen. “Effects of organic matter and salinity on the flocculation of kaolinites in a settling column”. In: *J Hydrodyn* 33 (2021), pp. 159–156.

[17] J. Wood. “Ocean Current Observations Throughout the Water Column in the Clarion-Clipperton Fracture Zone, Tropical North Pacific”. In: *Deep-Sea Mining and the Water Column: Advances, Monitoring and Related Issues*. Ed. by R. Sharma. Cham: Springer Nature Switzerland, 2024, pp. 335–376.

[18] M. Broeren. “The lifting of a deep sea mining collector from a soft cohesive soil”. MA thesis. TU Delft, 2021.

[19] B. Grupe & H.J. Becker & H.U. Oebius. “Geotechnical and sedimentological investigations of deep-sea sediments from a manganese nodule field of the Peru Basin”. In: *Deep Sea Research Part II: Topical Studies in Oceanography* 48.17 (2001), pp. 3593–3608.

[20] B. Widjaja & K. Kurniawan. “Development of Relationship between Liquid Limit and Clay Content for West Java Soils”. In: *IOP Conf. Ser. Mater. Sci. Eng.* 1007.1 (2020), p. 012102.

[21] L. Daoudi & A. Knidiri & H.E.B.E. Idrissi & B. Rhouta & N. Fagel. “Role of the texture of fibrous clay minerals in the plasticity behavior of host materials (Plateau du Kik, Western High Atlas, Morocco)”. In: *Applied Clay Science* 118 (2015), pp. 283–289.

[22] W.A. White & E. Pichler. *Water-Sorption Characteristics of Clay Minerals*. 1959.

[23] J.K. Mitchell & K. Soga. *Fundamentals of Soil Behavior*. 3rd ed. John Wiley & Sons, Inc., 2005.

[24] S. Alhaddad & D. Mehta & R. Helmons. “Mining of deep-seabed nodules using a Coandă-effect-based collector”. In: *Results in Engineering* 17 (2023), p. 100852.

[25] *Track Plate pull test report*. Tech. rep. Allseas Engineering B.V., 2020.

[26] *Propulsion system general arrangement*. EQ-916CE-000-G-A-001. Rev. A. Allseas Engineering B.V. 2022.

[27] *Propulsion track assembly*. EQ-916CE-100-G-A-001. Rev. B. Allseas Engineering B.V. 2021.

[28] J.Y. Wong. *Theory of Ground Vehicles*. 3rd ed. John Wiley & Sons, Ltd, 2001.

[29] N. Morgan & D. Cathie & J. Pyrah & J. Steward. *Tracked Subsea Trencher Mobility And Operation In Soft Clays*. The International Society of Offshore and Polar Engineers, July 2007.

[30] *DNV-RP-C212 Offshore Soil Mechanics and Geotechnical Engineering*. Tech. rep. DNV, 2019.

[31] K. Terzaghi. *Theoretical Soil Mechanics*. John Wiley & Sons, Inc, 1943.

[32] *Collector PMT track results*. Tech. rep. Allseas Engineering B.V., 2023.

[33] *Collector PMT test results*. Tech. rep. Allseas Engineering B.V., 2023.

[34] *Effect of Object In-situ Time on Bottom Breakout*. Vol. All Days. OTC Offshore Technology Conference. 1975, OTC-2184–MS.

[35] S.H. Baek & T. Bong & J. Cho & G.B. Shin. “Evaluation of the Soil Thrust on Continuous Tracks Considering Independent Soil Shearing by Grousers”. In: *Applied Sciences* 12.21 (2022).

[36] *High Grouser Detailed Design Drawing Alsseas Harvester*. EQ-916CE-161-M-V-001. Rev. C. Allseas Engineering B.V. 2021.

[37] T. Peacock. *The GSR Patania II Expedition: Technical Achievements & Scientific Learnings*. Tech. rep. Global Sea Mineral Resources.

[38] *Seabed soil mixtures to mimic CCZ soil*. Tech. rep. Deltares, 2020.

[39] *Product characteristics FT-S1*. Tech. rep. n.d. Sibelco.

[40] *Product Data Sheet CEBOGEL® OCMA*. Tech. rep. n.d. CEBO.

[41] *Millisil M10*. Tech. rep. Sibelco, 2012.

[42] O. Chmiel & I. Baselt & A. Malcherek. “Applicability of Acoustic Concentration Measurements in Suspensions of Artificial and Natural Sediments Using an Acoustic Doppler Velocimeter”. In: *Acoustics* 1.1 (2019), pp. 59–77.

[43] *Calibration_JUB_20211014*. Tech. rep. n.d. Royal Netherlands Institute for Sea Research.

[44] L. Barden & G. Pavlakis. “Air and water permeability of compacted unsaturated cohesive soil”. In: *J. Soil Sci.* 22.3 (1971), pp. 302–318.

[45] NPTEL. *Introduction and Fundamental Concepts*. URL: https://archive.nptel.ac.in/content/storage2/courses/112104118/lecture-2/2-4-compressibility.htm#:~:text=For%20example%2C%20the%20bulk%20modulus,times%20more%20compressible%20than%20water. (visited on 2025).

[46] E.M. Morales. *Soil Mechanics Principles in Construction Practice*. 2024. URL: https://pgatech.com.ph/soil-mechanics-principles-in-construction-practice/.

[47] Y. Zhu & J. Lu & H. Liao & J. Wang & B. Fan & S. Yao. “Research on cohesive sediment erosion by flow: An overview”. In: *Sci. China Ser. E-Technol. Sci.* 51.11 (2008), pp. 2001–2012.

[48] Media Storehouse. *Kaolinite. Scanning electron microscope image of kaolinite (x 4.00K)*. URL: https://www.mediastorehouse.com/mary-evans-prints-online/kaolinite-8616537.html (visited on 2025).

[49] M. Cheraghalikhani & H. Niroumand & L. Balachowski. “Micro- and nano-Illite to improve strength of untreated-soil as a nano soil-improvement (NSI) technique”. In: *Sci. Rep.* 14.1 (2024), p. 10862.

[50] B. Tang & B. Zhou & L. Xie & J. Yin & S. Zhao & Z. Wang. “Strength Recovery Model of Clay during Thixotropy”. In: *Adv. Civ. Eng.* 2021.1 (2021), pp. 1–11.

[51] S.A. Miedema. *The Delft Sand, Clay & Rock Cutting Model*. 3rd ed. Dr.ir. S.A. Miedema, 2019.

[52] *Wheel Guide Detailed design drawing*. EQ-916CE-170-M-V-001. Rev. A3. Allseas Engineering B.V. 2021.

[53] *Track Belt Assembly - General Arrangement*. EQ-916CE-100-G-A-002. Rev. A3. Allseas Engineering B.V. 2021.

A

Kinematic Sediment Relocation Model

In this appendix, the calculations for the amount of relocated sediment will be explained in more detail.

A.1. Seabed Penetration

The volume of relocated sediment due to seabed penetration is equal to the volume of the rut that is created by the tracks. The volume of all deformed sediment is calculated with the following equation:

$$A_{middle} = W_{trackroller} \cdot N_g \cdot W_{middle} = 0.07 \cdot 6.90 \cdot 0.26 = 0.126m^2 \tag{A.1}$$

$$A_{beltgab} = W_{grouser} \cdot N_g \cdot 6 \cdot W_{beltgab} = 0.045 \cdot 6.90 \cdot 6 \cdot 0.01 = 0.0186m^2 \tag{A.2}$$

$$A_{tracks} = A_{middle} + A_{beltgab} + (b - W_{middle} - W_{beltgab}) \cdot s = 0.126 + 0.0186 + (2 - 0.26 - 0.01) \cdot 1 = 1.82m^2 \tag{A.3}$$

$$V_{penetration,mix} = z \cdot A_{tracks} \cdot n_t = 0.06 \cdot 1.82 \cdot 2 = 0.219m^3 \tag{A.4}$$

Where A_{middle} is the area between the rubber belt in the middle of the track that is pushed into the soil (governed by the width of the track roller guidance), $W_{trackroller}$ is the width of the track roller guidance [52], N_g is the average number of grousers in 1 m of tracks, W_{middle} [53] is the distance between the rubber belts in the middle of the track, $A_{beltgab}$ is the sum of al the smaller areas between the rubber belts that is pushed into the soil (governed by the width of the grouser mountings), $W_{grouser}$ [36] is the width of the grouser mounting, $W_{beltgab}$ [53] is the smaller distance between the rubber belts, A_{tracks} is the total contact area of the tracks on the seabed, n_t is the number of tracks, z is the penetration depth of the tracks, b is the total width of the tracks and s the distance traveled. The mass of this volume is calculated with:

$$m_{penetration,mix} = V_{penetration,mix} \cdot (\frac{\gamma_s}{g} + \rho_w) = 0.219 \cdot (\frac{2.33}{9.81} + 1048) = 281kg \tag{A.5}$$

Where δ_s is the submerged unit weight of the solids, δ_w is the unit weight of sea water and g is the gravitational acceleration. To calculate the mass of only the sediment, the following equation is used:

$$m_{penetration} = \frac{m_{mix}}{u+1} = \frac{281}{3.64+1} = 60.6kg \tag{A.6}$$

Where u is the mass water content.

A.2. Scooping

To calculate the sediment relocation caused by the scooping effect, the motion of a grouser relative to the seabed must be determined. The track roller rotates by 30° and shifts to the right. This movement is illustrated in Figure A.1. In the figure, the brown line represents the seabed after penetration by the tracks, the blue line indicates the grouser, and the grey circle represents the track roller.

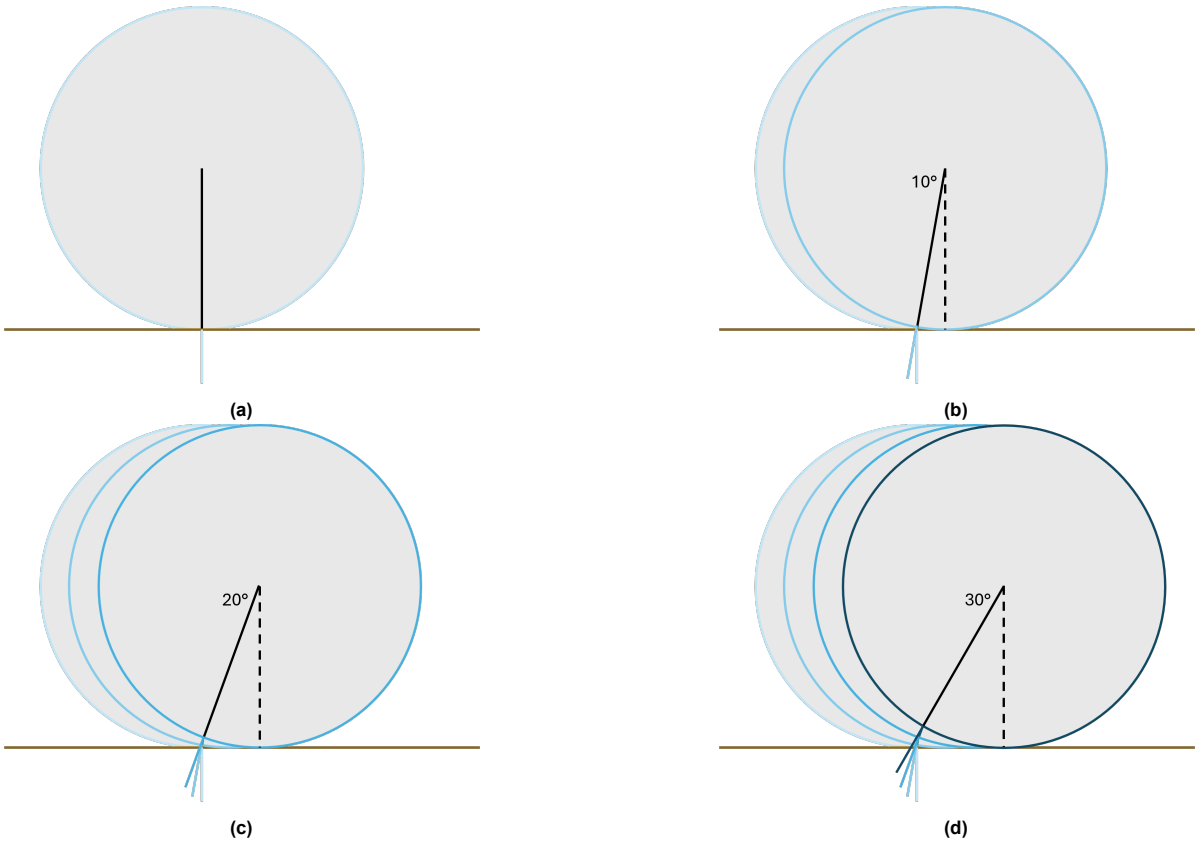


Figure A.1: Propagation of the grouser during the scooping effect shown at different angles

It follows that the area of relocated soil after seabed penetration corresponds to the region marked in red in Figure A.2.

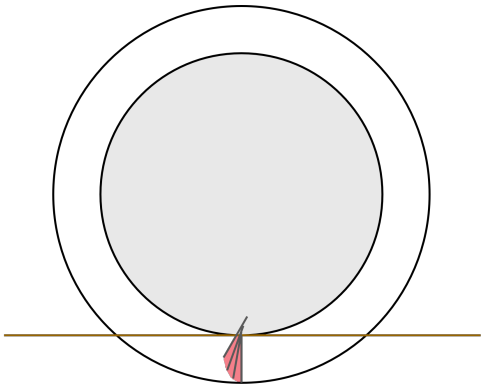
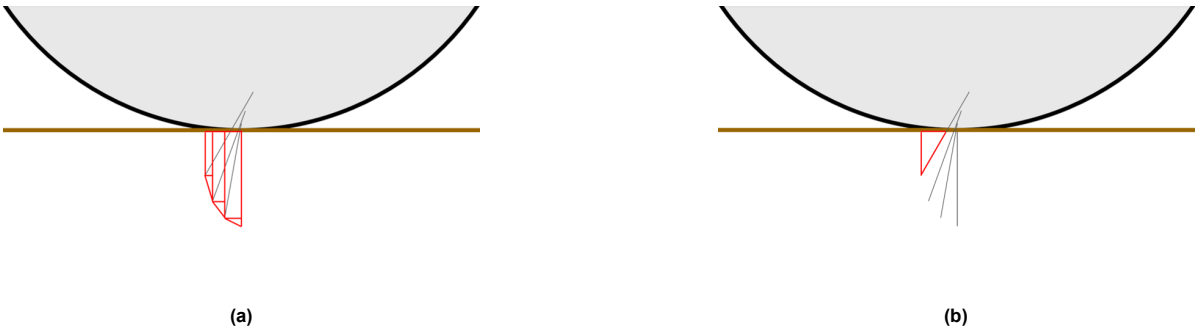


Figure A.2: Area of deformed soil due to scooping of the grouser

Calculations were performed in Python to determine the area. The rubber belt thickness and the height of the track roller guidance are included in the radius of the track roller. The 30-degree turn is divided

by n number of grouser positions. For every step, the grouser location is determined. The area over the interval between the grouser tips is calculated numerically (see figure A.3a). Then, the untouched part, as illustrated in Figure A.3b, is subtracted. It is important to note that the tracks have two types of grousers: high grousers (125 mm) and low grousers (75 mm). It is determined that 18.2 kg of dry sediment is relocated due to scooping by the high grouser and 4.78 kg by the low grouser. The codes used for this calculation are displayed below.
Calculations are performed using Python to calculate the area. The 30-degree rotation is divided into n grouser positions. At each step, the grouser's location is determined. The area over the interval between the grouser tips is numerically calculated (see figure A.3a). Subsequently, the untouched part, as illustrated in figure A.3b, is subtracted. The code used for this calculation is provided below.



(a) (b)

Figure A.3: Area of relocated soil calculations for scooping, with (a) being the illustration of the interval for the numeric calculation and (b) the part that will be subtracted from the numeric calculation

```
import numpy as np
import matplotlib.pyplot as plt

"""Soil and water properties"""
rho_w = 1048 #kg/m3
gamma_submerged = 2.33 #kN/m3
rho_submerged = gamma_submerged * 1000 / 9.81 #kg/m3
rho_mix = rho_w + rho_submerged #kg/m3
wc = 364 #%

"""Track dimensions"""
degree = 30 #degree

penetration = 0.06 #m
s_traveled = 1 #m

n_t = 2 #number of tracks
W_t = 2 #m

D_tr = 0.745 #m
r_tr = D_tr / 2 + 0.013 + 0.028 #m, radius track roller, incl. rubber belt (13 mm) and wheel guidance (28 mm)

L_gh = 0.125 #m
r_gh = r_tr + L_gh #m, distance grouser tip to track roller center
W_gh = 2 #m
s_g = 0.29 #m
n_g = s_traveled / s_g #number of high grousers per distance traveled

L_gl = 0.075 #m
r_gl = r_tr + L_gl #m
W_gl = 1.520 #m

"""Scooping High Grouser"""
n = 200 #the result does not change significantly and the code is still fast
x = np.zeros(n + 1)
y = np.zeros(n + 1)
x1 = np.zeros(n + 1)
x2 = np.zeros(n + 1)
```

```
y1 = np.zeros(n + 1)
y2 = np.zeros(n + 1)
delta_x = np.zeros(n)
delta_y = np.zeros(n)
A1 = np.zeros(n)
A2 = np.zeros(n)
delta_degree = degree / n

x[0] = 0
y[0] = L_gh

alpha = 0
Aa = 0

for i in range (n):
    alpha = alpha + delta_degree
    x1[i + 1] = r_gh * np.sin(alpha * (np.pi / 180)) #grouser displacement backward
    x2[i + 1] = (alpha / 360) * (r_tr * 2 * np.pi) #track displacement forward
    x[i + 1] = abs(x2[i + 1] - x1[i + 1]) #resultant displacement (forward)
    y1[i + 1] = r_gh * np.cos(alpha * (np.pi / 180)) #grouser tip vertical distance from
        track roller center
    y2[i + 1] = r_tr
    y[i + 1] = y1[i + 1] - y2[i + 1] #grouser tip dept
    delta_x[i] = x[i + 1] - x[i]
    delta_y[i] = y[i] - y[i + 1]
    A1[i] = delta_x[i] * y[i + 1] #area of rectangular part interval
    A2[i] = delta_x[i] * delta_y[i] / 2 #area of sloping part interval
    Aa = Aa + A1[i] + A2[i] #total simplified area (area has a curve which is simplified by a
         mulitple intervals with each it own linear slope)

Ab = np.tan(degree * (np.pi / 180)) * y[n] * y[n] / 2
A_grouserh_s = Aa - Ab #m2

V_grouserh_s_mix = A_grouserh_s * W_gh * n_t #m3
m_grouserh_s_mix = V_grouserh_s_mix * rho_mix #kg
m_scoopingh_mix = m_grouserh_s_mix * n_g #kg
m_scoopingh = m_scoopingh_mix / ((wc / 100) + 1) #kg

print('The total removed mass by high grouser scoop is ', m_scoopingh, ' kg.')

"""Scooping Low Grouser"""
x = np.zeros(n + 1)
y = np.zeros(n + 1)
x1 = np.zeros(n + 1)
x2 = np.zeros(n + 1)
y1 = np.zeros(n + 1)
y2 = np.zeros(n + 1)
delta_x = np.zeros(n)
delta_y = np.zeros(n)
A1 = np.zeros(n)
A2 = np.zeros(n)
delta_degree = degree / n

x[0] = 0
y[0] = L_gl

alpha = 0
Aa = 0

for i in range (n):
    alpha = alpha + delta_degree
    x1[i + 1] = r_gl * np.sin(alpha * (np.pi / 180)) #grouser displacement backward
    x2[i + 1] = (alpha / 360) * (r_tr * 2 * np.pi) #track displacement forward
    x[i + 1] = abs(x2[i + 1] - x1[i + 1]) #resultant displacement (forward)
    y1[i + 1] = r_gl * np.cos(alpha * (np.pi / 180)) #grouser tip vertical distance from
        track roller center
    y2[i + 1] = r_tr
    y[i + 1] = y1[i + 1] - y2[i + 1] #grouser tip dept
    delta_x[i] = x[i + 1] - x[i]
    delta_y[i] = y[i] - y[i + 1]
    A1[i] = delta_x[i] * y[i + 1] #area of rectangular part interval
```

```
    A2[i] = delta_x[i] * delta_y[i] / 2 #area of sloping part interval
    Aa = Aa + A1[i] + A2[i] #total simplified area (area has a curve which is simplified by a
         mulitple intervals with each it own linear slope)

Ab = np.tan(degree * (np.pi / 180)) * y[n] * y[n] / 2
A_grouserl_s = Aa - Ab #m2

V_grouserl_s_mix = A_grouserl_s * W_gl * n_t #m3
m_grouserl_s_mix = V_grouserl_s_mix * rho_mix #kg
m_scoopingl_mix = m_grouserl_s_mix * n_g #kg
m_scoopingl = m_scoopingl_mix / ((wc / 100) + 1) #kg

print('The total removed mass by low grouser scoop is ', m_scoopingl, ' kg.')
```

A.3. Pull-out

After the scooping phase, the grouser is pulled out of the seabed at a 15-degree angle relative to the seabed's vertical axis. This angle is determined with the following calculations:

$$s_{bw} = cos(\beta) \cdot s_{traveled} = cos(30) \cdot 1 = 0.866m \tag{A.7}$$

$$s_{up} = sin(\beta) \cdot s_{traveled} = sin(30) \cdot 1 = 0.5m \tag{A.8}$$

$$s_{fw} = s_{traveled} - s_{bw} = 1 - 0.688 = 0.134m \tag{A.9}$$

$$\epsilon = tan^{-1}(s_{fw}/s_{up}) = tan^{-1}(0.134/0.5) = 15 \tag{A.10}$$

Where s_{bw} and s_{up} are the distance traveled by the grouser relative to the tracks in backward and upward direction, β the angle of the tracks relative to the seabed, $s_{traveled}$ is the distance traveled by the tracks, s_{fw} the distance traveled by the grouser relative to the seabed and ϵ the pull-out angle. The area of relocated soil by the high grouser is indicated in red in Figure A.4.

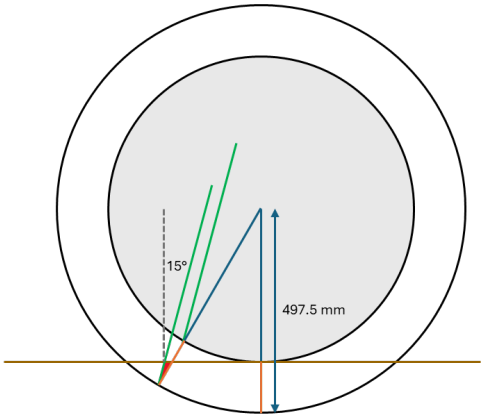


Figure A.4: Area of deformed soil due to the pull out process of the high grouser

This area is equal to the difference between the areas illustrated in Figure A.5, which is done by the following equations:

$$z_{g,h} = cos(\beta) \cdot r_{g,h} - r_{tr} = cos(30) \cdot 0.539 - 0.414 = 0.0529m \tag{A.11}$$

$$z_{g,l} = cos(\beta) \cdot r_{g,l} - r_{tr} = cos(30) \cdot 0.489 - 0.414 = 0.00955m \tag{A.12}$$

$$A_{grouser,h,po} = \frac{(tan(\beta) - tan(\epsilon)) \cdot z_{g,h}^2}{2} = \frac{(tan(30) - tan(15)) \cdot 0.0529^2}{2} = 4.32 \cdot 10^{-4} m^2 \quad \text{(A.13)}$$

$$A_{grouser,l,po} = \frac{(tan(\beta) - tan(\epsilon)) \cdot z_{g,l}^2}{2} = \frac{(tan(30) - tan(15)) \cdot 0.00955^2}{2} = 1.41 \cdot 10^{-5} m^2 \quad \text{(A.14)}$$

Where z_{gh} and z_{gl} are the depth of the high grouser tip and low grouser tip, r_{gh} and r_{gl} are the radius of the high grouser tip and low grouser tip to the center of the track roller, r_{tr} the radius of the track roller (incl. the rubber belt thickness (13 mm) and the track roller guidance height (28 mm)) and $A_{grouserh,po}$ and $A_{grouserl,po}$ the area of the relocated wet sediment by pull-out for a single high grouser and low grouser.

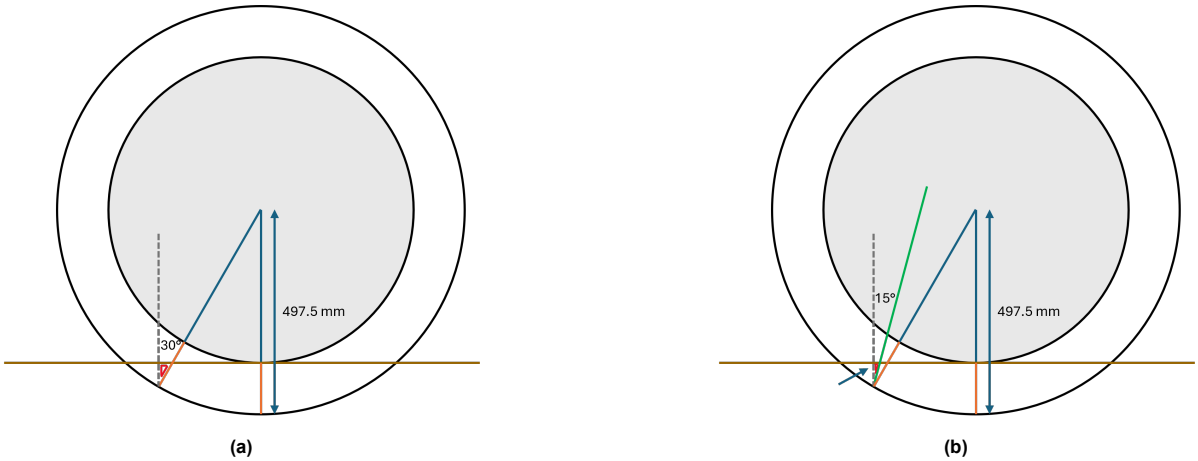


Figure A.5: Two used areas to calculate the area that is relocated due to the pull-out, with (a) the area between the seabed, grouser and vertical of the seabed and (b) the area between the seabed, grouser propogation line and vertical of the seabed

From these areas, it is estimated that a mass of 1.65 kg dry sediment is relocated by pulling the high grousers out of the seabed and 0.0410 kg by the low grousers. This is done with the following equations:

$$V_{grouser,h,po,mix} = A_{grouser,h,po} \cdot W_{g,h} \cdot n_t = 4.32 \cdot 10^{-4} \cdot 2 \cdot 2 = 1.73 \cdot 10^{-3} m^3 \quad \text{(A.15)}$$

$$V_{grouser,l,po,mix} = A_{grouser,l,po} \cdot W_{g,l} \cdot n_t = 1.41 \cdot 10^{-5} \cdot 1.520 \cdot 2 = 4.29 \cdot 10^{-5} m^3 \quad \text{(A.16)}$$

$$m_{grouser,h,po,mix} = V_{grouser,h,po,mix} \cdot \rho_{mix} = 1.73 \cdot 10^{-3} \cdot 1286 = 2.22kg \quad \text{(A.17)}$$

$$m_{grouser,l,po,mix} = V_{grouser,l,po,mix} \cdot \rho_{mix} = 4.29 \cdot 10^{-5} \cdot 1286 = 0.0552kg \quad \text{(A.18)}$$

$$m_{pullout,h,mix} = m_{grouser,h,po,mix} \cdot n_g = 2.22 \cdot 3.45 = 7.66kg \quad \text{(A.19)}$$

$$m_{pullout,l,mix} = m_{grouser,l,po,mix} \cdot n_g = 0.0522 \cdot 3.45 = 0.190kg \quad \text{(A.20)}$$

$$m_{pullout,h} = \frac{m_{pullout,h,mix}}{u+1} = \frac{7.66}{3.64+1} = 1.65kg \quad \text{(A.21)}$$

$$m_{pullout,l} = \frac{m_{pullout,l,mix}}{u+1} = \frac{0.190}{3.64+1} = 0.0410kg \tag{A.22}$$

Where $v_{grouser,h,po,mix}$ and $v_{grouser,l,po,mix}$ are the volume of relocated wet sediment by pull-out for a single high- and low grouser, $W_{g,h}$ and $W_{g,l}$ are the width of a high- and low grouser, n_t the number of tracks, $m_{grouser,h,po,mix}$ and $m_{grouser,l,po,mix}$ the mass of relocated wet sediment by pull-out for a single high- and low grouser, ρ_{mix} the bulk density of the wet soil, $m_{pullout,h,mix}$ and $m_{pullout,l,mix}$ the mass of relocated wet sediment by the pull-out for the high- and low grousers, n_g the average number of grousers per meter track and $m_{pullout,h}$ and $m_{pullout,l}$ the mass of relocated dry sediment by the pull-out for the high- and low grousers.

B

Raw OBS Data

The raw data measured by the OBS for each test are given in Tables B.1 - B.18. The OBS was in a steady-state plume from the red line. The average values for Figures 4.23 and 5.4 are taken from the point between the red line and the maximum distance (100 centimeters). Some turbidity values are grey. Those values are from measurements when a chunk of sediment was in front of the sensor.

Table B.1: 01_Clay_P6_V10_S10

01_Clay_P6_V10_S10					
Real time	Time (s)	Distance (cm)	Temperature (°C)	Turbidity (FTU)	Concentration (g/L)
15:12:20	0	0.00	10.42	3.80	0.0000
15:12:21	1	14.29	10.42	4.60	0.0000
15:12:22	2	28.57	10.42	4.82	0.0000
15:12:23	3	42.86	10.43	22.02	0.0185
15:12:24	4	57.14	10.46	134.05	0.2474
15:12:25	5	71.43	10.46	283.97	0.5537
15:12:26	6	85.71	10.45	234.79	0.4532
15:12:27	7	100.00	10.45	512.22	1.0200
15:12:28	8		10.44	340.65	0.6695
15:12:29	9		10.44	295.09	0.5764
15:12:30	10		10.43	251.51	0.4874
15:12:31	11		10.43	221.88	0.4268
15:12:32	12		10.43	233.72	0.4510
15:12:33	13		10.44	197.19	0.3764
15:12:34	14		10.44	203.11	0.3885
15:12:35	15		10.44	121.58	0.2219
15:12:36	16		10.45	103.80	0.1856
15:12:37	17		10.45	90.35	0.1581
	18				
	19				
	20				
	21				
	22				
	23				
	24				

Table B.2: 02_Clay_P6_V5_S10

02_Clay_P6_V5_S10					
Real time	Time (s)	Distance (cm)	Temperature (°C)	Turbidity (FTU)	Concentration (g/L)
11:04:01	0	0.00	9.91	7.33	0.0000
11:04:02	1	7.14	9.91	7.27	0.0000
11:04:03	2	14.29	9.91	7.31	0.0000
11:04:04	3	21.43	9.90	7.86	0.0000
11:04:05	4	28.57	9.90	8.33	0.0000
11:04:06	5	35.71	9.91	9.46	0.0000
11:04:07	6	42.86	9.90	11.91	0.0000
11:04:08	7	50.00	9.90	24.17	0.0229
11:04:09	8	57.14	9.89	32.38	0.0397
11:04:10	9	64.29	9.89	44.49	0.0644
11:04:11	10	71.43	9.89	112.06	0.2024
11:04:12	11	78.57	9.90	136.98	0.2534
11:04:13	12	85.71	9.91	96.19	0.1700
11:04:14	13	92.86	9.92	103.43	0.1848
11:04:15	14	100.00	9.92	95.94	0.1695
11:04:16	15		9.92	89.74	0.1568
11:04:17	16		9.92	61.96	0.1001
11:04:18	17		9.92	74.76	0.1262
11:04:19	18		9.93	66.60	0.1096
11:04:20	19		9.93	56.35	0.0886
11:04:21	20		9.93	55.71	0.0873
11:04:22	21		9.93	51.72	0.0792
11:04:23	22		9.93	50.24	0.0761
11:04:24	23		9.93	43.02	0.0614
11:04:25	24		9.93	36.87	0.0488

Table B.3: 04_Clay_P6_V5_S10

04_Clay_P6_V5_S10					
Real time	Time (s)	Distance (cm)	Temperature (°C)	Turbidity (FTU)	Concentration (g/L)
10:43:02	0	0.00	9.13	3.96	0.0000
10:43:03	1	7.69	9.13	3.37	0.0000
10:43:04	2	15.38	9.13	3.16	0.0000
10:43:05	3	23.08	9.12	3.19	0.0000
10:43:06	4	30.77	9.12	3.73	0.0000
10:43:07	5	38.46	9.11	6.27	0.0000
10:43:08	6	46.15	9.11	9.30	0.0000
10:43:09	7	53.85	9.11	414.54	0.8204
10:43:10	8	61.54	9.11	193.05	0.3679
10:43:11	9	69.23	9.11	84.26	0.1457
10:43:12	10	76.92	9.11	112.97	0.2043
10:43:13	11	84.62	9.11	105.16	0.1884
10:43:14	12	92.31	9.12	114.85	0.2081
10:43:15	13	100.00	9.13	69.47	0.1154
10:43:16	14		9.14	47.93	0.0714
10:43:17	15		9.14	51.37	0.0785
10:43:18	16		9.14	27.76	0.0302
10:43:19	17		9.13	43.44	0.0623
10:43:20	18		9.13	31.04	0.0369
10:43:21	19		9.12	30.97	0.0368
10:43:22	20		9.12	22.50	0.0195
10:43:23	21		9.12	26.15	0.0269
10:43:24	22		9.12	23.62	0.0218
10:43:25	23		9.12	23.55	0.0216
	24				

Table B.4: 05_Clay_P0_V5_S10

05_Clay_P0_V5_S10					
Real time	Time (s)	Distance (cm)	Temperature (°C)	Turbidity (FTU)	Concentration (g/L)
13:00:09	0	0.00	8.57	3.73	0.0000
13:00:10	1	7.69	8.57	3.19	0.0000
13:00:11	2	15.38	8.56	3.02	0.0000
13:00:12	3	23.08	8.55	3.53	0.0000
13:00:13	4	30.77	8.55	3.95	0.0000
13:00:14	5	38.46	8.55	5.06	0.0000
13:00:15	6	46.15	8.55	32.93	0.0408
13:00:16	7	53.85	8.55	52.73	0.0812
13:00:17	8	61.54	8.55	180.65	0.3426
13:00:18	9	69.23	8.56	137.01	0.2534
13:00:19	10	76.92	8.57	190.65	0.3630
13:00:20	11	84.62	8.57	151.66	0.2834
13:00:21	12	92.31	8.58	99.56	0.1769
13:00:22	13	100.00	8.58	83.59	0.1443
13:00:23	14		8.58	82.44	0.1419
13:00:24	15		8.58	87.00	0.1513
13:00:25	16		8.58	78.30	0.1335
13:00:26	17		8.58	79.37	0.1357
13:00:27	18		8.58	75.52	0.1278
13:00:28	19		8.58	78.78	0.1345
13:00:29	20		8.59	67.14	0.1107
13:00:30	21		8.59	69.45	0.1154
13:00:31	22		8.59	69.90	0.1163
13:00:32	23		8.59	70.27	0.1171
	24				

Table B.5: 06_Clay_P10_V5_S10

06_Clay_P10_V5_S10					
Real time	Time (s)	Distance (cm)	Temperature (°C)	Turbidity (FTU)	Concentration (g/L)
08:15:46	0	0.00	11.27	8.42	0.0000
08:15:47	1	8.33	11.27	8.33	0.0000
08:15:48	2	16.67	11.27	7.78	0.0000
08:15:49	3	25.00	11.26	7.91	0.0000
08:15:50	4	33.33	11.25	9.62	0.0000
08:15:51	5	41.67	11.25	11.48	0.0000
08:15:52	6	50.00	11.25	36.24	0.0475
08:15:53	7	58.33	11.25	49.94	0.0755
08:15:54	8	66.67	11.25	132.84	0.2449
08:15:55	9	75.00	11.26	71.68	0.1200
08:15:56	10	83.33	11.27	61.57	0.0993
08:15:57	11	91.67	11.28	83.16	0.1434
08:15:58	12	100.00	11.29	111.21	0.2007
08:15:59	13		11.30	113.35	0.2051
08:16:00	14		11.30	122.21	0.2232
08:16:01	15		11.30	123.81	0.2265
08:16:02	16		11.30	107.35	0.1928
08:16:03	17		11.30	91.09	0.1596
08:16:04	18		11.30	81.87	0.1408
08:16:05	19		11.30	85.91	0.1490
08:16:06	20		11.30	78.63	0.1341
08:16:07	21		11.30	73.47	0.1236
	22				
	23				
	24				

Table B.6: 07_Clay_P2_V5_S10

07_Clay_P2_V5_S10					
Real time	Time (s)	Distance (cm)	Temperature (°C)	Turbidity (FTU)	Concentration (g/L)
10:32:39	0	0.00	8.55	6.63	0.0000
10:32:40	1	8.33	8.55	5.89	0.0000
10:32:41	2	16.67	8.55	5.80	0.0000
10:32:42	3	25.00	8.55	5.69	0.0000
10:32:43	4	33.33	8.55	5.98	0.0000
10:32:44	5	41.67	8.56	8.13	0.0000
10:32:45	6	50.00	8.56	26.22	0.0271
10:32:46	7	58.33	8.56	47.97	0.0715
10:32:47	8	66.67	8.56	174.08	0.3292
10:32:48	9	75.00	8.56	69.68	0.1159
10:32:49	10	83.33	8.57	78.19	0.1333
10:32:50	11	91.67	8.58	122.16	0.2231
10:32:51	12	100.00	8.59	130.73	0.2406
10:32:52	13		8.59	87.51	0.1523
10:32:53	14		8.60	111.79	0.2019
10:32:54	15		8.60	74.49	0.1257
10:32:55	16		8.61	84.49	0.1461
10:32:56	17		8.61	97.86	0.1734
10:32:57	18		8.61	83.84	0.1448
10:32:58	19		8.61	93.70	0.1649
10:32:59	20		8.61	79.99	0.1369
10:33:00	21		8.61	80.02	0.1370
10:33:01	22		8.61	68.18	0.1128
	23				
	24				

Table B.7: 08_Clay_P4_V5_S10

08_Clay_P4_V5_S10					
Real time	Time (s)	Distance (cm)	Temperature (°C)	Turbidity (FTU)	Concentration (g/L)
12:48:12	0	0.00	8.73	3.44	0.0000
12:48:13	1	7.69	8.73	3.28	0.0000
12:48:14	2	15.38	8.72	2.43	0.0000
12:48:15	3	23.08	8.71	2.20	0.0000
12:48:16	4	30.77	8.70	2.51	0.0000
12:48:17	5	38.46	8.70	2.98	0.0000
12:48:18	6	46.15	8.70	6.27	0.0000
12:48:19	7	53.85	8.70	22.80	0.0201
12:48:20	8	61.54	8.71	266.38	0.5177
12:48:21	9	69.23	8.74	143.48	0.2666
12:48:22	10	76.92	8.75	70.71	0.1180
12:48:23	11	84.62	8.77	86.94	0.1511
12:48:24	12	92.31	8.77	91.34	0.1601
12:48:25	13	100.00	8.78	107.64	0.1934
12:48:26	14		8.78	97.65	0.1730
12:48:27	15		8.79	73.32	0.1233
12:48:28	16		8.78	97.53	0.1728
12:48:29	17		8.78	98.82	0.1754
12:48:30	18		8.78	98.80	0.1754
12:48:31	19		8.78	89.51	0.1564
12:48:32	20		8.78	69.61	0.1157
12:48:33	21		8.79	85.72	0.1486
12:48:34	22		8.79	94.28	0.1661
12:48:35	23		8.79	83.54	0.1442
	24				

Table B.8: 09_Clay_P8_V5_S10

09_Clay_P8_V5_S10					
Real time	Time (s)	Distance (cm)	Temperature (°C)	Turbidity (FTU)	Concentration (g/L)
15:23:04	0	0.00	8.23	3.35	0.0000
15:23:05	1	7.69	8.23	3.31	0.0000
15:23:06	2	15.38	8.23	3.05	0.0000
15:23:07	3	23.08	8.22	2.35	0.0000
15:23:08	4	30.77	8.22	2.53	0.0000
15:23:09	5	38.46	8.21	2.79	0.0000
15:23:10	6	46.15	8.21	3.96	0.0000
15:23:11	7	53.85	8.20	21.97	0.0184
15:23:12	8	61.54	8.20	27.97	0.0306
15:23:13	9	69.23	8.20	46.72	0.0690
15:23:14	10	76.92	8.20	100.36	0.1785
15:23:15	11	84.62	8.20	62.47	0.1011
15:23:16	12	92.31	8.20	49.71	0.0751
15:23:17	13	100.00	8.20	59.51	0.0951
15:23:18	14		8.20	65.56	0.1074
15:23:19	15		8.20	77.39	0.1316
15:23:20	16		8.20	73.28	0.1232
15:23:21	17		8.20	50.00	0.0757
15:23:22	18		8.20	43.28	0.0619
15:23:23	19		8.20	38.20	0.0515
15:23:24	20		8.20	50.54	0.0768
15:23:25	21		8.20	43.25	0.0619
15:23:26	22		8.20	37.84	0.0508
15:23:27	23		8.20	30.05	0.0349
	24				

Table B.9: 14_Clay_P6_V5_S0

14_Clay_P6_V5_S0					
Real time	Time (s)	Distance (cm)	Temperature (°C)	Turbidity (FTU)	Concentration (g/L)
09:18:46	0	0.00	12.01	8.20	0.0000
09:18:47	1	8.33	12.01	8.20	0.0000
09:18:48	2	16.67	12.01	8.20	0.0000
09:18:49	3	25.00	12.01	8.18	0.0000
09:18:50	4	33.33	12.01	7.78	0.0000
09:18:51	5	41.67	12.00	8.74	0.0000
09:18:52	6	50.00	12.00	8.58	0.0000
09:18:53	7	58.33	12.01	9.54	0.0000
09:18:54	8	66.67	12.01	17.27	0.0088
09:18:55	9	75.00	12.01	60.65	0.0974
09:18:56	10	83.33	12.01	41.64	0.0586
09:18:57	11	91.67	12.00	41.49	0.0583
09:18:58	12	100.00	12.01	60.16	0.0964
09:18:59	13		12.02	61.55	0.0993
09:19:00	14		12.03	59.14	0.0943
09:19:01	15		12.04	75.47	0.1277
09:19:02	16		12.05	79.22	0.1354
09:19:03	17		12.06	63.06	0.1023
09:19:04	18		12.06	73.67	0.1240
09:19:05	19		12.06	93.11	0.1637
09:19:06	20		12.06	87.15	0.1516
09:19:07	21		12.06	69.25	0.1150
09:19:08	22		12.05	70.39	0.1173
	23				
	24				

Table B.10: 15_Clay_P6_V5_S20

15_Clay_P6_V5_S20					
Real time	Time (s)	Distance (cm)	Temperature (°C)	Turbidity (FTU)	Concentration (g/L)
09:08:29	0	0.00	13.59	7.78	0.0000
09:08:30	1	9.09	13.59	7.41	0.0000
09:08:31	2	18.18	13.59	7.34	0.0000
09:08:32	3	27.27	13.59	7.08	0.0000
09:08:33	4	36.36	13.59	7.63	0.0000
09:08:34	5	45.45	13.58	25.75	0.0261
09:08:35	6	54.55	13.57	46.45	0.0684
09:08:36	7	63.64	13.55	132.33	0.2439
09:08:37	8	72.73	13.54	119.22	0.2171
09:08:38	9	81.82	13.54	78.67	0.1342
09:08:39	10	90.91	13.55	54.57	0.0850
09:08:40	11	100.00	13.55	97.86	0.1734
09:08:41	12		13.55	171.31	0.3235
09:08:42	13		13.56	88.07	0.1534
09:08:43	14		13.56	82.55	0.1422
09:08:44	15		13.56	72.87	0.1224
09:08:45	16		13.56	94.37	0.1663
09:08:46	17		13.56	53.22	0.0822
09:08:47	18		13.56	47.31	0.0702
09:08:48	19		13.56	45.62	0.0667
09:08:49	20		13.56	33.87	0.0427
09:08:50	21		13.56	46.27	0.0680
	22				
	23				
	24				

Table B.11: 16_Clay_P6_V5_S5

16_Clay_P6_V5_S5					
Real time	Time (s)	Distance (cm)	Temperature (°C)	Turbidity (FTU)	Concentration (g/L)
11:52:06	0	0.00	10.03	3.35	0.0000
11:52:07	1	9.09	10.03	3.35	0.0000
11:52:08	2	18.18	10.02	2.67	0.0000
11:52:09	3	27.27	10.00	2.74	0.0000
11:52:10	4	36.36	9.99	2.60	0.0000
11:52:11	5	45.45	10.00	5.47	0.0000
11:52:12	6	54.55	9.99	15.06	0.0000
11:52:13	7	63.64	9.97	16.78	0.0000
11:52:14	8	72.73	9.95	20.60	0.0156
11:52:15	9	81.82	9.97	19.57	0.0135
11:52:16	10	90.91	10.00	20.59	0.0156
11:52:17	11	100.00	10.04	22.43	0.0193
11:52:18	12		10.08	37.61	0.0503
11:52:19	13		10.10	54.45	0.0847
11:52:20	14		10.11	51.12	0.0779
11:52:21	15		10.12	46.50	0.0685
11:52:22	16		10.12	46.66	0.0688
11:52:23	17		10.12	50.44	0.0766
11:52:24	18		10.13	31.35	0.0376
11:52:25	19		10.12	25.80	0.0262
11:52:26	20		10.11	24.69	0.0239
11:52:27	21		10.11	22.99	0.0205
	22				
	23				
	24				

Table B.12: 17_Clay_P6_V5_S5

17_Clay_P6_V5_S5					
Real time	Time (s)	Distance (cm)	Temperature (°C)	Turbidity (FTU)	Concentration (g/L)
13:38:36	0	0.00	9.47	5.69	0.0000
13:38:37	1	9.09	9.47	5.60	0.0000
13:38:38	2	18.18	9.47	4.66	0.0000
13:38:39	3	27.27	9.46	4.96	0.0000
13:38:40	4	36.36	9.45	4.96	0.0000
13:38:41	5	45.45	9.45	6.98	0.0000
13:38:42	6	54.55	9.45	33.24	0.0414
13:38:43	7	63.64	9.46	50.01	0.0757
13:38:44	8	72.73	9.47	158.89	0.2981
13:38:45	9	81.82	9.48	136.85	0.2531
13:38:46	10	90.91	9.50	125.38	0.2297
13:38:47	11	100.00	9.51	108.81	0.1958
13:38:48	12		9.52	98.52	0.1748
13:38:49	13		9.52	142.60	0.2648
13:38:50	14		9.53	131.05	0.2412
13:38:51	15		9.53	139.59	0.2587
13:38:52	16		9.53	94.70	0.1670
13:38:53	17		9.53	97.73	0.1732
13:38:54	18		9.53	82.75	0.1426
13:38:55	19		9.53	63.34	0.1029
13:38:56	20		9.53	63.08	0.1024
13:38:57	21		9.53	77.20	0.1312
	22				
	23				
	24				

Table B.13: 18_Clay_P6_V5_S20

18_Clay_P6_V5_S20					
Real time	Time (s)	Distance (cm)	Temperature (°C)	Turbidity (FTU)	Concentration (g/L)
09:23:12	0	0.00	13.54	5.38	0.0000
09:23:13	1	9.09	13.55	5.24	0.0000
09:23:14	2	18.18	13.57	5.22	0.0000
09:23:15	3	27.27	13.60	5.60	0.0000
09:23:16	4	36.36	13.62	15.71	0.0000
09:23:17	5	45.45	13.57	19.24	0.0128
09:23:18	6	54.55	13.50	54.71	0.0853
09:23:19	7	63.64	13.42	46.30	0.0681
09:23:20	8	72.73	13.37	42.54	0.0604
09:23:21	9	81.82	13.32	88.01	0.1533
09:23:22	10	90.91	13.29	176.07	0.3332
09:23:23	11	100.00	13.28	154.51	0.2892
09:23:24	12		13.28	133.00	0.2452
09:23:25	13		13.27	159.58	0.2995
09:23:26	14		13.27	112.91	0.2042
09:23:27	15		13.27	73.47	0.1236
09:23:28	16		13.26	64.35	0.1050
09:23:29	17		13.27	58.12	0.0922
09:23:30	18		13.27	51.07	0.0778
09:23:31	19		13.28	35.82	0.0467
09:23:32	20		13.28	34.76	0.0445
09:23:33	21		13.28	29.84	0.0345
	22				
	23				
	24				

Table B.14: 19_clay_P10_V5_S10

19_Clay_P10_V5_S10					
Real time	Time (s)	Distance (cm)	Temperature (°C)	Turbidity (FTU)	Concentration (g/L)
12:19:44	0	0.00	10.65	2.31	0.0000
12:19:45	1	9.09	10.65	5.53	0.0000
12:19:46	2	18.18	10.65	18.15	0.0000
12:19:47	3	27.27	10.66	3.63	0.0000
12:19:48	4	36.36	10.67	6.93	0.0000
12:19:49	5	45.45	10.67	45.67	0.0668
12:19:50	6	54.55	10.66	37.90	0.0509
12:19:51	7	63.64	10.65	156.28	0.2928
12:19:52	8	72.73	10.65	149.41	0.2788
12:19:53	9	81.82	10.67	92.45	0.1624
12:19:54	10	90.91	10.68	68.78	0.1140
12:19:55	11	100.00	10.69	69.04	0.1146
12:19:56	12		10.69	57.29	0.0906
12:19:57	13		10.70	113.76	0.2059
12:19:58	14		10.70	84.88	0.1469
12:19:59	15		10.70	78.53	0.1339
12:20:00	16		10.70	47.99	0.0716
12:20:01	17		10.70	39.44	0.0541
12:20:02	18		10.70	50.42	0.0765
12:20:03	19		10.70	42.83	0.0610
12:20:04	20		10.70	44.56	0.0645
12:20:05	21		10.69	40.79	0.0568
	22				
	23				
	24				

Table B.15: 20_Clay_P6_V10_S10

20_Clay_P6_V10_S10					
Real time	Time (s)	Distance (cm)	Temperature (°C)	Turbidity (FTU)	Concentration (g/L)
15:18:01	0	0.00	9.92	3.29	0.0000
15:18:02	1	14.29	9.91	2.85	0.0000
15:18:03	2	28.57	9.90	2.79	0.0000
15:18:04	3	42.86	9.89	5.70	0.0000
15:18:05	4	57.14	9.88	19.49	0.0133
15:18:06	5	71.43	9.86	266.12	0.5172
15:18:07	6	85.71	9.85	153.50	0.2871
15:18:08	7	100.00	9.84	112.91	0.2042
15:18:09	8		9.82	138.35	0.2562
15:18:10	9		9.81	176.06	0.3332
15:18:11	10		9.80	98.31	0.1744
15:18:12	11		9.79	63.86	0.1040
15:18:13	12		9.78	63.40	0.1030
15:18:14	13		9.77	80.10	0.1372
15:18:15	14		9.77	42.53	0.0604
15:18:16	15		9.76	30.09	0.0350
15:18:17	16		9.76	33.18	0.0413
15:18:18	17		9.76	34.39	0.0438
	18				
	19				
	20				
	21				
	22				
	23				
	24				

Table B.16: 21_Clay_P6_V8_S10

21_Clay_P6_V8_S10					
Real time	Time (s)	Distance (cm)	Temperature (°C)	Turbidity (FTU)	Concentration (g/L)
08:59:44	0	0.00	13.02	7.12	0.0000
08:59:45	1	11.11	13.01	7.11	0.0000
08:59:46	2	22.22	13.00	8.07	0.0000
08:59:47	3	33.33	12.99	11.55	0.0000
08:59:48	4	44.44	12.98	41.97	0.0593
08:59:49	5	55.56	12.95	204.61	0.3915
08:59:50	6	66.67	12.93	159.76	0.2999
08:59:51	7	77.78	12.91	227.48	0.4383
08:59:52	8	88.89	12.89	197.15	0.3763
08:59:53	9	100.00	12.87	255.96	0.4964
08:59:54	10		12.85	173.47	0.3279
08:59:55	11		12.82	160.71	0.3018
08:59:56	12		12.80	143.90	0.2675
08:59:57	13		12.78	110.41	0.1991
08:59:58	14		12.78	61.48	0.0991
08:59:59	15		12.78	52.90	0.0816
09:00:00	16		12.78	48.03	0.0716
09:00:01	17		12.78	34.33	0.0436
09:00:02	18		12.78	26.62	0.0279
09:00:03	19		12.78	30.94	0.0367
	20				
	21				
	22				
	23				
	24				

Table B.17: 22_Clay_P6_V20_S10

22_Clay_P6_V20_S10					
Real time	Time (s)	Distance (cm)	Temperature (°C)	Turbidity (FTU)	Concentration (g/L)
11:05:51	0	0.00	11.16	5.06	0.0000
11:05:52	1	20.00	11.16	8.61	0.0000
11:05:53	2	40.00	11.17	8.75	0.0000
11:05:54	3	60.00	11.15	49.15	0.0739
11:05:55	4	80.00	11.13	125.41	0.2229
11:05:56	5	100.00	11.14	151.37	0.2764
11:05:57	6		11.14	141.74	0.2566
11:05:58	7		11.14	116.82	0.2052
11:05:59	8		11.15	119.41	0.2106
11:06:00	9		11.15	86.53	0.1428
11:06:01	10		11.15	93.15	0.1564
11:06:02	11		11.14	80.50	0.1304
11:06:03	12		11.14	69.25	0.1072
11:06:04	13		11.14	46.04	0.0594
11:06:05	14		11.14	45.22	0.0577
11:06:06	15		11.14	61.92	0.0921
	16				
	17				
	18				
	19				
	20				
	21				
	22				
	23				
	24				

Table B.18: 23_Clay_P6_V5_S10

23_Clay_P6_V5_S10					
Real time	Time (s)	Distance (cm)	Temperature (°C)	Turbidity (FTU)	Concentration (g/L)
13:03:35	0	0.00	10.70	3.37	0.0000
13:03:36	1	9.09	10.70	2.67	0.0000
13:03:37	2	18.18	10.69	2.59	0.0000
13:03:38	3	27.27	10.68	2.64	0.0000
13:03:39	4	36.36	10.68	3.15	0.0000
13:03:40	5	45.45	10.68	16.89	0.0000
13:03:41	6	54.55	10.67	33.15	0.0412
13:03:42	7	63.64	10.66	140.41	0.2538
13:03:43	8	72.73	10.66	225.17	0.4284
13:03:44	9	81.82	10.66	171.41	0.3177
13:03:45	10	90.91	10.67	140.49	0.2540
13:03:46	11	100.00	10.68	204.07	0.3850
13:03:47	12		10.69	252.18	0.4841
13:03:48	13		10.69	131.97	0.2364
13:03:49	14		10.69	147.99	0.2694
13:03:50	15		10.69	158.96	0.2920
13:03:51	16		10.68	113.97	0.1993
13:03:52	17		10.68	105.58	0.1821
13:03:53	18		10.68	136.77	0.2463
13:03:54	19		10.68	108.34	0.1877
13:03:55	20		10.68	87.05	0.1439
13:03:56	21		10.68	81.67	0.1328
	22				
	23				
	24				

Table B.19: 01_DSClay_P6_V5_S10

01_DSClay_P6_V5_S10					
Real time	Time (s)	Distance (cm)	Temperature (°C)	Turbidity (FTU)	Concentration (g/L)
11:58:45	0	0.00	9.74	3.02	0.0060
11:58:46	1	9.09	9.75	2.80	0.0056
11:58:47	2	18.18	9.75	2.09	0.0042
11:58:48	3	27.27	9.75	2.11	0.0042
11:58:49	4	36.36	9.74	2.43	0.0048
11:58:50	5	45.45	9.74	5.02	0.0100
11:58:51	6	54.55	9.75	15.23	0.0304
11:58:52	7	63.64	9.75	18.35	0.0366
11:58:53	8	72.73	9.76	33.06	0.0660
11:58:54	9	81.82	9.78	39.12	0.0781
11:58:55	10	90.91	9.79	39.26	0.0783
11:58:56	11	100.00	9.82	65.37	0.1304
11:58:57	12		9.84	147.09	0.2935
11:58:58	13		9.85	101.65	0.2028
11:58:59	14		9.86	136.66	0.2727
11:59:00	15		9.87	112.64	0.2247
11:59:01	16		9.88	64.39	0.1285
11:59:02	17		9.88	51.45	0.1027
11:59:03	18		9.89	50.60	0.1010
11:59:04	19		9.89	48.12	0.0960
11:59:05	20		9.89	57.04	0.1138
11:59:06	21		9.89	55.57	0.1109
	22				
	23				
	24				

C

Sediment Bed Pictures

This appendix shows the sediment bed profiles after the test run.



(a) 01 Imitation clay



(b) 02 Imitation clay



(c) 04 Imitation clay



(d) 05 Imitation clay



(e) 06 Imitation clay



(f) 07 Imitation clay



(g) 07 Imitation clay after a beam fell in the bed



(h) 08 Imitation clay

Figure C.1: Pictures after test run of tests 1 till 8 and DSC



(a) 09 Imitation clay **(b)** 10 Imitation clay **(c)** 11 Imitation clay **(d)** 12 Imitation clay

(e) 14 Imitation clay **(f)** 15 Imitation clay **(g)** 16 Imitation clay **(h)** 17 Imitation clay

(i) 18 Imitation clay **(j)** 19 Imitation clay **(k)** 20 Imitation clay **(l)** 21 Imitation clay

(m) 22 Imitation clay **(n)** 23 Imitation clay **(o)** 01 Deep-sea clay

Figure C.2: Pictures after test run of tests 9 till 23 and DSC

D

Sediment Bed Height Profiles

Sediment bed height profiles made by the 3D camera.

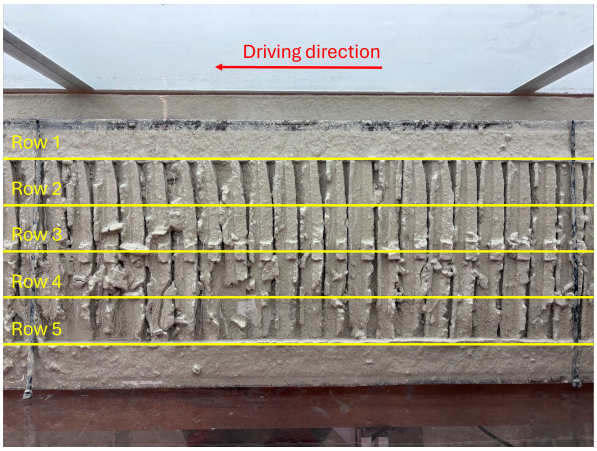
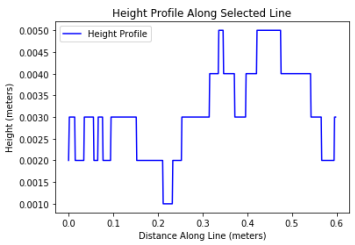
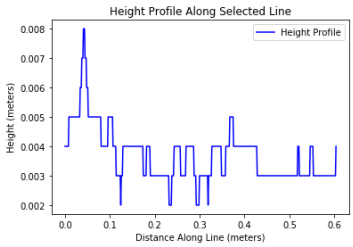


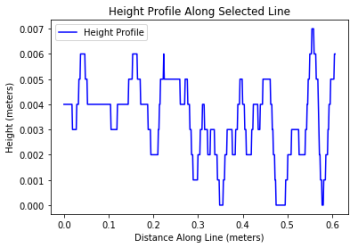
Figure D.1: The lines used for the height profiles of the sediment beds



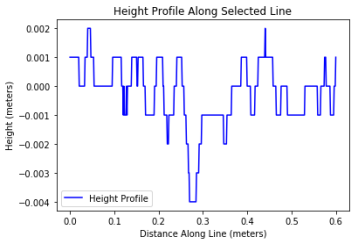
(a) Row 1



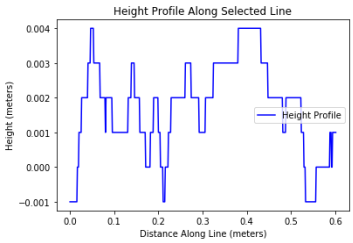
(b) Row 2



(c) Row 3

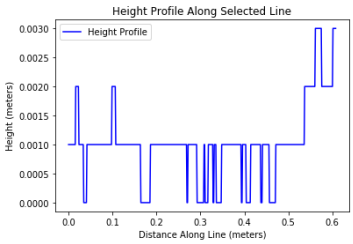


(d) Row 4

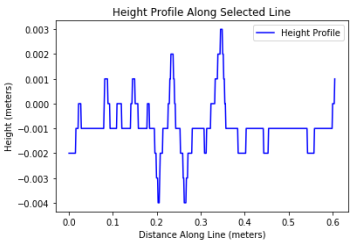


(e) Row 5

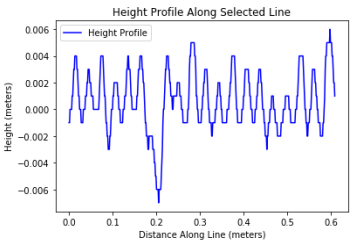
Figure D.2: Deep-sea clay 01



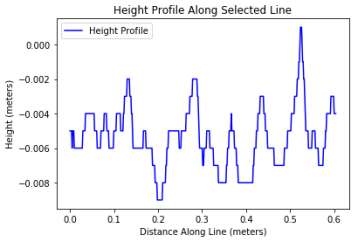
(a) Row 1



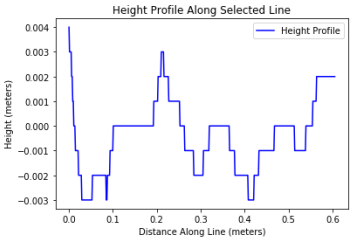
(b) Row 2



(c) Row 3

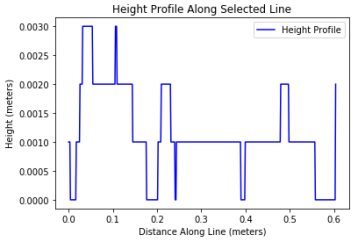


(d) Row 4

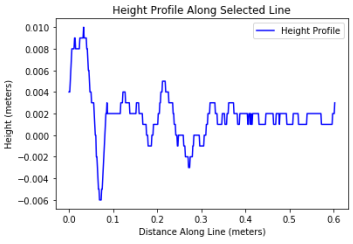


(e) Row 5

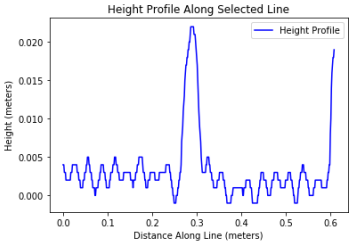
Figure D.3: Clay 02



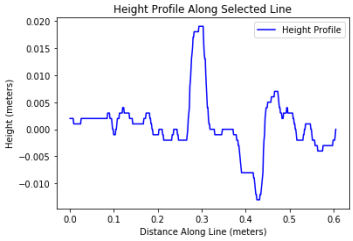
(a) Row 1



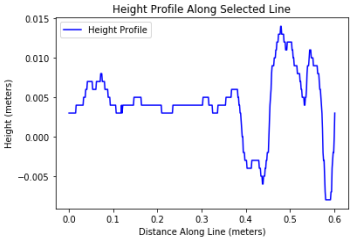
(b) Row 2



(c) Row 3

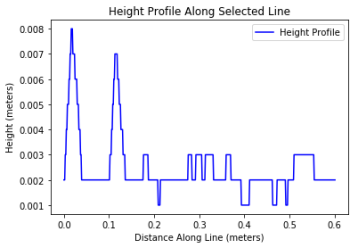


(d) Row 4

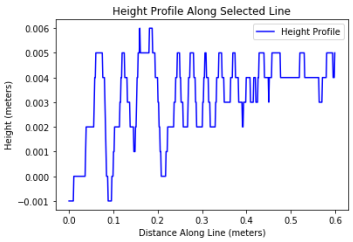


(e) Row 5

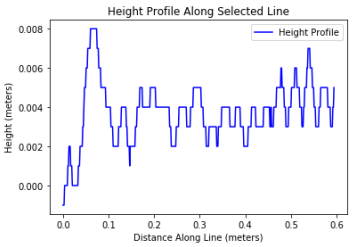
Figure D.4: Clay 04



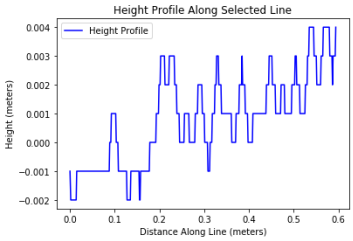
(a) Row 1



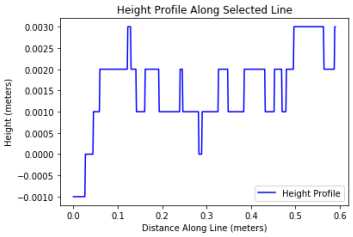
(b) Row 2



(c) Row 3

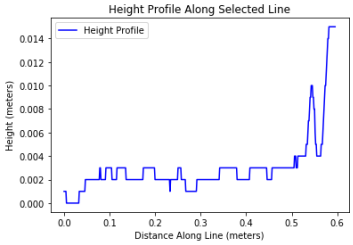


(d) Row 4

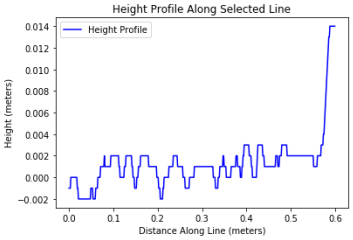


(e) Row 5

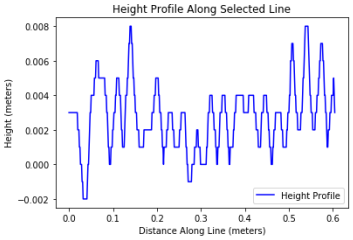
Figure D.5: Clay 05



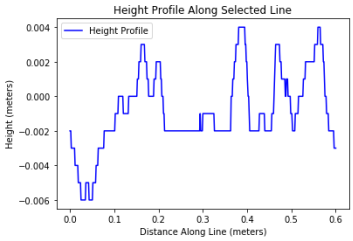
(a) Row 1



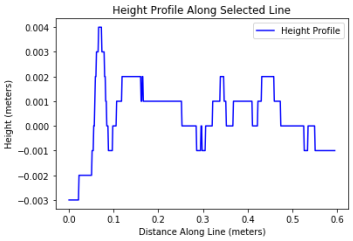
(b) Row 2



(c) Row 3

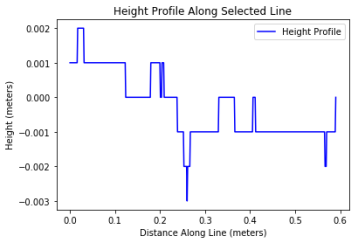


(d) Row 4

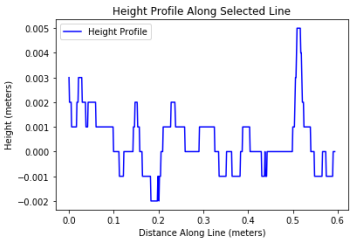


(e) Row 5

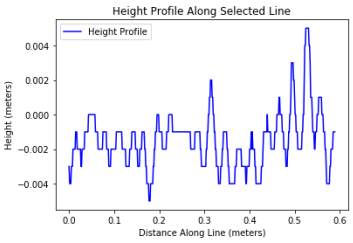
Figure D.6: Clay 06



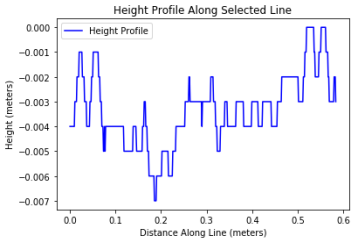
(a) Row 1



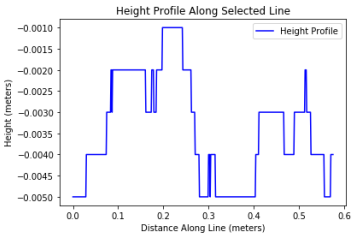
(b) Row 2



(c) Row 3

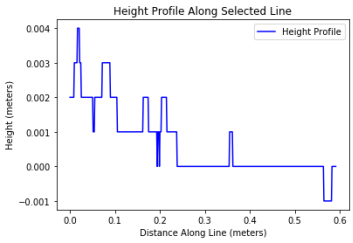


(d) Row 4

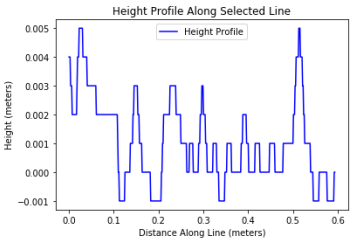


(e) Row 5

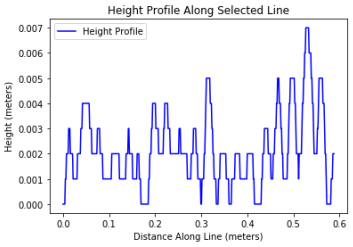
Figure D.7: Clay 07



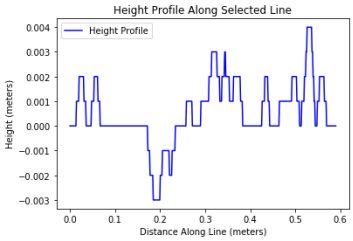
(a) Row 1



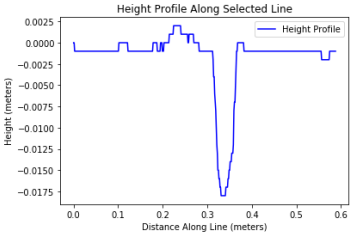
(b) Row 2



(c) Row 3

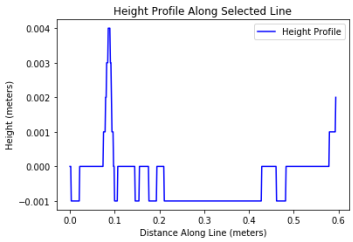


(d) Row 4

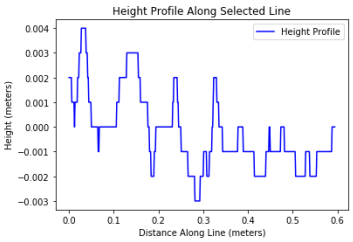


(e) Row 5

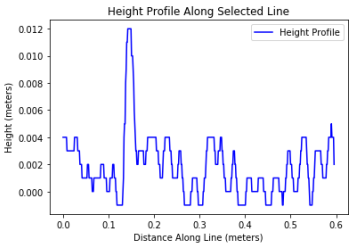
Figure D.8: Clay 07 after a beam fell in the bed



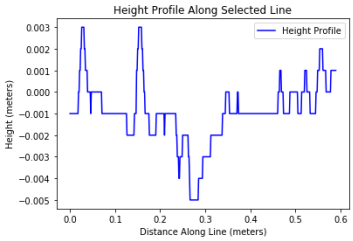
(a) Row 1



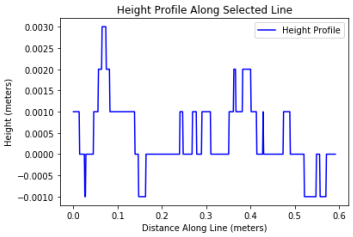
(b) Row 2



(c) Row 3

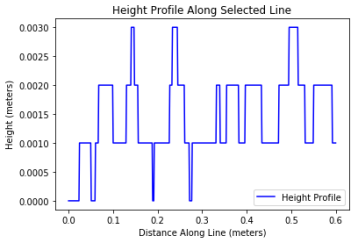


(d) Row 4

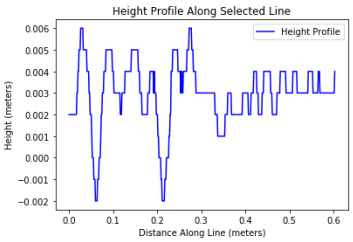


(e) Row 5

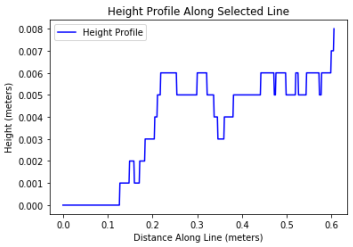
Figure D.9: Clay 08



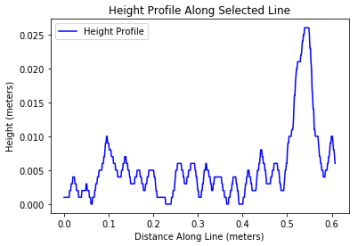
(a) Row 1



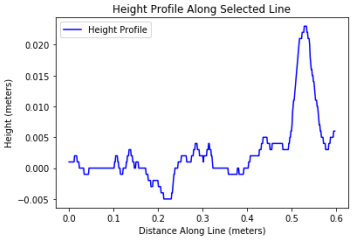
(b) Row 2



(c) Row 3

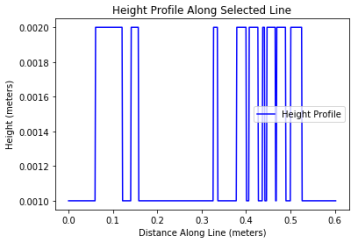


(d) Row 4

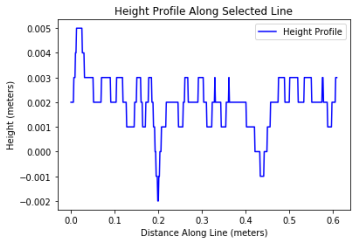


(e) Row 5

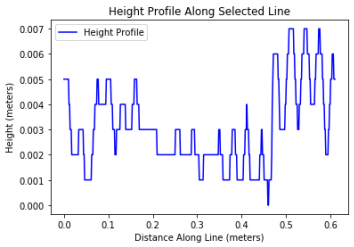
Figure D.10: Clay 09



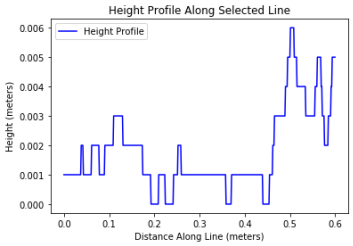
(a) Row 1



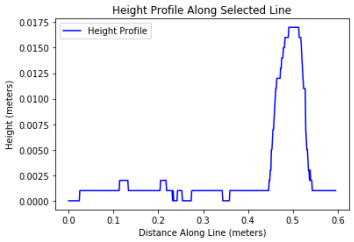
(b) Row 2



(c) Row 3

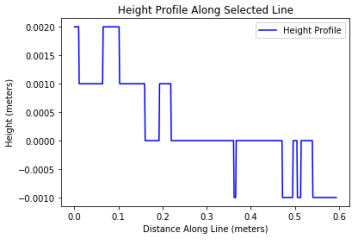


(d) Row 4

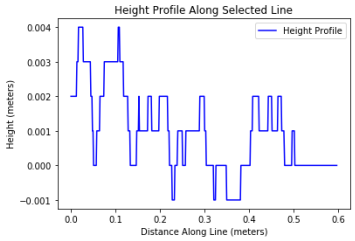


(e) Row 5

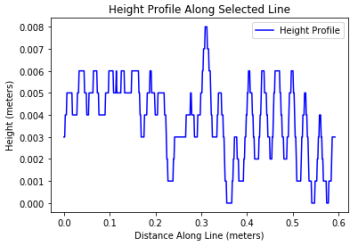
Figure D.11: Clay 10



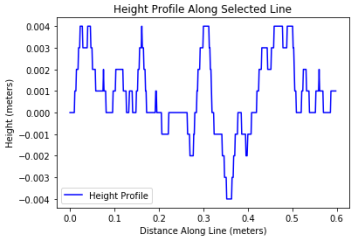
(a) Row 1



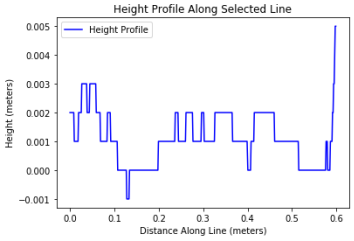
(b) Row 2



(c) Row 3

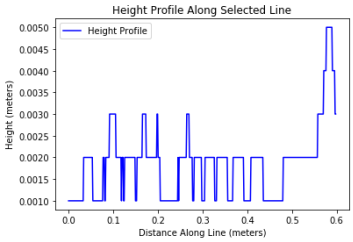


(d) Row 4

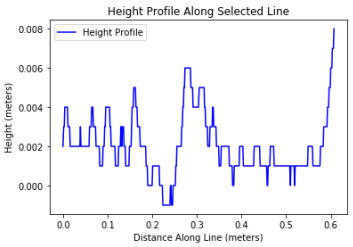


(e) Row 5

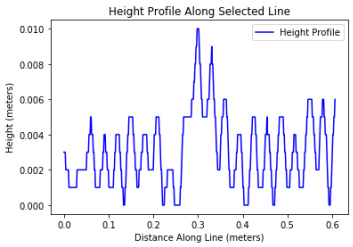
Figure D.12: Clay 11



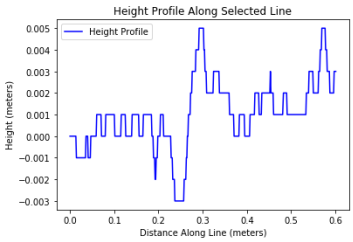
(a) Row 1



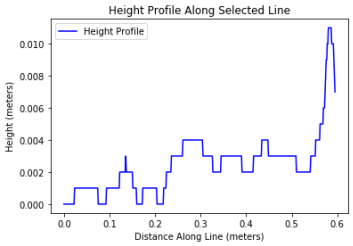
(b) Row 2



(c) Row 3

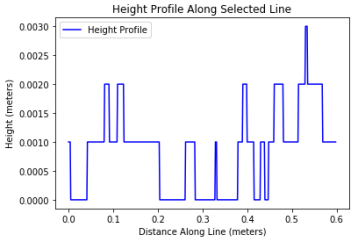


(d) Row 4

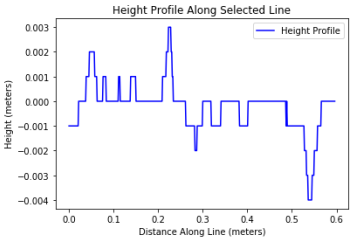


(e) Row 5

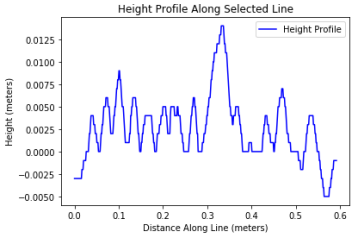
Figure D.13: Clay 12



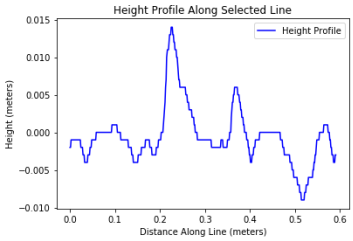
(a) Row 1



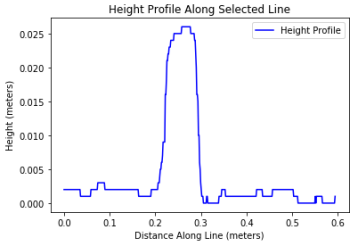
(b) Row 2



(c) Row 3

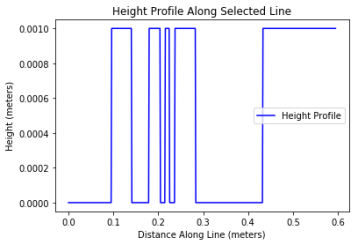


(d) Row 4

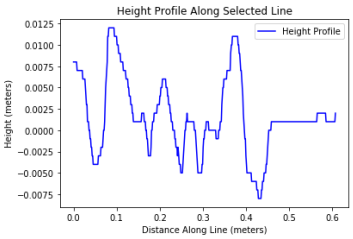


(e) Row 5

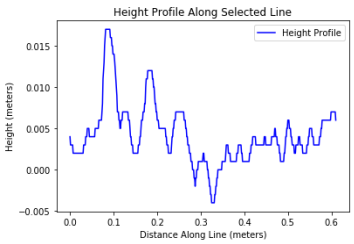
Figure D.14: Clay 14



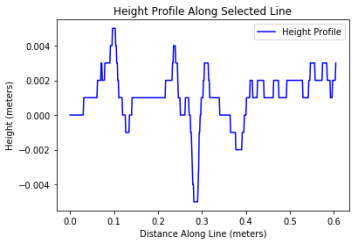
(a) Row 1



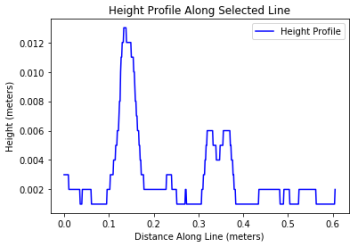
(b) Row 2



(c) Row 3

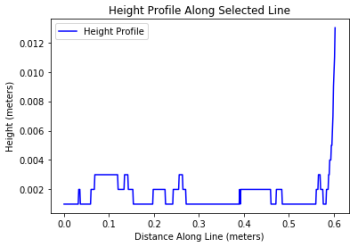


(d) Row 4

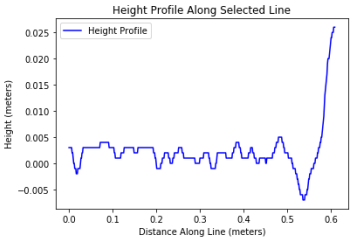


(e) Row 5

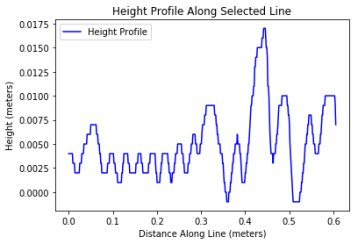
Figure D.15: Clay 15



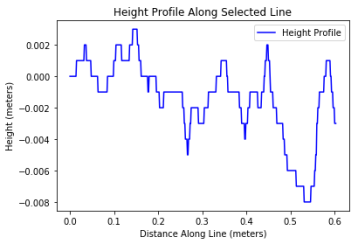
(a) Row 1



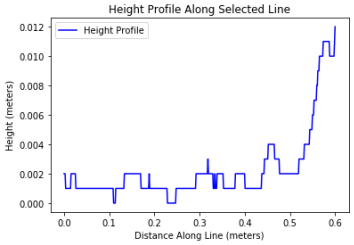
(b) Row 2



(c) Row 3

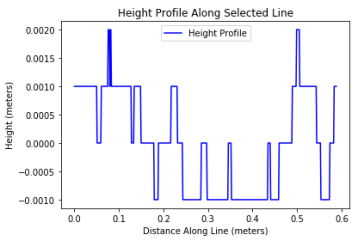


(d) Row 4

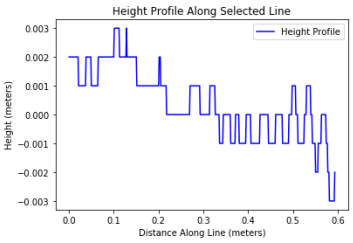


(e) Row 5

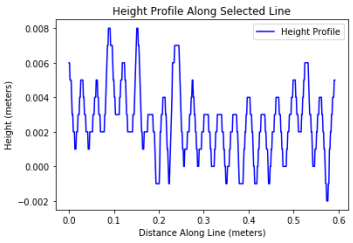
Figure D.16: Clay 16



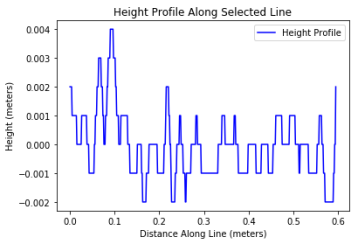
(a) Row 1



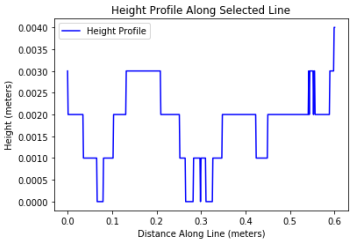
(b) Row 2



(c) Row 3

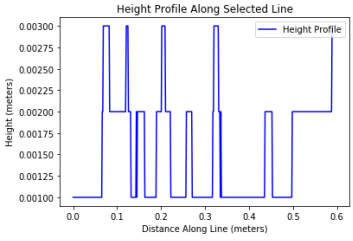


(d) Row 4

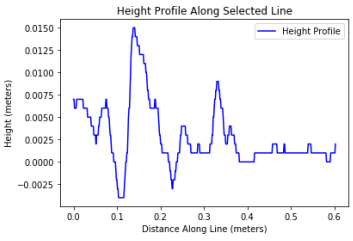


(e) Row 5

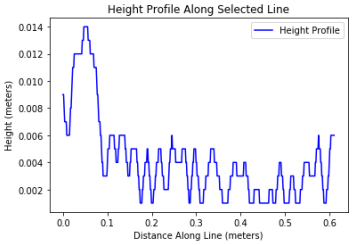
Figure D.17: Clay 17



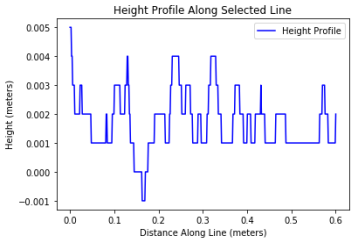
(a) Row 1



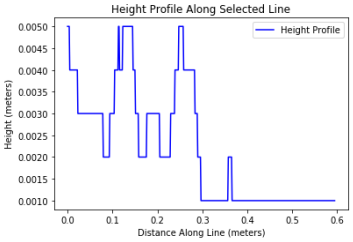
(b) Row 2



(c) Row 3

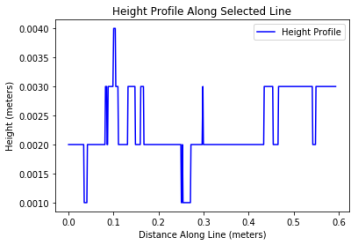


(d) Row 4

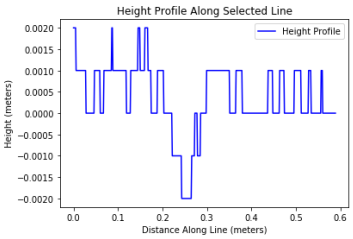


(e) Row 5

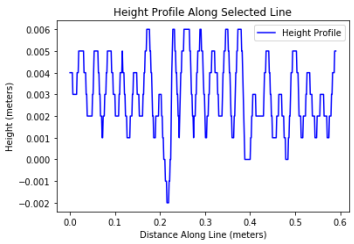
Figure D.18: Clay 18



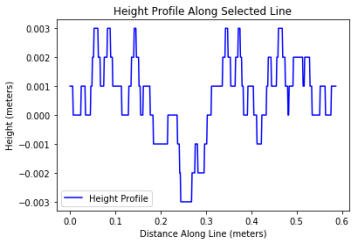
(a) Row 1



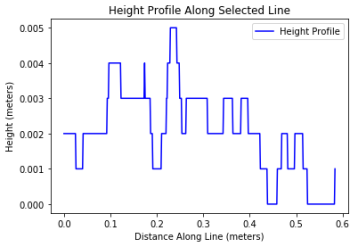
(b) Row 2



(c) Row 3

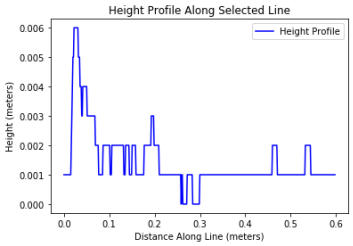


(d) Row 4

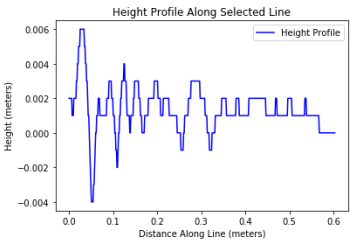


(e) Row 5

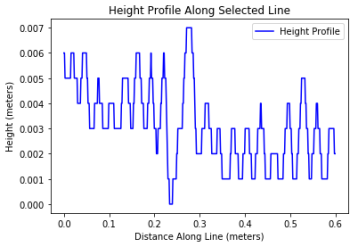
Figure D.19: Clay 19



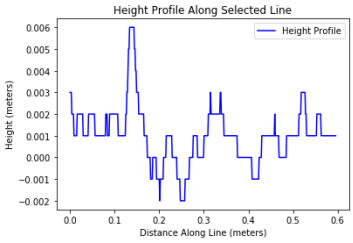
(a) Row 1



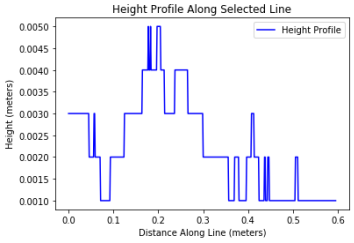
(b) Row 2



(c) Row 3

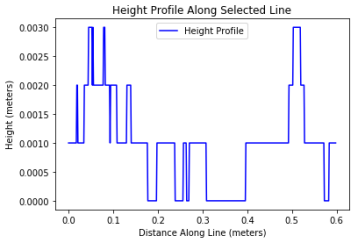


(d) Row 4

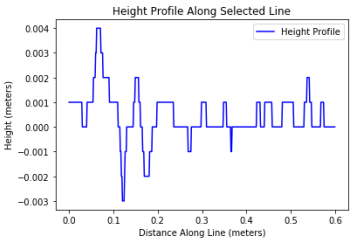


(e) Row 5

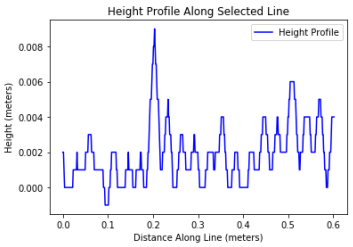
Figure D.20: Clay 20



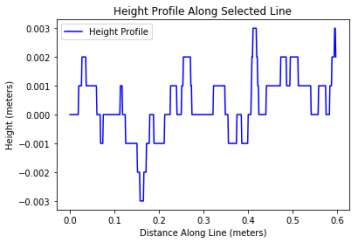
(a) Row 1



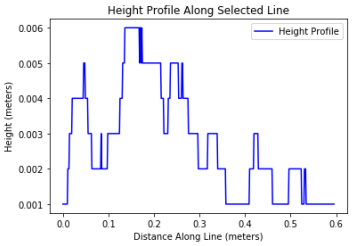
(b) Row 2



(c) Row 3

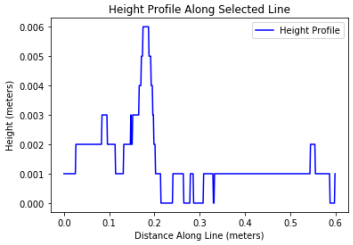


(d) Row 4

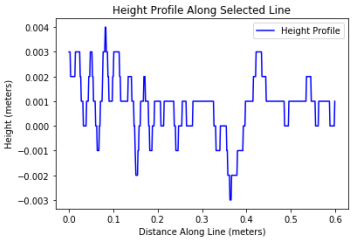


(e) Row 5

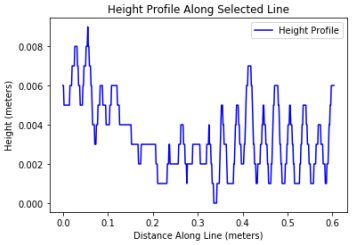
Figure D.21: Clay 21



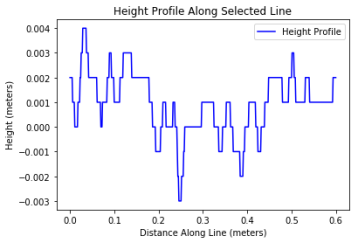
(a) Row 1



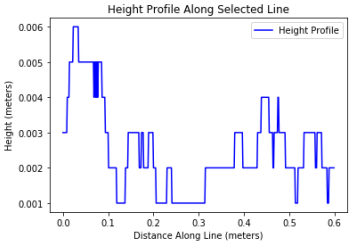
(b) Row 2



(c) Row 3

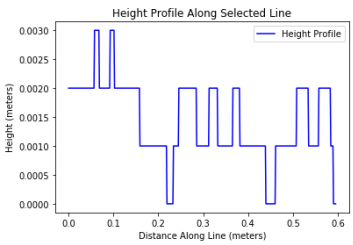


(d) Row 4

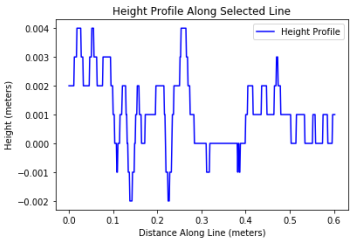


(e) Row 5

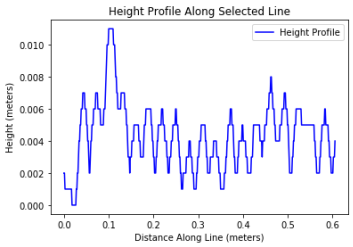
Figure D.22: Clay 22



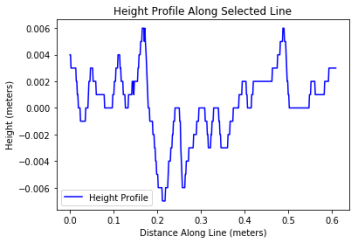
(a) Row 1



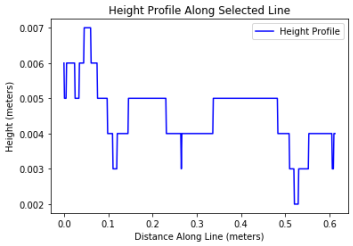
(b) Row 2



(c) Row 3



(d) Row 4



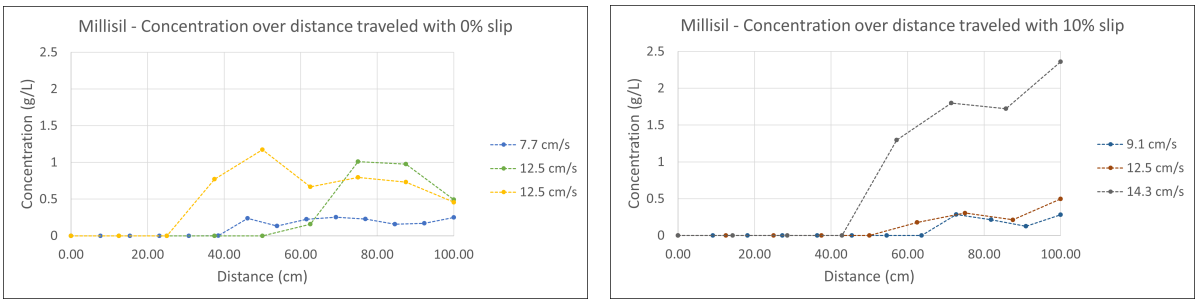
(e) Row 5

Figure D.23: Clay 23

E

Millisil Results

The Millisil experiments are primarily conducted to study plume generation caused by the tracks and to refine the experimental setup, ensuring it is fully optimised before starting the clay experiments. However, data is also gathered during these Millisil tests. The concentrations measured by the OBS are shown in Figure E.1. Unlike the clay experiments, the Millisil data do not exhibit sharp concentration spikes when the OBS enters a dense plume. Instead, the concentrations appear more stable over the distance travelled.
A clear trend can be observed: plume concentration increases with velocity, which aligns with the results from the imitation clay experiments. However, the effect of slip rate appears less consistent. For instance, the test at 14.3 cm/s with 10% slip (Figure E.1b) shows the highest concentration among the Millisil experiments, but this may be attributed more to its high velocity than the slip rate. In contrast, among all tests conducted at 12.5 cm/s, the 10% test shows the lowest concentration and the 9.3 cm/s test with 10% slip yields a lower concentration than the slower 7.7 cm/s test with 0% slip. These results deviate from expectations and the trends observed in the clay tests.



(a) **(b)**

Figure E.1: Concentrations measured by the OBS over the distance traveled by the tracks for the Millisil experiments, with (a) 0% slip and (b) 10% slip

The Millisil bed is highly packed, making it difficult to penetrate. As a result, the grousers cannot fully embed into the sediment, causing the tracks to drive on the grousers rather than the rubber belt. This deviation may have affected the interpretability of the results. The dense packing of the bed also made it impossible to conduct track penetration experiments.
After the test runs, small clusters of Millisil are observed adhering to the grousers, as shown in Figure E.2. This is likely caused by suction forces, further indicating the tightly packed nature of the sediment.



Figure E.2: Picture of the tracks after a Millisil experiment where clusters of sediment are sticking to the grousers (in the middle of the tracks)

It is observed that when fully saturated, Millisil exhibits behaviour somewhat similar to that of a non-Newtonian fluid: it behaves like a firm solid under short, high-intensity forces, while becoming more workable and fluid-like under sustained, low-intensity forces.

F

Millisil Filtering Process

Pictures taken during the Millisil filtering process. All pictures use the following code: SxTy, where 'x' is the number of the washing and 'y' the time in hours after mixing it.

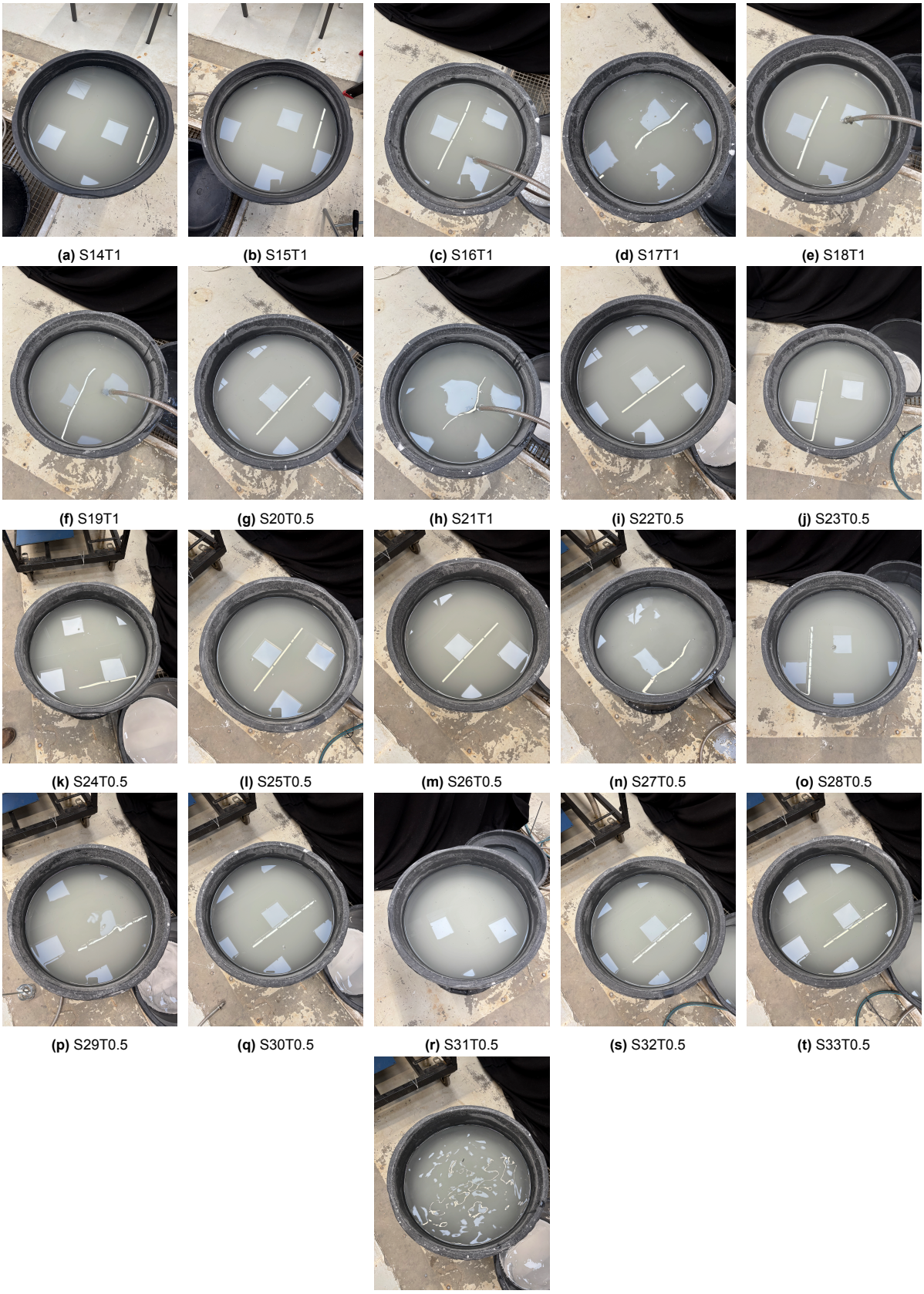


(a) S1T0 **(b)** S1T1 **(c)** S1T2.5 **(d)** S2T0 **(e)** S2T1

(f) S3T1 **(g)** S4T1 **(h)** S5T1 **(i)** S6T1 **(j)** S8T21.5

(k) S9T1 **(l)** S10T1 **(m)** S11T1 **(n)** S12T1 **(o)** S13T1

Figure F.1: Millisil filtering process from washing 1 till 13



(a) S14T1 **(b)** S15T1 **(c)** S16T1 **(d)** S17T1 **(e)** S18T1

(f) S19T1 **(g)** S20T0.5 **(h)** S21T1 **(i)** S22T0.5 **(j)** S23T0.5

(k) S24T0.5 **(l)** S25T0.5 **(m)** S26T0.5 **(n)** S27T0.5 **(o)** S28T0.5

(p) S29T0.5 **(q)** S30T0.5 **(r)** S31T0.5 **(s)** S32T0.5 **(t)** S33T0.5

(u) S34T0.5

Figure F.2: Millisil filtering process from washing 14 till 34